Comptes Rendus de l'Académie des sciences

1878-1535 (electronic)

Physique

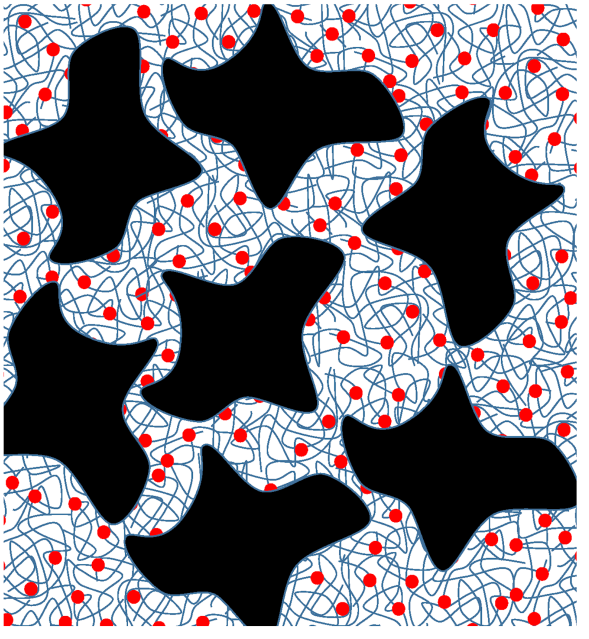

Volume 22, Special Issue S5, 2021

Special issue / *Numéro thématique*

Prizes of the French Academy of Sciences 2020 / *Prix 2020 de l'Académie des sciences*

Académie des sciences — Paris

INSTITUT DE FRANCE
Académie des sciences

CENTRE MERSENNE

Comptes Rendus

Physique

Objective of the journal

Comptes Rendus Physique is a peer-reviewed electronic journal of international standing, covering all fields of physics and astrophysics. It publishes mainly thematic issues, but also original research articles, preliminary announcements, review articles, historical perspectives, pedagogical texts or conference proceedings, without length limit, in English or in French. It also publishes special issues devoted to certain recent and/or significant aspects of the discipline, whose authors are chosen from among the most active researchers on the subject and whose coordination is assured by guest editors.

Comptes Rendus Physique is published according to a virtuous policy of diamond open access, free for authors (no publication fees) as well as for readers (immediate and permanent open access).

About the journal

All journal's information, including the text of published articles, which is fully open access, is available from the journal website at https://comptes-rendus.academie-sciences.fr/physique/.

Author enquiries

For enquiries relating to the submission of articles, please visit this journal's homepage at https://comptes-rendus.academie-sciences.fr/physique/.

Contact

Académie des sciences
23, quai de Conti, 75006 Paris, France
Tel: (+33) (0)1 44 41 43 72
CR-Physique@academie-sciences.fr

Comptes Rendus
Physique
2021, 22, nº S5

Contents / *Sommaire*

Comptes Rendus
Physique
2021, 22, nº S5, p. 1-5
https://doi.org/10.5802/crphys.107

Foreword: Prizes of the French Academy of Sciences 2020

Avant-propos : Prix 2020 de l'Académie des sciences

Jacques Villain[*, a]

[a] Institut Laue-Langevin, 71 Avenue des Martyrs, CS 20156, 38042 Grenoble cedex 9, France
E-mail: jvillain@infonie.fr

This special issue of *Comptes Rendus Physique* brings together articles by three winners of prizes awarded by the Academy of Sciences in 2020. The goal of this foreword is to make them more accessible by non experts, especially students.

The first article, by Philippe Bourges ("Science et innovation" CEA prize), Dalila Bounoua and Yvan Sidis, is part of the history of superconductivity, fertile in unexpected twists for 110 years. It was in 1911 that the Dutch scientist Kamerlingh Onnes, having succeeded in achieving very low temperatures which allowed him to liquefy helium, had the very natural curiosity to study the properties of various elements at these temperatures. He was surprised to find that some of them had zero electrical resistance. An electric current could thus circulate for days in a ring of mercury. What was the explanation for this perpetual motion? It was not found until 46 years later by Bardeen, Cooper and Schrieffer, in 1957. These three scientists showed that electrons can form pairs (Cooper pairs). In a simplified description, we can say that these pairs are bosons and that at very low temperatures these bosons undergo Bose condensation, which leads to superconductivity. It is obvious that a vanishing electric resistance has a considerable technological interest, but this interest was considerably reduced by the need for very low temperatures. The critical temperature of the elements culminates at about ten kelvins in niobium and can reach higher values in compounds, but it was not expected to exceed the 23 K which correspond to Nb_3Ge. However, in 1986 in Zürich, Müller and Bednorz discovered a family of superconductors whose critical temperature was higher, and a little later exceeded the temperature of liquid nitrogen (77 K). These materials were oxides containing copper and other metals. A stoichiometric oxide is an insulator, but if stoichiometry is violated, a conductor can be obtained, and even a superconductor (see figure 1 of the article by Bourges et al.). Unfortunately this type of superconductivity cannot be explained by the theory of Bardeen, Cooper and Schrieffer… nor by any theory currently accepted by all theoreticians. To fully understand the superconductivity of

* Corresponding author.

cuprates, one has to understand the transition to the non-superconducting state, and therefore to understand the non-superconducting state which appears above the critical temperature T_c. This state itself presents remarkable particularities below a temperature T^*. The phase which is stable between T_c and T^* is called pseudogap phase for reasons which will not be explained here. In particular, its Fermi surface is quite different from the Fermi surface at $T > T^*$ [1–3]. We would like to characterize the pseudo-gap phase by structural, e.g. electronic properties. This is precisely the subject of the article by Bourges et al. The authors think they have confirmed by polarized neutron diffraction a theory of Varma according to which certain electrons would describe closed trajectories (loops) by hopping from one atom to another. This is an unusual thing. We usually imagine conduction electrons moving in a straight line and localized electrons rotating around a nucleus. Varma's interatomic loops constitute magnetic moments as well as the intra-atomic loops, and these magnetic moments, according to the observations of the authors, are ordered in an antiferromagnetic structure. This magnetism in which spin plays no role is a great novelty. But there is still a lot to do, especially for theoreticians. The coincidence of the pseudo-gap with this novel magnetism is an experimental observation, but it remains to be determined if it has a deep physical reason.

The second article of this special issue, written by Hélène Montes and François Lequeux (prix de la fondation d'entreprise Michelin) is devoted to the materials that make up our tires, for example: elastomers reinforced by the inclusion of rigid particles intended to improve their mechanical qualities, in particular their resistance to wear. The authors begin by describing the properties of pure elastomer, which is a viscoelastic material, i.e. having both viscosity and elasticity. Its response to a time-dependent stress is described by the relaxation modulus $E(t)$ which, like the elastic modulus E (also called Young's modulus) and the shear modulus, is expressed in Pascals. The authors introduce a model, based on the discovery of dynamic heterogeneities in glasses at the scale of a few nanometers, which describes well the viscoelastic behavior of a homogeneous elastomer from the assumption of a domain structure. They then treat elastomers reinforced with rigid particles. They show that these particles are mechanically linked by two kinds of bonds: glassy bridges and rubber bridges; the glassy state and the rubber state of an elastomer differ by the value of the shear modulus, of the order of GPa in the first case and MPa in the second. The authors apply in particular their ideas to the Payne effect, a non-linear phenomenon which leads to high energy dissipation in reinforced elastomers.

The third article presented here is the work of Etienne Perret (Espoir-IMT prize)… It illustrates the growing presence of robots in our lives, a presence that would not be possible without the complicity of physicists. A century ago, when somebody went to the grocer to buy a jar of fresh cream and a pair of socks, the grocer had to calculate the price by adding up with a pencil and a sheet of paper, which required time and involved the risk of error. Half a century later, the grocer had acquired a machine that did the additions, a kind of very specialized robot, which unfortunately was unable to read, so that the grocer had to introduce the numbers to be added. The waste of time and the risk of error were less, but not zero. Today, when we go to the supermarket to buy ten items, it is sufficient to present the 10 barcodes to a robot reader which takes care of the reading and the additions. The barcode is just a label that carries simple information in a language that the robot can read more easily than Arabic numerals and the Latin alphabet. Also, if the supermarket decides to change the price, this can be done without changing the label. In this dialogue between a tag and a reading robot, the robot can be extremely sophisticated and receive orders from the other side of the world, but the tag must be as cheap as possible. Perret and his collaborators replace the optical reading of the bar code or the QR code (Quick Reading) by a reading by electromagnetic waves at radio frequency, which makes it possible, for example, to read information concealed by an opaque

envelope. This obviously involves replacing the barcode with a label of another kind. Such labels already exist. They use RFID technology [radio frequency identification], which equips contactless bus tickets, ski passes, building entry badges. These labels, which use electronic "chips", have the drawback of being significantly more expensive than barcodes or QR codes. Perret and his collaborators offer cheap, radio-readable tags without chips. More details can be found in an interview with the author, on the website: https://imtech.wp.imt.fr/2020/11/24/prix-imt-academie-des-sciences-etienne-perret/… and of course in the article of this special issue.

These three articles give an idea of the diversity of current research in physics.

I acknowledge the help of Antoine Georges, Marc-Henri Julien and Tim Ziman as well as that of the authors.

Avant-propos

Le présent numéro spécial des *Comptes Rendus Physique* rassemble des articles de trois lauréats de prix décernés par l'Académie des Sciences en 2020. L'avant-propos qui y suit tente de les rendre plus accessibles aux non spécialistes et notamment aux étudiants.

Le premier article, dû à Philippe Bourges (Prix « Science et innovation » du CEA), Dalila Bounoua et Yvan Sidis, s'inscrit dans l'histoire de la supraconductivité, fertile en rebondissements inattendus depuis 110 ans. C'est en effet en 1911 que le Néerlandais Kamerlingh Onnes, ayant réussi à réaliser de très basses températures qui lui permettaient de liquéfier l'hélium, eut la curiosité bien naturelle d'étudier les propriétés de divers éléments à ces températures. Il eut la surprise de constater que certains d'entre eux avaient une résistance électrique nulle. Un courant électrique pouvait ainsi circuler pendant des jours dans un anneau de mercure. Quelle était l'explication de ce mouvement perpétuel? Elle ne fut trouvée que 46 ans plus tard par Bardeen, Cooper et Schrieffer, en 1957. Ces trois chercheurs montrèrent que les électrons peuvent former des paires (paires de Cooper). Dans une description simplifiée, on peut dire que ces paires sont des bosons et qu'à très basse température ces bosons subissent la condensation de Bose, ce qui mène à la supraconductivité. Il est évident qu'une résistance électrique nulle a un intérêt technologique considérable, mais cet intérêt se trouvait considérablement diminué par la nécessité de températures très basses. La température critique des éléments culmine à une dizaine de kelvins dans le niobium et peut atteindre des valeurs plus élevées dans des composés, mais on ne pensait pas pouvoir dépasser les 23 K qui correspondent à Nb_3Ge. Or, en 1986 à Zürich, Müller et Bednorz découvrirent une famille de supraconducteurs dont la température critique était plus élevée et allait un peu plus tard dépasser la température de l'azote liquide (77 K). Il s'agissait d'oxydes contenant du cuivre et d'autres métaux. Un oxyde bien stœchiométrique est isolant, mais si on viole la stœchiométrie on peut obtenir un conducteur, et même un supraconducteur (voir la figure 1 de l'article de Bourges *et al.*). Malheureusement ce type de supraconductivité n'est pas explicable par la théorie de Bardeen, Cooper et Schrieffer… ni par aucune théorie admise par tous les théoriciens actuellement. Pour bien comprendre la supraconductivité, il faudrait comprendre la transition à l'état non supraconducteur, donc comprendre l'état non supraconducteur qui apparaît au-dessus de la température critique T_c. Or cet état lui-même présente, en dessous d'une certaine température T^*, des particularités remarquables, et c'est de cela que nous parlent Philippe Bourges et al. La phase stable entre T_c et T^* est traditionnellement appelée phase à pseudo-gap pour des raisons que nous n'exposerons pas. Elle se caractérise notamment par une surface de Fermi très différente de la surface de Fermi à $T > T^*$ [1–3]. On aimerait pouvoir caractériser la phase pseudo-gap par des propriétés structurelles (par exemple électroniques). Or

c'est précisément l'objet de l'article de Bourges *et al.* Les auteurs pensent avoir confirmé par diffraction de neutrons polarisés une théorie de Varma selon laquelle certains électrons sauteraient d'un atome à l'autre en décrivant des trajectoires fermées (boucles). C'est là une chose inhabituelle. On imagine d'ordinaire les électrons de conduction se déplaçant en ligne droite et les électrons localisés tournant autour d'un noyau. Les boucles interatomiques de Varma constituent des moments magnétiques aussi bien que les boucles intra-atomiques, et ces moments magnétiques, selon les observations des auteurs, s'ordonnent en une structure antiferromagnétique. Ce magnétisme dans lequel le spin ne joue aucun rôle est une grande nouveauté. La coïncidence du pseudo-gap avec ce magnétisme de nature nouvelle est une constatation expérimentale, mais il reste à déterminer si elle a une cause physique profonde.

Le deuxième article du présent numéro spécial, écrit par Hélène Montes et François Lequeux (prix de la fondation d'entreprise Michelin), est consacré aux matériaux qui constituent par exemple nos pneumatiques : des élastomères renforcés par l'inclusion de particules rigides destinées à améliorer leurs qualités mécaniques, notamment leur résistance à l'usure. Les auteurs commencent par décrire les propriétés de l'élastomère pur, qui est un matériau viscoélastique, c'est-à-dire pourvu à la fois de viscosité et d'élasticité. Sa réponse à une contrainte dépendant du temps est décrite par le module de relaxation E(t) qui, comme le module élastique E (encore appelé module d'Young) et le module de cisaillement, s'exprime en Pascals. Les auteurs introduisent un modèle, basé sur la découverte des hétérogénéités dynamiques dans les verres à l'échelle de quelques nanomètres, qui décrit bien le comportement viscoélastique d'un élastomère homogène à partir de l'hypothèse d'une structure en domaines. Ils s'attaquent ensuite aux élastomères renforcés par des particules rigides. Ils montrent que ces particules sont reliées mécaniquement par deux sortes de liaisons : des ponts vitreux et des ponts caoutchouteux ; l'état vitreux et l'état caoutchouteux d'un élastomère diffèrent par la valeur du module de cisaillement, de l'ordre du GPa dans le premier cas et du MPa dans le second. Les auteurs appliquent notamment leurs idées à l'effet Payne, phénomène non linéaire qui entraîne une dissipation d'énergie élevée dans les élastomères renforcés.

Le troisième article présenté ici est l'œuvre d'Etienne Perret (prix Espoir-IMT). Il illustre la présence croissante des robots dans notre vie, présence qui ne serait pas possible sans la complicité des physiciens. Il y a un siècle, quand on allait chez l'épicier acheter un pot de crème fraîche et une paire de chaussettes, l'épicier devait pour calculer le prix faire l'addition avec un crayon et une feuille de papier, ce qui demandait du temps et comportait des risques d'erreur. Un demi-siècle plus tard, l'épicier avait acquis une machine qui faisait les additions, une sorte de robot très spécialisé. Comme le robot ne savait pas lire, l'épicier devait lui indiquer les nombres à additionner. Il fallait moins de temps et le risque d'erreur était moindre, mais non nul. Aujourd'hui, quand nous allons au supermarché acheter une dizaine d'articles, il suffit de présenter successivement les 10 codes-barres à un robot lecteur qui se charge de la lecture et des additions. Le code-barre est une étiquette qui porte une information simple dans un langage que le robot peut lire plus facilement que les chiffres arabes et l'alphabet latin. De plus, si le supermarché décide de modifier le prix, il peut le faire sans changer l'étiquette. Dans ce dialogue entre une étiquette et un robot lecteur, le robot peut être extrêmement perfectionné et recevoir des ordres de l'autre bout du monde, mais l'étiquette doit être aussi bon marché que possible. Perret et ses collaborateurs remplacent la lecture optique du code-barre ou du QR code (Quick Reading) par une lecture par ondes électromagnétiques à fréquence radio, ce qui permet par exemple de lire des informations dissimulées par une enveloppe opaque. Cela implique évidemment le remplacement du code barre par une étiquette d'un autre genre. De telles étiquettes existent déjà. Elles font appel à la technologie RFID [identification radiofréquence], qui équipe les tickets de bus sans contact, les forfaits de ski, les badges d'entrée dans les immeubles. Ces étiquettes, qui uti-

lisent des « puces » électroniques, ont le défaut d'être nettement plus chères que les codes-barres ou les QR codes. Perret et ses collaborateurs proposent des étiquettes sans puces, à bon marché, lisibles par ondes radio. On trouvera plus de détails dans une entrevue avec l'auteur, sur le site : https://imtech.wp.imt.fr/2020/11/24/prix-imt-academie-des-sciences-etienne-perret/… et bien entendu dans l'article du présent numéro spécial.

Ces trois articles donneront au lecteur une idée de la diversité de la recherche actuelle en physique.

Je remercie Antoine Georges, Marc-Henri Julien et Tim Ziman pour leur aide, ainsi que les auteurs.

Jacques Villain
Editor-in-Chief
jvillain@infonie.fr

References

[1] A. Kanigel *et al.*, "Evolution of the pseudogap from Fermi arcs to the nodal liquid", *Nat. Phys.* **2** (2006), p. 447-451.
[2] S. E. Sebastian, C. Proust, "Quantum Oscillations in Hole-Doped Cuprates", *Annual Review of Condensed Matter Physics* **6** (2015), p. 411-430.
[3] M. Hartstein *et al.*, "Hard antinodal gap revealed by quantum oscillations in the pseudogap regime of underdoped high-T_c superconductors", *Nat. Phys.* **16** (2020), p. 841-847.

Comptes Rendus
Physique
2021, 22, nº S5, p. 7-31
https://doi.org/10.5802/crphys.84

Prizes of the French Academy of Sciences 2020 / *Prix 2020 de l'Académie des sciences*

Loop currents in quantum matter

Philippe Bourges *, [a], **Dalila Bounoua** [a] **and Yvan Sidis** [a]

[a] Université Paris-Saclay, CNRS, CEA, Laboratoire Léon Brillouin, 91191, Gif-sur-Yvette, France

E-mails: philippe.bourges@cea.fr (P. Bourges), dalila.bounoua@cea.fr (D. Bounoua), yvan.sidis@cea.fr (Y. Sidis)

Prix CEA « science et innovation » de l'Académie des sciences 2020

Abstract. In many quantum materials, strong electron correlations lead to the emergence of new states of matter. In particular, the study in the last decades of the complex phase diagram of high temperature superconducting cuprates highlighted intra-unit-cell electronic instabilities breaking discrete Ising-like symmetries, while preserving the lattice translation invariance. Polarized neutron diffraction experiments have provided compelling evidences supporting a new form of intra-unit-cell magnetism, emerging concomitantly with the so-called pseudogap state of these materials. This observation is currently interpreted as the magnetic hallmark of an intra-unit-cell loop current order, breaking both parity and time-reversal symmetries. More generally, this magneto-electric state is likely to exist in a wider class of quantum materials beyond superconducting cuprates. For instance, it has been already observed in hole-doped Mott insulating iridates or in the spin liquid state of hole-doped 2-leg ladder cuprates.

Keywords. Loop-current, Quantum matter, Polarized neutron diffraction, High-temperature superconductors, Pseudo-gap, Magnetic correlations.

Available online 7th September 2021

1. Introduction

Strong electron correlations in condensed matter lead to the emergence of novel phenomena and exotic states. None of these collective phenomena is encompassed by the simple addition of individual electrons but results instead from many-body effects as it was advocated by Anderson almost 50 years ago [1]. Spin liquids, Mott physics, strange metals, high-temperature superconductivity and its related pseudogap phase are all typical examples of these novel states of matter, generically labeled as quantum matter.

The study of the complex phase diagram of hole-doped superconducting cuprates highlighted the existence of a mysterious state of matter, the so-called pseudogap (PG) metal [2–4], where large portions of the Fermi surface are gapped out and only Fermi arcs survive. The PG state is characterized by a significant loss of electronic entropy [5] below a certain temperature, so-called T^*, in the phase diagram, as represented in Figure 1. On cooling down, unconventional

* Corresponding author.

superconductivity with a d-wave symmetry occurs and seems to emerge out of the PG state. Furthermore, deep inside the PG state, an incipient charge density wave (CDW), with a d-wave structure factor, competes with superconductivity [2,3], while strong antiferromagnetic (AF) spin fluctuations are still present in the materials. The incipient CDW breaks the lattice translation (LT) symmetry and gives rise to a new periodicity associated with its modulation wave vector $\mathbf{q}_c \neq 0$. It coexists with a set of intra-unit-cell (IUC) electronic instabilities which preserve the LT invariance ($\mathbf{q} = 0$) (see e.g. [6–8]), but break discrete Ising-like symmetries: the fourfold rotation (R) symmetry for an electronic nematic state and additionally, time reversal (T) and parity (P) symmetries, as we shall discuss in details here. Remarkably, these different IUC orders show up concomitantly with the PG state. They are then necessarily tied up with it and should also be associated with a significant energy condensation. It should be stressed out that no additional noticeable change of the electronic entropy is reported below T^*, of course apart from the one associated with superconductivity [5]. This is, for instance, the case for states like the CDW occurring within the PG state. A central question is therefore which one of these order parameters is the primary one? It should be also stressed that there are two known mechanisms to open gaps in metals, either it results from a finite $\mathbf{q} \neq 0$ ordering breaking LT or it is due to a particle–particle pairing as does superconductivity. Therefore, none of the IUC broken symmetries alone can induce the needed fermionic gap characterizing the PG state.

To get a better understanding about these IUC orders, it is useful to look at the basic atomic structure of superconducting cuprates. They are layered perovskite materials, made of the stacking of CuO_2 layers, whose building block is a CuO_2 squared plaquette (Figure 3a–c). In the insulating undoped state, there is only a single electron on the Cu site carrying a half-integer spin $S = 1/2$. Upon hole doping, an extra hole on the O site can form a bound state with the electron on the Cu site, yielding the so-called Zhang–Rice singlet [9]. Owing to the strong on-site Coulomb repulsion which prevents a second hole to enter the plaquette, one is left with a set of three states for the CuO_2 squared plaquette, useful to build a minimum model (such as the widely studied $t-J$ model) for cuprates, but which also eliminate the internal degrees of freedom within the CuO_2 plaquette. In contrast, the IUC electronic orders imply the emergence of non-Zhang–Rice singlet states [10]. For an electronic nematic state, an unbalanced electronic density at the O sites breaks the fourfold R-symmetry of the CuO_2 plaquette, as observed in scanning tunneling microscopy (STM) [7,8].

Put altogether, the IUC symmetry breakings point towards novel electronic states that have been proposed either to account for or to characterize the PG state. That takes in particular the forms of loop currents (LCs) flowing coherently between copper and oxygen orbitals [4] as depicted in Figure 2a,b. LC states can take different shapes [23–28], where the electronic density remains uniform, but spontaneous charge currents appear between Cu and O sites within the CuO_2 plaquette. The circulating loop currents spontaneously break T-, P- and/or R-symmetries. The search for states of matter involving charge currents is a long story in the physics of high temperature superconductors and various states of matter were proposed. Unlike IUC and LC states (both being $\mathbf{q} = 0$ electronic instabilities), charge current density wave ($\mathbf{q} \neq 0$ electronic instability) were also proposed [29]. For instance, within a single band Hubbard model, charge currents were predicted to flow around the CuO_2 square lattice, yielding the so called "π-flux phase" or D-density wave (DDW) [30,31] which doubles the unit cell. As the π-flux phase breaks the LT symmetry, additional superstructure Bragg reflections are expected at several $\mathbf{Q}$-points in the reciprocal space equivalent to (π,π) [30,31]. Despite various attempts in different sets of samples, neutron diffraction measurements failed to prove the existence of magnetic peaks at the planar wave vector $(1/2,1/2) \equiv (\pi,\pi)$ in the 2D first Brillouin zone. As a generic property, all the types of charge current phases break T-symmetry and closed current loops generate a magnetic flux and orbital magnetic moments. That is the primary property reported to provide

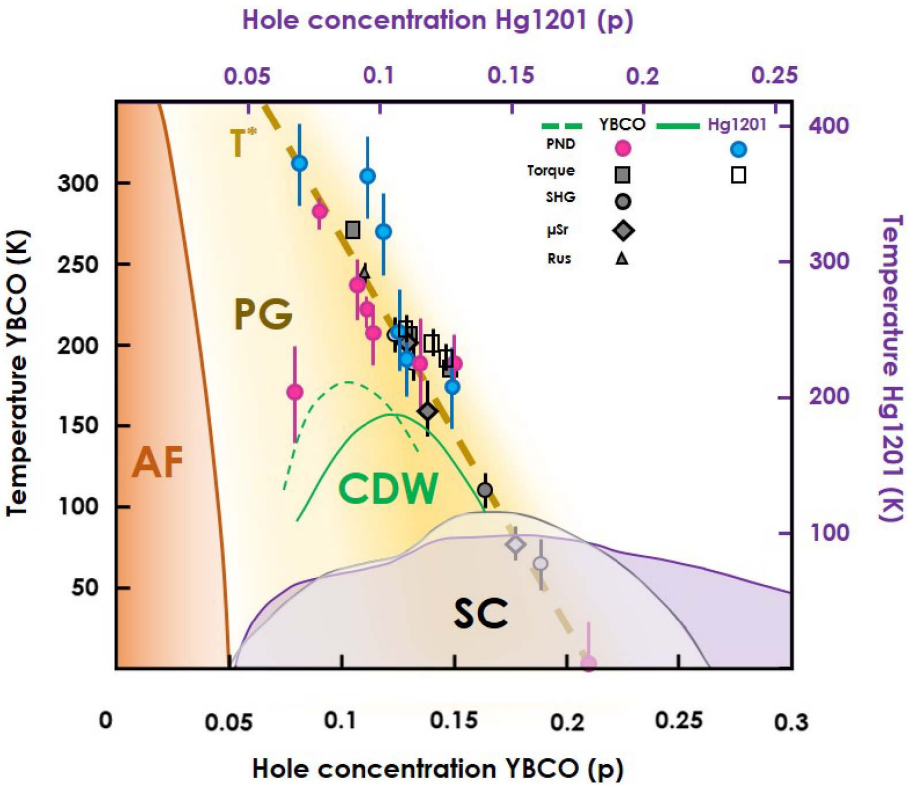

Figure 1. High-T_c superconducting cuprates phase diagram versus hole concentration for two cuprates families $YBa_2Cu_3O_{6+x}$ (YBCO) (bottom and right scales) and $HgBa_2CuO_{4+\delta}$ (Hg1201) (top and left scales) showing the intra-unit cell (IUC) magnetic order associated with the pseudogap state from polarized neutron diffraction (PND) [6, 11–17] and T^*, the pseudogap temperature, determined from torque [18, 19], second harmonic generation (SHG) [20], muon spectroscopy (μSR) [21] and resonant ultrasound (Rus) [22] experiments. Representative lines of transition of antiferromagnetism (AF), superconductivity (SC), pseudogap (PG) and charge density wave (CDW) (full line for YBCO and dashed line for Hg1201) are also depicted. The vertical and horizontal scales have been adapted to match T^* in both materials.

evidence in favor of the LC states in various quantum materials, and which experimentalists have tried to evidence by using dichroic effect using circularly polarized angle resolved photoemission (ARPES) [32] and next by looking for the LC induced orbital magnetism using polarized neutron diffraction (PND) as we shall review here in Section 2. To date, the LC state has been reported in several oxide materials either with 2D structure, in the superconducting cuprates [6,11–17,33–35] and in the iridates [36], or in the 1D spin ladder cuprate [37], showing the universal nature of this exotic state.

In this article, we next list in Section 3 the various experimental data (other than PND) that support the emergence of such LC states built from the LC-Θ_{II} pattern represented in Figure 2a. In particular, the macroscopic torque measurements in two cuprates families, namely in bilayer $YBa_2Cu_3O_{6+x}$ and monolayer $HgBa_2CuO_{4+\delta}$, [18, 19], although showing different results, match nicely the PND experiments [14, 15].

The remainder of the manuscript focuses in Section 4 on the interplay with the PG state, which

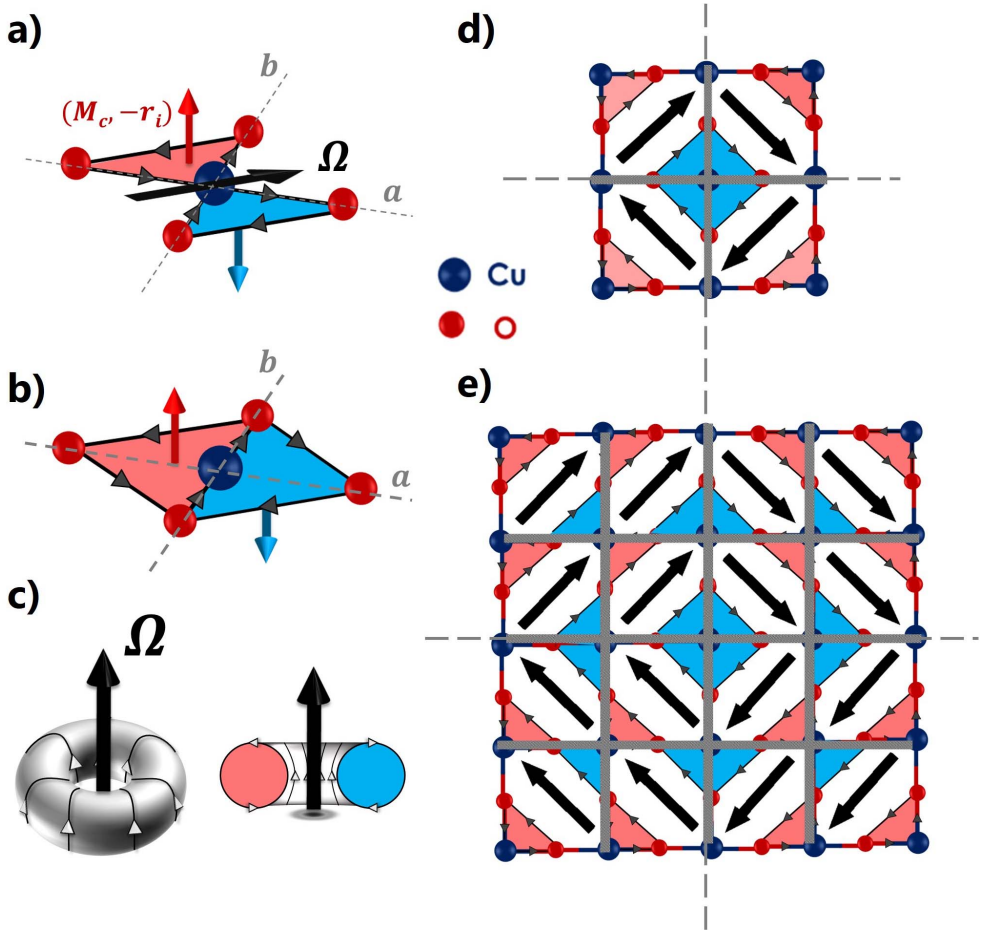

Figure 2. (a) Loop currents (LC) in CuO_2 plane, so-called LC-Θ_{II} phase, as proposed by Varma in superconducting cuprates [24, 25], with the corresponding toroidal moment, Ω, in black. (b) Model of loop currents proposed in Ref. [38]. The LCs now only run between oxygen sites, in contrast with the LC-Θ_{II} phase. (c) Anapole or polar toroidal moment Ω formed by winding current around a solenoid. A 2D section in the torus reveals two loop currents turning clockwise (blue) and anti-clockwise (red). (d) $(2P \times 2P)$ anapoles vortex crystal formed by LC-Θ_{II} supercells [28] obtained from a $\pi/2$ rotation of the anapole moment (in black) between neighbouring unit-cells. The magnetic cell encompasses the 4 possible domains for a LC pattern separated by domain walls (represented by the shaded lines). Here, the domains size as a function of the unit-cell is $P = 1$. (e) $(2P \times 2P)$ magnetic supercell for $P = 2$.

depends on the hierarchy among the various co-existing/competing observed phases. LCs can be bound to the PG physics in two ways. First, the LC phase is degenerate and several states corresponding to distinct LC patterns are allowed [25]. This degeneracy can be the source of a proliferation of randomly distributed LC domains. Assuming the existence of a super-cell made of a coherent juxtaposition of LC domains [28] (as shown by Figure 2d,e), the LT invariance would be broken and this modulated ($\mathbf{q} \neq 0$) LC-based phase could trigger a gap opening on the Fermi surface. Following a fundamentally different approach, the LC order can also be understood in

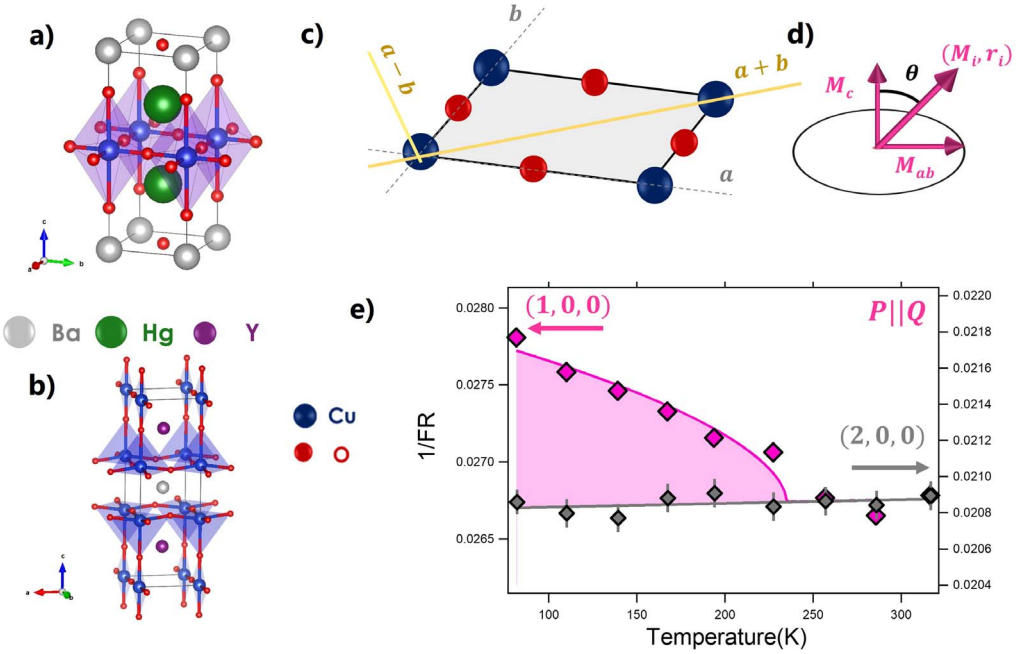

Figure 3. Crystal structure of layered perovskites (a) $HgBa_2CuO_{4+\delta}$ and (b) $YBa_2Cu_3O_{6+x}$. (c) CuO_2 plane with copper (blue circles) and oxygen (red circles) atoms. (d) Tilt of the observed magnetic moment. The magnetic moment is tilted by an angle θ from the c-axis direction, perpendicular to the CuO_2 plane. (e) Temperature dependencies of the inverse of the flipping ratio 1/FR (see text) measured at $\mathbf{Q} = (1,0,0)$ (purple) and at $\mathbf{Q} = (2,0,0)$ (gray), **P** is the neutron polarization parallel to **Q** to maximize the magnetic intensity (from [14]).

terms of a so-called "ancillary state" inseparable from the PG state [38–41]. The ancillary state is a secondary instability associated to a mother instability which itself effectively opens the PG. For instance, it can correspond to pair-density-wave (PDW) states [39–41]. Within these approaches, it was first pointed out by Agterberg *et al.* [39] that the LC phase necessarily happens owing to the symmetry and is therefore essential to capture the specific nature of the PG. We conclude in Section 5 with some perspectives for future experimental developments.

2. Polarized neutron diffraction experiments

Hunting for LCs, we have performed PND experiments on several correlated materials over the last 15 years. We here discuss layered perovskite materials with a (nearly) tetragonal structure within the **ab** basal plane corresponding to the (CuO_2 or IrO_2) layers (Figure 3c), stacked along the **c**-axis. The structural unit-cell contains one or more layers, depending on the materials, yielding different c lattice parameter. Examples of the corresponding crystallographic structure are shown in Figure 3a,b. The PND technique is a momentum-selective probe for magnetism. We commonly write, see e.g. Ref. [6], the measured momentum as $\mathbf{Q} = (H,K,L)$ in reduced lattice units $(2\pi/a, 2\pi/b, 2\pi/c)$ with $a \sim b \sim 3.85$ Å. Various attempts to observe the different orbital magnetic moments associated with the charge currents (π-flux or D-density wave) phase have been already discussed in [42,43].

2.1. *The IUC ($\boldsymbol{q} = 0$) magnetism*

Unlike the π-flux phase, the staggered orbital magnetism induced by the Varma's LCs [23–25] is associated with a set of pairs of charge currents looping clockwise and anticlockwise within each unit cell, Figure 2a [44]. Such a LC state preserves the LT symmetry, so that, in a diffraction experiment its magnetic Bragg reflections are superimposed to the structural Bragg reflections. This makes the experiments particularly difficult, as the magnetic contribution is weak, and polarized neutrons are required to discriminate between the structural and magnetic scatterings on a Bragg reflection. Indeed, any source of magnetism in the sample is able to flip the neutron spin, i.e. changing the spin polarization of the scattered neutron beam. To determine a possible orbital magnetic order, one needs to measure the variation of the neutron polarization versus temperature. A long range magnetic order would give rise to an upturn of the so-called inverse flipping ratio, 1/FR, which measures the ratio of magnetic to structural scatterings when the neutron polarization is set parallel to the scattering wavevector [6, 43]. A typical result is reported in Figure 3e where 1/FR ratio is shown versus temperature in the bilayer cuprate $YBa_2Cu_3O_{6.6}$ [14]. Two Bragg peaks are measured: at large $\mathbf{Q}$, (2,0,0), where the magnetic signal should vanish, an expected smooth thermal variation is reported whereas an upturn is observed around $T \simeq 235$ K at low $\mathbf{Q}$ = (1,0,0). This corresponds to the occurrence of a spontaneous magnetic signal. Assessment of the technical difficulties and limitations related to the PND experiments have been recently re-emphasized in [45].

Numerous PND measurements reveal the appearance of a $\mathbf{q} = 0$ antiferromagnetic order at the Bragg reflections $\mathbf{Q} = (1, 0, L)$ [43], also referred to as IUC magnetism [44]. This order displays a magnetic structure factor consistent with the orbital staggered magnetism produced by the LC-Θ_{II} state within the CuO_2 planes. In the field of unconventional high temperature superconductors, we reported such observations in four distinct cuprate families: $YBa_2Cu_3O_{6+x}$ [6, 11–14], $HgBa_2CuO_{4+\delta}$ [15–17], $(La,Sr)_2CuO_4$ [33], and $Bi_2Sr_2CaCu_2O_{8+\delta}$ [34, 35]. Figure 1 groups, in a generic phase diagram, the magnetic ordering temperatures measured by PND in the monolayer $HgBa_2CuO_{4+\delta}$ and bilayer $YBa_2Cu_3O_{6+x}$ compounds, as a function of the hole doping.

Later, we also reported an IUC magnetism in the large spin–orbit coupled Mott insulators, $Sr_2(Ir,Rh)O_4$ monolayer iridates [36], suggesting a more generic character of such LC orders in correlated electron oxides. It is worth noting that both iridates (Ir, 5d) and cuprates (Cu, 3d) are AF insulators which can be doped (Mott or charge-transfer insulators, respectively, and $S = 1/2$ on Cu versus $J = 1/2$ on Ir). Likewise, they share a similar layered perovskite structure. A noticeable difference with the 2D cuprates is that the LC occurs as well in the insulating compounds at half-filling, whereas in cuprates it is so far only observed in the doped metallic and superconducting materials, i.e. for a doping $\gtrsim$8% [12]. It is worth stressing out that the mechanism that could be invoked to produce LC state could differ in both oxides.

Despite the large body of PND data supporting an IUC magnetism in superconducting cuprates, its existence was questioned by a PND attempt [46], which failed to detect it in small $YBa_2Cu_3O_{6+x}$ single crystals (weighing less than 18 mg in contrast with our samples which weighted at least 2000 mg [47]). Due to the limited flux of polarized neutron beams and the relatively weak orbital magnetic moments, we demonstrated in [45, 47] that the experimental accuracy in [46] was clearly insufficient to draw any conclusions from the data as a consequence of the one well-known drawback of neutron scattering, which is the systematic need of large enough sample volume.

The PND results prove that the T-symmetry is broken when entering the PG phase of high-T_c superconducting cuprates, consistent with the LC-Θ_{II} phase symmetry (Figure 2a) originally proposed by Varma [24, 25]. The deduced spontaneous orbital magnetic moment is typically of the order of ~$0.1\mu_B$ per loop of the LC-Θ_{II} phase [43] and its magnitude decreases with increasing

hole doping following the trend of the pseudogap [6,35]. In general, it should be stressed out that PND data can be interpreted by a large number of magnetic models as long as these models produce compensated magnetic moments within a given unit cell and respect the LT symmetry. This is the case for instance for the Dirac multipole ordering proposed in Refs. [48–50], which we will discuss below. To conclude, a model accounting for the PND data needs at least two opposite magnetic moments in each unit cell, to comply with the $\mathbf{q} = 0$ antiferromagnetic structure.

2.2. *Magnetic moment direction*

The direction of the magnetic moments is experimentally determined through the neutron polarization analysis [43], from which one can deduce the magnitude of the out-of-plane component ($\mathbf{M}_c$) and the in-plane component ($\mathbf{M}_{ab}$). In the LC-$\Theta_{\rm II}$ phase, the orbital magnetic moments should be perpendicular to the CuO_2 plane in which LCs are confined (Figure 2a,b). However, as sketched in Figure 3d, the outcome of the PND analysis is a $\Theta \sim 40 \pm 20°$ tilt angle of the magnetic moment with respect to the **c** axis. While systematically observed in all 2D cuprates [17], Θ can vary noticeably between the cuprates, as well as in function of the measured momentum **Q**-points. Interestingly, the moment tilt could also be temperature dependent [13]. Furthermore, as sketched in Figure 3d, the exact orientation of $\mathbf{M}_{ab}$ in the ab plane has not been determined experimentally yet. As a general remark, the observed tilt is not well accounted for by most of the theoretical models proposed for the IUC magnetism, as we shall see below. The observed tilt is certainly a key and unexpected feature of the observed IUC magnetism, putting stringent constraints on theoretical models.

2.3. *IUC spatial correlations*

Before, going further in the discussion, it is worth emphasizing some experimental limitations of the neutron scattering technique. Generally speaking, the neutron scattering cross-section is convoluted with the instrumental resolution of the instrument in 4 dimensions ($\mathbf{Q}$, ω) [51]. The determination of the correlation length and characteristic time scale are limited by the instrument resolution. In order to detect a weak magnetic response, one usually relaxes the resolution. Likewise, a modulated structure, with a very long pitch, λ, gives rise to satellite reflections very close to the Bragg spot. These satellite scatterings can merge with the Bragg scattering owing to the experimental resolution. The canonical example is the long period helimagnet MnSi with $\lambda \sim 180$ Å, [52], for which the observation of the magnetic satellites requires the use of a very good resolution for diffraction measurements or the use of small angle neutron scattering techniques. In the latter case, the measurement is not performed around a Bragg reflection at finite $\mathbf{Q}$ ($\neq 0$) anymore, but around $\mathbf{Q} \rightarrow 0$. For LC-like magnetism, whose magnetic structure factor cancels for $\mathbf{Q} \rightarrow 0$, small angle neutron scattering is unfortunately unsuited.

In three of the cuprates families, namely $YBa_2Cu_3O_{6+x}$, $HgBa_2CuO_{4+\delta}$ and $Bi_2Sr_2CaCu_2O_{8+\delta}$, the observed IUC magnetism superimposes to the atomic Bragg peak [6, 15, 34, 43], suggesting that the IUC order is long range and 3D as it is clearly established in underdoped $YBa_2Cu_3O_{6.6}$ [11]. Due the relaxed instrument resolution that was used, only an upper limit of the correlation length along the c axis $\xi_c \leq 75$ Å could be given [11, 43]. As in MnSi, a situation with magnetic satellites with a long magnetic pitch could happen. Various attempts to observe a magnetic response in the reciprocal space distant from the Bragg position were however unsuccessful, giving a lower limit of a possible pitch of $\lambda \gtrsim 40$ Å. In an nearly optimally doped $YBa_2Cu_3O_{6.85}$ sample only, an IUC magnetic signal could be detected broader than the in-plane momentum resolution [13]. This indicates short range correlations with finite in-plane correlation lengths, $\xi_{ab} \sim 20a \sim 80$ Å in that compound.

A particularly interesting case is that of $La_{2-x}Sr_xCuO_4$, a system which is known to experience a segregation of doped holes into charge stripes [53]. For Sr substitution close to $x = 1/12$, we observed an IUC magnetic signal that remained quasi-2D with short range correlation lengths [33]. This contrasts with observations in other cuprates where a (quasi) long range IUC magnetism develops at 3D. This short range magnetism in lightly doped $La_{2-x}Sr_xCuO_4$ can be associated with very weak correlation lengths of LC-Θ_{II} 1D ribbons (~10 Å, i.e 2–3a). The short range magnetism can be viewed as LC-Θ_{II} objects confined on the charge stripes separated by hole poor AF domains of Cu spins, in relation with the charge order in this material [43, 53]. LCs can therefore interact with other electronic instabilities and persist in low dimensional systems (1D).

Following this observation and theoretical predictions [38, 54], we recently studied the 2-leg ladder cuprate $Sr_{14-x}Ca_xCu_{24}O_{41}$, which is an archetype of 1D spin liquids. This aperiodic system hosts a very rich phase diagram where, depending on the Ca content (which induces hole doping), it exhibits a strong spin liquid state ending into an intriguing ordered magnetic state at larger Ca content, passing through a CDW phase. Using PND, we discovered the existence of 2D short range magnetism in this material for two Ca contents [37]. This magnetism cannot be described by any type of Cu spins ordering. Instead, our investigations establish the existence of LC correlations within the 2-leg ladders [37]. The results from both studies suggest that LCs could be confined within quasi-1D structures, such as 2-leg Cu ladders, imposed either by the structure of the material in $Sr_{14-x}Ca_xCu_{24}O_{41}$ or by an electronic phase segregation yielding the formation of (bond centered-) stripes in $La_{2-x}Sr_xCuO_4$.

2.4. *L-dependence of the IUC magnetic structure factor*

The L dependence of the magnetic scattering associated with the IUC order has been reported for wavevectors $\mathbf{Q} = (1,0,L)$ in two monolayer compounds $HgBa_2CuO_{4+\delta}$ [15] and $La_{2-x}Sr_xCuO_4$ [33]. In the former, the magnetic signal from IUC order is only at integer L values, while it remains 2D (any L values) for the latter. Surprisingly, the scattered magnetic intensity displays the same fast decay as a function of L [34]. In principle, in bilayer compounds, in-phase or out-of-phase coupling between layers would give rise to a magnetic structure factor modulated either by a term $4\cos^2(\pi zL)$ or $4\sin^2(\pi zL)$, where $z(= d/c)$ stands for the reduced interlayer distance. Instead, the IUC magnetic pattern in $YBa_2Cu_3O_{6+x}$ exhibits a crisscrossed stacking of the IUC patterns [14] (as illustrated in Figure 5b), so that the L-dependence associated with the bilayer vanishes in the magnetic structure factor when dealing with a twinned crystal. Accordingly, the L-dependence of the scattered magnetic intensity measured in bilayer systems like twinned $YBa_2Cu_3O_{6+x}$ and $Bi_2Sr_2CaCu_2O_{8+\delta}$, matches that found for monolayer cuprates [34]. Furthermore, the calibration of the magnetic intensity measured on Bragg reflections with similar $|\mathbf{Q}|$ and in comparable samples, (i.e. at similar T^* and doping levels) indicates that the intensity for 2 Cu/f.u is only twice larger than the one measured for a single Cu/f.u, as if the (bi)layers were decoupled. Such a ratio is well acounted for by a crisscrossed arrangement of LCs within a bilayer [14].

The fast decay of the magnetic intensity along L observed in all cuprates is actually much faster than the one controlled by $|f(\mathbf{Q})|^2$ the squared magnetic form factor of Cu or O single ion [34]. This phenomenon could then be accounted for by IUC magnetic moments being spread out within the CuO_2 layer. In this picture, LCs would not be simply confined within the CuO_2 layers. They would be more delocalized than a magnetic moment bound to a single ion, giving rise to a faster decay of the IUC structure factor along the out-of-plane direction. This interpretation seems to be supported by the study carried out on twin-free samples: in this case, the scattered intensities along $(1,0,L)$ and $(0,1,L)$ differ and are weighted by $4\cos^2(\pi zL)$ and $4\sin^2(\pi zL)$,

respectively [14]. However, the observed ratio between the magnetic IUC intensities measured along a and b is not quantitatively reproduced with the reduced Cu–Cu distance, $z = 0.28$. A larger value of z provides a better result, suggesting that the magnetic moments could be located outside the CuO_2 layer. Such a property has not been observed yet in other materials exhibiting IUC order, such as iridates or 2-leg ladder cuprates.

3. Symmetry considerations

In both cuprates and iridates, PND shows the existence of an IUC magnetism, whose characteristic properties are consistent with the LC-Θ_{II} phase pattern breaking discrete T-, P- and four-fold R-symmetries. In addition to PND, complementary evidences of such broken symmetries were reported by other techniques, ranging from dichroism in circularly polarized ARPES spectroscopy [32], Kerr effect [55], Nernst effect [56], optical birefringence measurements [57], second harmonic generation (SHG) [20, 58], torque [18, 19, 59] and recently photo-galvanic effects [60], respectively. The Kerr effect was reported in cuprates and necessarily implies a global T-broken symmetry although this happens in $YBa_2Cu_3O_{6+x}$ [55] at a slightly lower temperature than the other experimental probes [6, 18, 20, 56, 57]. Each technique brings complementary information to draw the portrait of the IUC order and to guide theoretical models.

3.1. *Anapoles and quadrupoles*

The LC-Θ_{II} state is the ground reference of the observed IUC magnetic order. It is characterized by T- and P-symmetry breaking (although their product is preserved) [24, 25]. This view was reinforced in cuprates [58] and put forward in iridates [20] by the observation of P-symmetry breaking in SHG experiments at the same temperature as the T-symmetry breaking for a given doping. The LC-Θ_{II} magnetic pattern is described by two staggered orbital magnetic moments $\mathbf{M_i}$ located on a diagonal of the CuO_2 plaquette and equidistant from the Cu site. Within the basal lattice and for the state described in Figure 2a, the magnetic moments $\mathbf{M}_i = \pm(0, 0, \pm M_c)$ are then located at $\mathbf{r}_i = \pm(-r_0, r_0, 0)$. The LC-$\Theta_{II}$ exhibits, in principle, magneto-electric effects that can be described by a uniform arrangement of anapoles (also named: toroidal moments) [61]. The anapole Ω corresponds to a polar vector shown in Figure 2a constructed from the LC as,

$$\Omega = \sum_i \mathbf{r_i} \wedge \mathbf{M_i}. \tag{1}$$

In general, an anapole is described using a current flowing around a solenoid bent to form a torus (Figure 2c). The winding current around the solenoid generates a circular magnetic field inside the torus which gives rise to a pure anapole along the axis of the torus, according to the definition of Ω. In 2D, the 3D torus reduces to 2 LCs turning clockwise and anticlockwise. Actually, this staggered orbital magnetism supports not only an anapole, but also a magnetic quadrupole (3×3) tensor [62]. This is not surprising as the anapole appears at the same order of the magnetic multipole expansion as quadrupoles, as it is discussed in the context of multiferroics [62, 63]. More precisely, for the LC-Θ_{II} state, $\Omega = 2r_0M_c(\mathbf{a} + \mathbf{b})$ and the non-zero components of the magnetic quadrupole $Q_{ac} = Q_{bc} = r_0M_c$ [62].

LC-free models, involving Dirac multipoles, were actually developed to account for the IUC magnetic scattering reported by PND [48–50]. The CuO_2 plaquette is not occupied anymore by an anapole bound to LCs flowing through Cu and O, but by magnetic quadrupoles localized on the Cu site. Symmetry arguments are used to select the allowed magnetic quadrupoles, which can further ensure the P- and T-symmetries breaking [48–50]. Unlike electronic multiferroics where the charge and magnetic degrees of freedom form two distinct order parameters, these theoretical models predict the existence of new magneto-electric objects, in which the magnetic

and electronic degrees of freedom are intimately coupled to form a single exotic order parameter, for instance due to electron–phonon coupling [50].

Similarly to the magnetic distribution of the LC-Θ_{II} state, a magnetic distribution with only in-plane magnetic moments can be considered as well [62]: this corresponds to a pure magnetic quadrupole which is generated by a set of magnetic dipoles. Keeping the same notation as for the LC-Θ_{II} state, one could consider two magnetic moments $\mathbf{M}'_i = \pm(-M_{ab}, M_{ab}, 0)$, again located at $\mathbf{r}_i = \pm(-r_0, r_0, 0)$. The non-zero components of the magnetic quadrupole are $Q_{aa} = (1/3)Q_{ab} = -(1/2)Q_{cc} = (2/3)r_0 M_{ab}$ [62] and differ from the ones of the quadrupole above. These planar magnetic moments do not generate an anapole. The existence of such a magnetic quadrupole could then explain the observed in-plane component ($\mathbf{M}_{ab}$) of the IUC magnetism reported by PND, whereas the original LC-Θ_{II} state can only explain the measured out-of-plane component ($\mathbf{M}_c$). As one observes experimentally a tilted IUC moment, none of these magnetic distributions alone can describe the PND results. However, a combination of these two pictures could account for the tilted IUC moment as we shall see below (Section 3.3).

3.2. *Degeneracy of LC-Θ_{II} state*

It is worth emphasizing that the LC-Θ_{II} phase is characterized by four degenerate quantum states. The four LC patterns are deduced from each other by a 90° rotation with the anapole pointing along all diagonals of the basal plane [64, 65]. They produce four types of magnetic domains that will be summed up in bulk PND experiments (Figure 3e). If one considers a classical LC model, each of the LC domains gives a magnetic scattering in PND corresponding to magnetic moments perpendicular to the CuO_2 layer. In contrast, if a quantum superposition of the four LC states is allowed, then an effective planar magnetic response can appear as a result of quantum interference in the neutron scattering cross-section [65]. Therefore, the existence of the in-plane magnetic response could highlight the quantum effects in the LC state. The observation of a temperature dependent tilt angle in nearly optimally doped $YBa_2Cu_3O_{6.85}$ [13] could suggest a crossover from classical to quantum LC states, when thermal fluctuations are overcome by quantum ones. Within that scenario, quantum effects would then occur at relatively high temperature, around 200–250 K. This might be surprising unless the PG itself could impose the quantum superposition of the LC states which in turn produce the observed tilt [65].

3.3. *IUC point group symmetry*

Considering the simple crystal structure of a tetragonal monolayer system, such as $HgBa_2CuO_{4+\delta}$ (see Figure 3a), the LC-Θ_{II} state belongs to the magnetic point group $m'mm$ [25, 66] (m' is a mirror plane followed by a time reversal operation). The three mirror planes are respectively: the (**a+b**, **a-b**), (**a+b**, **c**) and (**a-b**, **c**) planes. Combining the above discussed magnetic distributions, one can build the magnetic pattern reported in Figure 4a with two magnetic moments $\mathbf{M}_i = \pm(M_{ab}, M_{ab}, M_c)$. This magnetic arrangement corresponds to a rotation of the LC-Θ_{II} magnetic pattern around the **(a-b)** diagonal axis, yielding a monoclinic magnetic point group $2/m'$ (as the rotation preserves the m' mirror plane) [66]. The magnetic pattern shown in Figure 4a differs from the one shown in Figure 4b where the planar magnetic component is aligned along the **(a-b)** axis (the moments are tipped out of the plane of the M_c components). The latter magnetic pattern has a magnetic point group $2'/m$ [66]. Note that the planar magnetic components of Figure 4b cannot be associated with a pure magnetic quadrupole only as in Figure 4a. Indeed, they give a contribution to an anapole ($-4r_0 M_{ab}\mathbf{c}$), in addition to the magnetic quadrupole ($Q_{aa} = -Q_{bb} = 2r_0 M_{ab}$). While being distinct, the magnetic patterns reported in Figure 4 produce hardly distinguishable neutron scattering cross-sections and fully account for the observed IUC

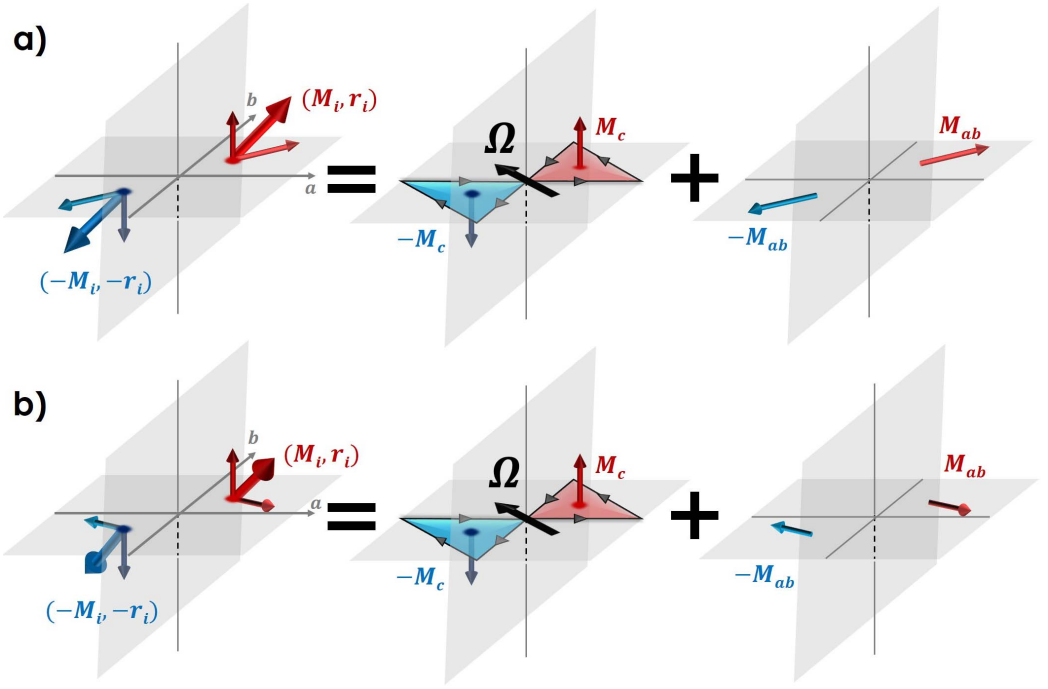

Figure 4. Representation of two possible magnetic moment arrangements which are compatible with the PND results. They correspond to a superposition of out-of-plane moments as the LC-Θ_{II} phase [24,25] with in-plane moments either (a) along the diagonal joining up the moments, or (b) along the perpendicular diagonal. This leads to different symmetries with (a) $2/m'$ point group and (b) $2'/m$ point group. Note that, as in Figure 2a, only one of the four possible LC states is shown.

magnetism. It should be stressed out that the $2'/m$ point group was deduced from SHG results in $YBa_2Cu_3O_{6+x}$ [58] based on (i) the observed $2/m$ symmetry of the atomic structure at 300 K and (ii) the broken global inversion related to the absence of C_2 axis.

In order to account for the existence of an in-plane magnetic component, one could also relax the constraint that LCs have to be confined within the CuO_2 plaquette. In hole doped cuprates, the Cu site is located at the center of an O octahedron in monolayer compounds, which splits in O pyramids in bilayer ones. The LCs could then be delocalized on the faces of the CuO_6 octahedra or on the CuO_5 pyramids, yielding a natural tilt of their orbital moments. However, the PND experiments exclude the LC states occurring on the faces of the CuO_6 octahedra [26, 66, 67] or on the CuO_5 pyramids [68] because the basal plane cannot also be a mirror plane for the in-plane component $\mathbf{M}_{ab}$. Only the LC state decorating the CuO_6 octahedra with only two opposite moments, as shown in Figure 5a and represented in [39, 67], is compatible so far with the PND results in $HgBa_2CuO_{4+\delta}$ [15–17] and belongs to the $2/m'$ point group. It should be stressed that no LC model on the CuO_5 pyramids has been found to be consistent with the PND data in bilayer materials.

Beyond the LC approach, a (Cu-)quadrupole modelling of the PND data [48–50] is also proposed with a magnetic structure belonging to $m'm'm'$ point group. It is actually not consistent with the data, as the basal plane cannot have a m' symmetry plane for the $\mathbf{M}_c$ component. This is due to the measurement of the magnetic structure factor at the $\mathbf{Q}$-position for $L = 0$ where a larger tilt is typically deduced [11, 17]. Other possible quadrupole arrangements [50] are then designed

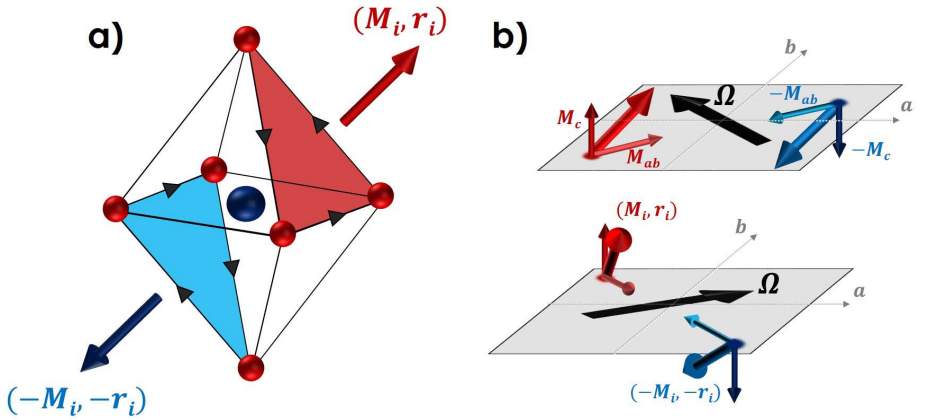

Figure 5. (a) Loop currents decorating a CuO_6 octahedron with two circulating loops [39, 67] which can describe the PND results in $HgBa_2CuO_{4+\delta}$ [15–17]. (b) Model of magnetic moments for a bilayer cuprate like $YBa_2Cu_3O_{6+x}$ built from the magnetic moment arrangement of a single layer shown in Figure 4a and compatible with the observed neutron structure factor [14].

to give a magnetic structure that belongs to the $2/m'$ point group.

In the bilayer $YBa_2Cu_3O_{6+x}$ system, the PND results in a twin-free sample [14] (see e.g. Figure 5b) are important as they rule out models [48, 50, 68], which assume either an in-phase or out-of-phase coupling of IUC order within a given bilayer. This dismisses models based on a magnetic nematic order, involving spin or orbital moments located at the O sites [6, 10] as well.

Linear and circular photo-galvanic effects recently observed at the PG temperature [60] in both monolayer and bilayer Bi-based cuprates suggest a $mm2$ point group symmetry, although monoclinic point group as $2/m'$ or $2'/m$ are also possible. A very interesting outcome of these experiments is the fact that the phase coherence of the IUC order should be as large as the size of the illuminated beam (~10 μm).

3.4. *Rotational symmetry breaking*

The different IUC phases proposed break R-symmetry. This can be tested in various experiments as, for instance, via the loss of both C_4 rotation and mirror symmetry in the electronic structure of the CuO_2 plane [57]. Indeed, the LC-Θ_{II} state imposes a preferential direction of the anapole along one of the diagonals of the CuO_2 plane. On the opposite, staggered LCs flowing on O sites only, as proposed in Refs. [38, 69], give a pattern rotated at 45° with respect to LC-Θ_{II} one and are characterized by an anapole along one of the CuO bonds (Figure 2b). However, owing to the formation of degenerate domains and assuming equal populations of the domains, PND cannot distinguish between these different magnetic models, see e.g. our results in 2-leg ladder cuprates [37]. Other techniques can provide information on the R-symmetry breaking. The broken fourfold R-symmetry is very often associated with the existence of electronic nematicity, which was reported using magnetic torque measurements in both cuprates [18, 19] and iridates [59]. In the monolayer $HgBa_2CuO_{4+\delta}$ compound, the torque magnetometry reports an anisotropy, $\chi_{ab} \neq 0$, along the diagonals of the CuO_2 plane [19], consistent with a distortion induced by the original LC-Θ_{II} state [61]. In monolayer iridates, torque experiments also show an electronic nematicity [59] with a nematic director, which is rotated by 45° from that of monolayer cuprate $HgBa_2CuO_{4+\delta}$. This implies different LC patterns between both systems, suggesting orbital-current configurations also turned by 45° (Figure 2b) [38, 69].

In the bilayer $YBa_2Cu_3O_{6+x}$ compound, there is a weak orthorhombicity ($a \neq b$) and an electronic nematicity was reported through Nernst effect measurements [56], showing the spontaneous appearance of a strong ab anisotropy. In addition, the torque magnetometry shows an anisotropy along the principal directions, with $\chi_{aa} > \chi_{bb}$ [18] i.e. turned by 45° from the single layer compound. Actually, the surprising difference in torque measurement results in monolayer $HgBa_2CuO_{4+\delta}$ and bilayer $YBa_2Cu_3O_{6+x}$ compounds can be solved by a close examination of the way LC-Θ_{II} patterns are stacked within a bilayer (along the **c**-axis) as shown by previous PND results [14]. Indeed, using a twin-free sample of the orthorhombic $YBa_2Cu_3O_{6.6}$, our PND results show a distinct ab anisotropy of the IUC magnetic structure factor [14], as a result of R-symmetry breaking. This highlights that the IUC order in this material breaks the mirror symmetry of the CuO_2 bilayer (Figure 5b). For a single CuO_2 plaquette, 4 LC patterns are allowed and, then, 4×4 LC patterns for a bilayer. Only 4 of them produce the magnetic structure factor matching the observed ab anisotropy found in PND measurements. They correspond to a crisscrossed arrangement of the LC patterns in the bilayer, yielding a resulting anapole, $\Omega_1 + \Omega_2$, parallel to **b** axis [14] as shown in Figure 5b. Note that each of the 4 selected LC patterns could be fully identified when using both their anapole and their chiral parameter, $\mathbf{c}(\Omega_1 \wedge \Omega_2)$.

From this result and using the corrugation of the CuO_2 plane (usually called dimpling in the literature), corresponding to the fact that Cu and O atoms lay in slightly different (but parallel) planes, one can construct a picture to explain the origin of the torque anisotropy (Figure 6a–d). Assuming that LCs run exactly within the Cu–O triangle, the dimpling of the CuO_2 layer induces a tilt of the out-of-plane moment, yielding a weak ferromagnetic in-plane component **M**, pointing perpendicular to the anapole Ω_i in each layer. As the total bilayer anapole is found to be along the **b** direction, the remaining weak ferromagnetic component for the bilayer is found also along **b** (Figure 6d). Accordingly, the magnetic torque τ, defined as $\tau \propto \mathbf{M} \wedge \mathbf{H}$ for an applied magnetic field **H** along **c**, is then expected to give an anisotropy along the **a** direction as it is reported in [18]. This simple picture gives a nice agreement between the microscopic picture deduced from PND experiment and the macroscopic torque measurements. It should be stressed that the weak ferromagnetic component would be averaged owing to the existence of the four domains of the LC-Θ_{II} state [64, 65].

Electronic nematicity was reported in the bilayer $Bi_2Sr_2CaCu_2O_{8+\delta}$ family as well, using either STM images of the IUC states [7,8,70,71] or electronic Raman scattering in the B_{1g} symmetry [72]. As in the bilayer $YBa_2Cu_3O_{6+x}$ material, a nematic director is found along the Cu–O bonds. Therefore, the nematic state in $Bi_2Sr_2CaCu_2O_{8+\delta}$ can be understood the same way assuming a similar crisscrossed arrangement of LCs within the CuO_2 bilayer, i.e. with a total anapole moment in the bilayer pointing along the Cu–O bonds. Alternatively, the LC-Θ_{II} state is a $\mathbf{q} = 0$ electronic state that could co-exist with other orthogonal $\mathbf{q} = 0$ electronic states, such as an electronic nematic state [73].

To conclude, the proposed LC-Θ_{II} represents the most adequate starting point to describe the IUC magnetism observed in PND experiments. It takes into account the various constraints imposed by symmetry even though additional features need to be considered.

4. Loop currents for cuprates

4.1. *Pseudogap line in cuprates: a phase transition*

Describing the generic experimental phase diagram shown in Figure 1, one realizes that the IUC order occurs at T^*, the PG onset temperature. The PG energy scale impacts a large number of experimental spectroscopic probes in cuprates, for instance electronic Raman scattering [74]. For a long time, the PG physics in 2D cuprates has been considered as a crossover phenomenon observed in various physical properties, occurring over a certain range of temperatures. No

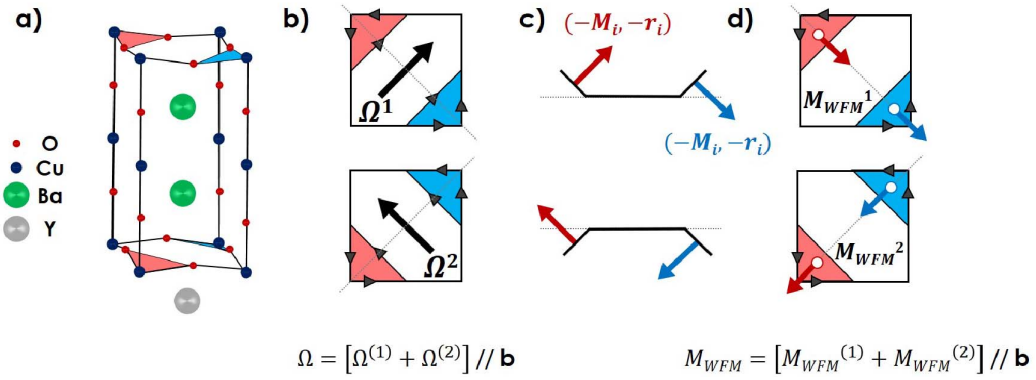

Figure 6. (a) Crystal structure of $YBa_2Cu_3O_{6+x}$, showing the corrugation or dimpling of the CuO_2 planes. (b) Top view of the loop currents arrangements of the LC-Θ_{II}-type in each CuO_2 layer (from [14]) where the toroidal moment is shown in black. The summed toroidal moment for a bilayer is pointing along the **b** direction. (c) Cut of the unit cell along the diagonal showing the orbital moments perpendicular to the O–Cu–O triangle. The dimpling of the O–Cu–O triangle gives rise to an horizontal magnetic component along the diagonal direction. (d) Top view of the summed magnetic moment, also pointing along **b**.

sharp anomaly was seen in the specific heat data, from which it was concluded that T^*, where the PG opens in transport measurements, cannot correspond to a thermodynamic phase transition [5]. In the recent years, as pointed out above, various symmetry breakings were identified over a much thinner range of temperatures. Independent measurements of an order parameter breaking T-, P- and R-symmetries agree on the location of a phase transition seen in experiments probing the thermodynamic properties. This is clearly established in three high-T_c superconducting cuprate families (the monolayer $HgBa_2CuO_{4+\delta}$, the bilayers $YBa_2Cu_3O_{6+x}$ and $Bi_2Sr_2CaCu_2O_{8+\delta}$). Figure 7 shows exclusively experimental results in $Bi_2Sr_2CaCu_2O_{8+\delta}$. That system is important to adress the issue of the PG because surface spectroscopic techniques can be performed as that material cleaves easily. Numerous ARPES [75] and tunneling spectroscopy of junctions [76, 77] studies have been performed to establish the depletion of the electronic states in that particular cuprate family. These estimates agree with T^* deduced from resistivity measurements [78] as well with those obtained from various spectroscopies [79, 80]. The IUC magnetism observed using PND was among the first reported order parameters in the PG state, which starts at a temperature T_{mag} that matches T^* (see Figures 1 and 7) and agrees with the downturn of the resistivity measurements in $YBa_2Cu_3O_{6+x}$ [6], in $HgBa_2CuO_{4+\delta}$ [15, 17] and in $Bi_2Sr_2CaCu_2O_{8+\delta}$ [78]. That suggested that the PG line corresponds to a true phase transition. Later, detailed analysis of the magnetization measurements [81], resonant ultrasound spectroscopy [22] and torque measurements [18, 19] demonstrated in both $YBa_2Cu_3O_{6+x}$ and $HgBa_2CuO_{4+\delta}$ that the PG line is truly a thermodynamic phase transition.

Although the reported features at T^* are rather weak in amplitude, they are all observed due to the higher accuracy of those techniques compared with specific heat data, where a large phonon background has to be removed. This establishes that the PG state is necessarily associated with an ordered state, a point that should be present in any model relevant for the physics of high-T_c cuprates. For instance, it is argued [82] that these results are compatible with the thermodynamics of the Ashkin–Teller model, which corresponds to the universality class of the LC-ordered phase, as this model does not produce any strong jump in the specific heat for a wide range of parameters [83].

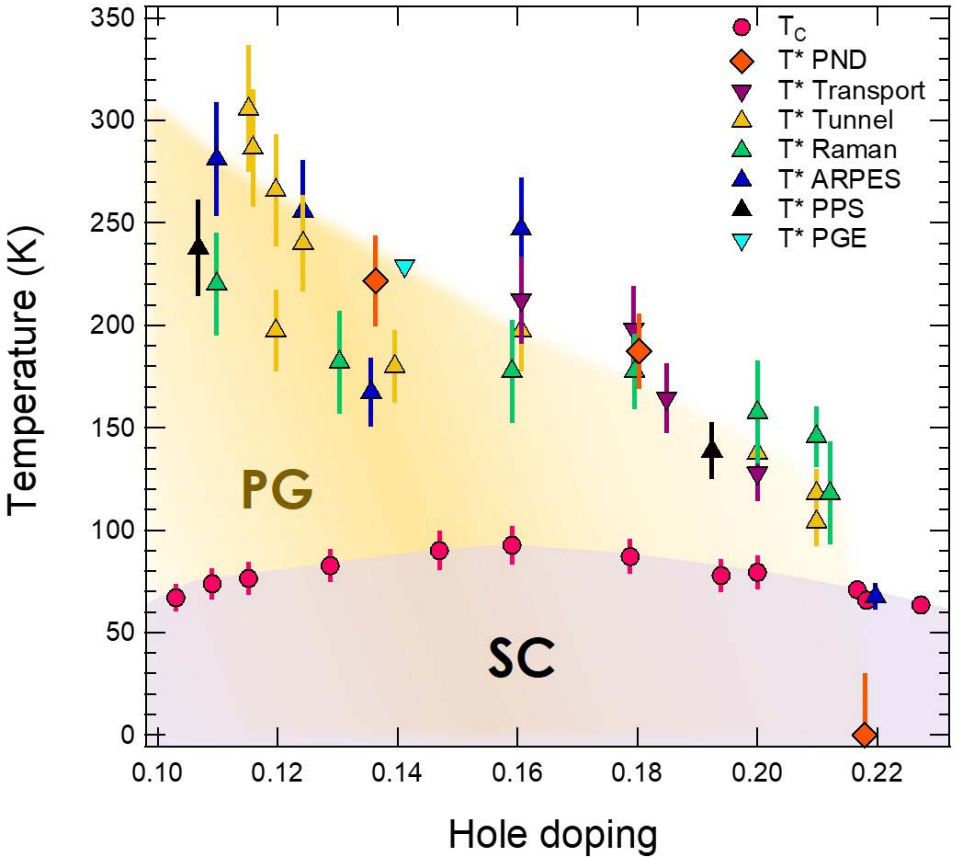

Figure 7. High-T_c superconducting cuprates phase diagram versus hole concentration for the cuprate family $Bi_2Sr_2CaCu_2O_{8+\delta}$ showing the intra-unit cell (IUC) magnetic order associated with the pseudogap state from polarized neutron diffraction (PND) [34, 35], transport [78], tunnel [76, 77], electronic Raman scattering [80], ARPES [75], pump probe spectroscopy (PPS) [79] and photo-galvanic (PGE) [60] experiments. Representative area for superconductivity (SC) and pseudogap (PG) are also depicted.

It has to be stressed that no other true symmetry-breaking phase than the IUC magnetism develops long range 3D correlation at T^*. Contrariwise, the incipient CDW phase develops at lower temperature (Figure 1), deep inside the PG state [2, 3] and remains short range and quasi-2D at zero magnetic field. That contrasts with the cases where uniform perturbations, such as a strong external magnetic field [84] or a uni-axial strain [85], are applied, which promote a long range ordered CDW, at the expense of superconductivity. If uniform perturbations can be used to tune the balance between superconductivity and CDW inside the PG state, the substitution by a minute amount of non magnetic (Zn) impurity on Cu site is sufficient to lower strongly the onset temperature of both states [86]. In contrast, the PG state [87] and the onset temperature of IUC magnetism [12] are both extremely robust against non magnetic impurity substitution. Furthermore, the IUC magnetism is reduced in amplitude through Zn substitution [12], in agreement with a picture established by NMR and STM [88] that the PG physics basically vanishes near Zn impurities, while remaining unchanged a few lattice spacings away from the impurity.

4.2. *Loop currents and pseudogap*

Because of its central play in the generic phase diagram, it is compulsory to consider PG physics in any scenario aiming at a description of the physics of cuprates. Being intimately tied to the PG state, the IUC magnetism, reported by PND, has to be implemented in any theoretical approach. Although the interplay between the LCs and the PG state is rather obvious from experimental results, its theoretical importance remains unclear as the proposed LC order in cuprates cannot open a PG at the Fermi level simply because it preserves LT symmetry [2]. Indeed, $\mathbf{q} = 0$ electronic instabilities in the electron–hole channel commonly split or distort the Fermi surface. This is the case for a ferromagnetic state, where two Fermi surfaces with different spin polarizations form in order to break the T-symmetry, or for an electronic nematic state where the Fermi Surface is distorted to break the R-symmetry. The only way to open a gap is then to break the LT-symmetry. Note, that superconductivity, which gaps the Fermi surface, is also a $\mathbf{q} = 0$ electronic instability, but in the electron–electron channel and it breaks a gauge symmetry. Therefore, one is left with two possibilities that we discuss below: (i) there is a hidden modulation of the IUC magnetism probed by PND, (ii) or the PG state is a distinct state of matter, intertwined with the IUC magnetism.

A modified version of the LC state, now breaking LT-symmetry, was recently proposed [28]. It consists of a LC super-cell of the four degenerate LC domains. Importantly, the next-nearest domain of a given domain should be characterized by an anapole rotated by $\pi/2$, either turned left or right, whereas the domain with an anapole rotated by π is only joining the first domain through its corners. The domains size, counted in number of unit cells P, ranges from a few cells to dozens of them. Examples of such phases are depicted in Figure 2d for $P = 1$ and in Figure 2e for $P = 2$. It is shown that domains of $P \sim$ 10–20 unit cells give rise to both a PG and Fermi arcs [28], as experimentally evidenced by ARPES and STM over the last two decades [2]. In this approach, the new magnetic unit cell is square, $(2P \times 2P)$ larger than the CuO_2 unit cell, and it is characterized by the planar wave vectors $\mathbf{q}_{\mathrm{LC}} = (1/2P, 0)$ and $(0, 1/2P)$. In a diffraction experiment like PND or resonant X-ray diffraction, this has major consequences, as the translation symmetry is now broken. Although this super-cell LC state has not been observed experimentally yet, it cannot be excluded from the current PND data sets if P is large enough. Indeed, in this case, the diffraction pattern has no maximum at the $(1, 0, L)$ or $(0, 1, L)$ Bragg reflections anymore, but gives rise to satellite reflections at $\pm\mathbf{q}_{\mathrm{LC}}$ away from them. If P were large enough, the diffracted peaks would occur as centered at the Bragg positions owing to the broad neutron instrument resolution, and to the limitations of the experiments with respect to the finite neutron polarization [43, 45, 47]. Furthermore, if there were a distribution of domains size P [89], it would lead to an effective broadening of the magnetic peaks appearing on the shoulders of the structural Bragg peaks.

The initial uniform LC phase can be as well considered as ancillary to a mother state associated with the PG state. For instance, square lattice spin liquid states are predicted to possess spontaneous LCs [38, 69]. In the framework of a fractionalized spin density wave, the LCs also appear, forming an ancillary order, resulting from the intertwining between a topological order and the discrete Z_2 broken symmetries. In spin liquids, the emergence of LC orders in the archetype of doped 1D spin-liquids (hole-doped spin ladders) has been proposed [54]. Our recent results in spin-ladders [37] shows that local discrete symmetries are also broken in 1D spin liquid systems, as it has been theoretically predicted. In other models, based on a PDW state [39, 40] or a fractionalized PDW instability [41], the PG is described as a highly fluctuating state, where a preemptive phase breaking both T- and P-symmetries (a LC-like phase) is expected at higher temperature. More generally, discrete symmetry breaking usually happens at higher temperature than continuous symmetry breaking. A strong influence of the LCs state on both unidirectional and bidirec-

tional d-wave charge-density-wave/pair-density-wave (CDW/PDW) composite orders has been emphasized [29, 90]. In these approaches, whatever the theoretical framework, the IUC LC order has to be intertwined with other states of matter [91]. For instance in Ref. [41], one starts with two primary states reported at lower temperature deep in the PG state (namely, the incipient CDW and superconductivity, both carrying a d-wave symmetry). The PG state is proposed to be a composite multi-component order parameter, where the system fluctuates between the two primary states which are intertwined. Then, the LC state would emerge as a preemptive state, born out of a higher order combination of the composite order parameters, which can be observed in the PG state (as soon as it forms), whenever the primary states still fluctuate or become static on cooling down.

Another interesting question is the relationship of the IUC magnetism with other $\mathbf{q} = 0$ electronic instabilities. In addition to the electronic nematicity observed through the Nernst effect in $YBa_2Cu_3O_{6+x}$ effect at T^* [56], enhanced electronic nematic fluctuations were observed close to the end point of the PG state at large hole doping [72]. However, they deviate from a canonical quantum critical scenario and cannot be directly associated with the PG state. Finally, the electronic nematicity could be inherited from another instability as suggested, for instance, by the sub-linear thermal dependence of torque measurements [18, 19]. This other instability could actually correspond to the LC state. Alternatively, it could be a vestigial order [92] related to the CDW, which exhibits a d-wave structure factor, implying that the electronic density on the O sites is involved [71]. At low temperature, the CDW breaks both the LT symmetry and the fourfold R-symmetry. At high temperature, when the CDW correlation length becomes shorter than the pitch of the modulation, the LT symmetry is restored and, the electronic nematic correlation only is left inside the unit cell. Both states can be viewed as the nematic (R-broken symmetry) and smectic (LT-broken symmetry) phases of an electronic liquid crystal. The role of IUC magnetism in this last approach remains unclear.

4.3. *IUC time-scale*

An important aspect of the IUC magnetic order seen in PND is that the local magnetic probes like nuclear magnetic resonance (NMR) and muon-spin rotation (μSR) are basically silent [43] because detecting the corresponding magnetic fields with magnetic resonance techniques has proved to be vastly unsuccessful, see e.g. in $HgBa_2CuO_{4+\delta}$ [93]. Another attempt using NMR in an ortho-II $YBa_2Cu_3O_{6+x}$ sample concluded that any static field at $T = 60$ K cannot be larger than ∼0.3 G at apical O site and ∼4 G at the planar O(2) sites [94]. For a static IUC magnetic order, a magnetic field of one order of magnitude larger is expected on these sites. The fact that the existence of a static long range IUC magnetism cannot be validated by NMR is a serious issue, which may question the outcome of the PND measurements. One possibility to reconcile NMR and PND data is to consider internal fluctuating fields at a timescale slow enough to appear static at the timescale of PND scattering (∼0.1 ns) but too fast to impact the NMR lines (≥10 μs).

The situation with μSR is more subtle. Since the first discovery of IUC magnetism with PND, it has been envisaged [6, 89, 95] that the magnetic moments could still fluctuate at the μSR timescale, meaning slowly enough to appear static to neutrons, but too fast to be observed as a magnetic order in μSR, therefore even more so for NMR, which probes even slower timescales. Several controversial results were reported by one team [95–97] but as a matter of fact, this interesting picture has been experimentally approved, as slow magnetic fluctuations were discovered using a longitudinal field μSR technique in $YBa_2Cu_3O_{6+x}$ compounds [21, 98] and in iridates [99].

In several $YBa_2Cu_3O_{6+x}$ underdoped samples [21, 98], at 80 K just above the superconducting temperature, the μSR measurements report magnetic correlations at a finite timescale of ∼10 ns

which fluctuate slowly enough to give rise to resolution-limited magnetic peaks in a PND experiment. Furthermore, this time-scale does not appear to be strongly temperature dependent. Such a finite time-scale associated with finite spatial domains was proposed to happen if defects limit the magnetic correlation length [89]. Short range correlations with finite in-plane correlation lengths, $\xi \sim 20a$, were actually detected in nearly optimally doped $YBa_2Cu_3O_{6+x}$ using PND [13]. As discussed above, shorter in-plane IUC correlation lengths are even observed in other cuprates, limited either by the competition with charge stripes in $(La,Sr)_2CuO_4$ [33] or by dimension in two-leg spin ladder compounds [37]. Clearly, dimension, disorder and proliferation of magnetic domains associated with degenerate LC states all can play a role.

The magnetic correlations seen by μSR can therefore be associated with slowly fluctuating magnetic domains. Interestingly, these fluctuations are maximum at the same temperature $T_{\rm mag} \sim T^*$ at which the neutron magnetic signal sets in [21, 98]. This suggests a critical slowing down of these magnetic fluctuations at T^*, associated with the PG onset. Such dynamical fluctuations at T^* have also been detected by PND in nearly optimally doped $YBa_2Cu_3O_{6+x}$ [13] and in $HgBa_2CuO_{4+\delta}$ at two hole doping levels [17].

4.4. *Possible roles of loop currents*

As it does not affect the LT symmetry, the original LC states are usually not considered as a key player for the physics of high-T_c superconducting cuprates. It is typically much less discussed than CDW, stripes physics or AF fluctuations [2, 3]. This might be for two main reasons. First, it is a more exotic phenomenon with, so far, a limited number of realizations in nature. The recent observation of P- [20], T- [36] and R- [59] symmetry breaking in $(Sr,Rh)_2IrO_4$ iridates clearly opens new frontiers as it basically corresponds to a LCs picture [25, 69]. Second, it is a state which involves not only copper orbitals but also oxygen orbitals. This orbitals mixing with an electronic phase gradiant among the three d and p orbitals is a central feature, which imposes a three-band Hubbard model as a starting point [25, 27, 38]. A large majority of the models built for cuprates usually neglects the possible role of oxygen orbitals, as the band structure is nicely reproduced by a single renormalized band electronic structure observed in ARPES and STM [2].

Numerical calculations using different methods still give contrasted pictures, even for three-band Hubbard model. On the one hand, variational Monte Carlo calculations on asymptotically large lattices and exact diagonalization on a 24-site cluster show a stabilization of the LC-Θ_{II} for a wide range of parameters [27]. On the other hand, no instance of spontaneous LCs has been found by applying cluster dynamical mean field theory in ladder cuprates [100] in materials where they have been observed [37]. As a matter of fact, variational Monte Carlo is a method to determine ground states at zero temperature, in contrast to the dynamical mean field theory, which is typically more efficient at finite temperature.

Generally speaking, LCs could be of great fundamental interest for several reasons. First, their fluctuations could be involved in the pairing mechanism and thus explain high-temperature superconductivity [64]. Within that scenario, the electrons are paired through the coupling of their local angular momentum to an operator defined as the generator of the rotations in the space of the four degenerate states discussed above. The corresponding pairing vertex favors d-wave superconductivity and is also proportional to the LC order susceptibility. Along similar lines, a novel spin-fluctuation-driven charge loop current mechanism based on the functional renormalization group theory has been proposed [101]. The discussed mechanism leads to ferro-LC order in a simple frustrated chain Hubbard model, which indicates that the LC can be universal in strongly correlated electron metals near magnetic criticality with geometrical frustration.

In the normal state, the related density susceptibility takes the functional form hypothesized for the Marginal Fermi liquid or strange metals [4]. Namely, it should be rather independent of momentum and with almost structure-less energy dependence. Such a charge response has been recently measured in cuprates using a new technique probing the charge-charge correlation function [102]. It is argued that it corresponds to the density susceptibility expected for the LC fluctuations in the normal state [4]. Interestingly, LC states are thought to be an emergent phenomenon, important for the establishment of the strange metals physics [103]. More specifically, if a scaling ω/T of the low energy dependence of the conductivity is observed, it must be due to the fluctuations of an order parameter which is a vector that breaks T and P symmetries and has zero crystal momentum [103]. That is a precisely the statement for LC order.

LC orders could also be of particular importance in certain theories of the PG state in cuprates in relation with topological orders [38] or emanating from the fluctuations of a vectorial order parameter [41, 104] as discussed above.

5. Conclusions and perspectives

In this brief overview, arguments were listed in favor of the physics of LCs in quantum materials. Numerous experiments that include PND point towards the existence of an exotic LC order parameter that does not break the LT symmetry. At a microscopic level, this corresponds to an electronic state phasing d orbitals of the transition metals with the ligand p orbitals. To some extent, the observed phenomenon could also be described by the ordering of magnetic quadrupoles of the transition metals [48, 50]. All these order parameters, anapoles, quadrupoles or orbital currents curls have in common the breaking of both T- and P-symmetries and the conservation of their product. These objects have dual (magnetic and electric) character order parameter, leading to interesting new applications for magneto-electricity [105]. For instance, they are proposed for potential applications in the field of data storage, where it would be possible to control magnetization via the application of an electric field, and thus use these toroidal domains as magnetic qubit [63].

In this context, future developments will aim at exploring and generalizing the observation of these new exotic objects in a wider range of materials. That will follow several directions: for instance, the Fe-based superconducting materials could host as well such a phase. It is actually proposed that the spin–orbit coupling present in the pnictides enforces the emergence of orbital loop current order inside the usual stripe-type spin-density wave state [106]. In any case, the investigation of LCs in other families of cuprate compounds using PND, namely in CuO, $Sr_2CuO_2Cl_2$ and $La_{2-x}Ba_xCuO_4$ should be pursued. In CuO, LCs were reported by a resonant X-ray scattering study [107], though this interpretation is not necessarily supported by later experiments and simulations [62, 108]. In $Sr_2CuO_2Cl_2$, a recent optical SHG experiment points towards a magneto-chiral state [109]. Following previous PND results [33], studying $La_{2-x}Ba_xCuO_4$ will allow one to probe the competition between the IUC magnetic order and other electronic instabilities, in that particular case the long range ordering of charge stripes [110]. All these examples should address the important question of the coexistence of LC phases with AF order in highly hole doped cuprates.

Another route to explore the magnetism related to the anapoles or quadrupoles is to use resonant X-ray diffraction at the appropriate atomic edge [49, 62, 107, 108]. Unlike usual non-resonant X-ray diffraction, the magnetic signal is enhanced at the resonant energy threshold of atomic electronic transitions. This technique, sensitive to both T- and P-symmetries, allows the separation of the magnetic signal from the atomic signal, by the use of linear or circular polarization analysis of the scattered beam. It allows one to selectively probe dipole, quadrupole transitions or the interaction between these two processes. A key advantage is the ability to select

the ion whose electronic transitions are induced by proper selection of the incident X-ray energy. For cuprates, measurements need to be carried at the absorption K-edge of Cu in order to access the terms corresponding to the anapoles, as derived from the multipolar expansion series. The IUC magnetic ordering observed in PND should induce an additional contribution to the anomal structure factor. For example, at the Cu K-edge (8985 eV), a dipolar–quadrupolar interference term (E1-E2) should occur with a characteristic dependence as a function of the azimuthal angle. This experiment certainly represents an important challenge.

Finally, the LC story has not been completed yet. The exact interplay between LC states and high-T_c superconductivity needs more experimental results, which will contribute to consolidate the theoretical models and to complete them. We hope our discovery will open up a new field of study when addressing the physical properties of highly correlated electron materials.

Glossary

AF	Antiferromagnetic/antiferromagnetism
ARPES	Angle resolved photoemission
CDW	Charge density wave
IUC	Intra-unit-cell
LC	Loop current
LT	Lattice translation
μSR	Muon spectroscopy/muon-spin rotation
NMR	Nuclear magnetic resonance
P	Parity
PDW	Pair density wave
PG	Pseudogap
PND	Polarized neutron scattering
R	Rotational
SHG	Second harmonic generation
STM	Scanning tunneling microscopy
T	Time

Acknowledgements

The authors are deeply indebted to C. M. Varma who first proposed to search for a loop currents phase in high-T_c cuprates and has been suggesting appealing novel ideas ever since. We acknowledge also the many students and colleagues who contributed to this work either in France, V. Balédent, S. de Almeida, B. Fauqué, Jaehong Jeong, L. Mangin-Thro, S. Pailhès or within our international collaborations, M. Greven, Yuan Li and all our collaborators whose names appear in Refs. [6, 11–17, 33–37]. We wish to thank F. Damay, A. Georges, T. Giamarchi, S. Lovesey, C. Pépin, E. Tailleur, A. Shekhter and J. Villain for stimulating discussions on various aspects related to this work. We acknowledge financial supports from the project NirvAna (Contract ANR-14-OHRI-0010) of the Agence National de la Recherche (ANR) French agency.

References

[1] P. W. Anderson, "More is different", *Science* **177** (1972), p. 393-396.

[2] B. Keimer, S. A. Kivelson, M. R. Norman, S. Uchida, J. Zaanen, "From quantum matter to high-temperature superconductivity in copper oxides", *Nature* **518** (2015), p. 179-186.

[3] C. Proust, L. Taillefer, "The remarkable underlying ground states of cuprate superconductors", *Annu. Rev. Condens. Matter Phys.* **10** (2019), no. 1, p. 409-429.

[4] C. M. Varma, "Colloquium: linear in temperature resistivity and associated mysteries including high temperature superconductivity", *Rev. Mod. Phys.* **92** (2020), article no. 031001.

[5] J. Loram, J. Luo, J. Cooper, W. Liang, J. Tallon, "Evidence on the pseudogap and condensate from the electronic specific heat", *J. Phys. Chem. Solids* **62** (2001), no. 1, p. 59-64.

[6] B. Fauqué, Y. Sidis, V. Hinkov, S. Pailhès, C. T. Lin, X. Chaud, P. Bourges, "Magnetic order in the pseudogap phase of high-T_C superconductors", *Phys. Rev. Lett.* **96** (2006), article no. 197001.

[7] K. Fujita, C. K. Kim, I. Lee, J. Lee, M. H. Hamidian, I. A. Firmo, S. Mukhopadhyay, H. Eisaki, S. Uchida, M. J. Lawler, E.-A. Kim, J. C. Davis, "Simultaneous transitions in cuprate momentum-space topology and electronic symmetry breaking", *Science* **344** (2014), no. 6184, p. 612-616.

[8] K. Fujita, M. H. Hamidian, S. D. Edkins, C. K. Kim, Y. Kohsaka, M. Azuma, M. Takano, H. Takagi, H. Eisaki, S.-i. Uchida, A. Allais, M. J. Lawler, E.-A. Kim, S. Sachdev, J. C. S. Davis, "Direct phase-sensitive identification of a d-form factor density wave in underdoped cuprates", *Proc. Natl Acad. Sci. USA* **111** (2014), no. 30, p. E3026-E3032.

[9] F. C. Zhang, T. M. Rice, "Effective Hamiltonian for the superconducting Cu oxides", *Phys. Rev. B* **37** (1988), p. 3759-3761.

[10] A. S. Moskvin, "Pseudogap phase in cuprates: oxygen orbital moments instead of circulating currents", *JETP Lett.* **96** (2012), p. 385-390.

[11] H. A. Mook, Y. Sidis, B. Fauqué, V. Balédent, P. Bourges, "Observation of magnetic order in a superconducting $YBa_2Cu_3O_{6.6}$ single crystal using polarized neutron scattering", *Phys. Rev. B* **78** (2008), article no. 020506.

[12] V. Balédent, D. Haug, Y. Sidis, V. Hinkov, C. T. Lin, P. Bourges, "Evidence for competing magnetic instabilities in underdoped $YBa_2Cu_3O_{6+x}$", *Phys. Rev. B* **83** (2011), article no. 104504.

[13] L. Mangin-Thro, Y. Sidis, A. Wildes, P. Bourges, "Intra-unit-cell magnetic correlations near optimal doping in $YBa_2Cu_3O_{6.85}$", *Nat. Commun.* **6** (2015), article no. 7705.

[14] L. Mangin-Thro, Y. Li, Y. Sidis, P. Bourges, "$a-b$ anisotropy of the intra-unit-cell magnetic order in $YBa_2Cu_3O_{6.6}$", *Phys. Rev. Lett.* **118** (2017), article no. 097003.

[15] Y. Li, V. Balédent, N. Barisic, Y. Cho, B. Fauqué, Y. Sidis, G. Yu, X. Zhao, P. Bourges, M. Greven, "Unusual magnetic order in the pseudogap region of the superconductor $HgBa_2CuO_{4+\delta}$", *Nature* **455** (2008), no. 7211, p. 372-375.

[16] Y. Li, V. Balédent, N. Barišić, Y. C. Cho, Y. Sidis, G. Yu, X. Zhao, P. Bourges, M. Greven, "Magnetic order in the pseudogap phase of $HgBa_2CuO_{4+\delta}$ studied by spin-polarized neutron diffraction", *Phys. Rev. B* **84** (2011), article no. 224508.

[17] Y. Tang, L. Mangin-Thro, A. Wildes, M. K. Chan, C. J. Dorow, J. Jeong, Y. Sidis, M. Greven, P. Bourges, "Orientation of the intra-unit-cell magnetic moment in the high-T_c superconductor $HgBa_2CuO_{4+\delta}$", *Phys. Rev. B* **98** (2018), article no. 214418.

[18] Y. Sato, S. Kasahara, H. Murayama, Y. Kasahara, E.-G. Moon, T. Nishizaki, T. Loew, J. Porras, B. Keimer, T. Shibauchi, Y. Matsuda, "Thermodynamic evidence for a nematic phase transition at the onset of the pseudogap in $YBa_2Cu_3O_y$", *Nat. Phys.* **13** (2017), p. 1074-1078.

[19] H. Murayama, Y. Sato, R. Kurihara, S. Kasahara, Y. Mizukami, Y. Kasahara, H. Uchiyama, A. Yamamoto, E.-G. Moon, J. Cai, J. Freyermuth, M. Greven, T. Shibauchi, Y. Matsuda, "Diagonal nematicity in the pseudogap phase of $HgBa_2CuO_{4+\delta}$", *Nat. Commun.* **10** (2019), article no. 3282.

[20] L. Zhao, D. H. Torchinsky, H. Chu, V. Ivanov, R. Lifshitz, R. Flint, T. Qi, G. Cao, D. Hsieh, "Evidence of an odd-parity hidden order in a spin–orbit coupled correlated iridate", *Nat. Phys.* **12** (2016), p. 32-36.

[21] J. Zhang, Z. Ding, C. Tan, K. Huang, O. O. Bernal, P.-C. Ho, G. D. Morris, A. D. Hillier, P. K. Biswas, S. P. Cottrell, H. Xiang, X. Yao, D. E. MacLaughlin, L. Shu, "Discovery of slow magnetic fluctuations and critical slowing down in the pseudogap phase of $YBa_2Cu_3O_y$", *Sci. Adv.* **4** (2018), no. 1, article no. eaao5235.

[22] A. Shekhter, B. J. Ramshaw, R. Liang, W. N. Hardy, D. A. Bonn, F. F. Balakirev, R. D. McDonald, J. B. Betts, S. C. Riggs, A. Migliori, "Bounding the pseudogap with a line of phase transitions in $YBa_2Cu_3O_{6+x}$", *Nature* **498** (2013), p. 75-77.

[23] C. M. Varma, "Non-Fermi-liquid states and pairing instability of a general model of copper oxide metals", *Phys. Rev. B* **55** (1997), p. 14554-14580.

[24] M. E. Simon, C. M. Varma, "Detection and implications of a time-reversal breaking state in underdoped cuprates", *Phys. Rev. Lett.* **89** (2002), article no. 247003.

[25] C. M. Varma, "Theory of the pseudogap state of the cuprates", *Phys. Rev. B* **73** (2006), article no. 155113.

[26] C. Weber, A. Läuchli, F. Mila, T. Giamarchi, "Orbital currents in extended hubbard models of high-T_c cuprate superconductors", *Phys. Rev. Lett.* **102** (2009), article no. 017005.

[27] C. Weber, T. Giamarchi, C. M. Varma, "Phase diagram of a three-orbital model for high-T_c cuprate superconductors", *Phys. Rev. Lett.* **112** (2014), article no. 117001.

[28] C. M. Varma, "Pseudogap and Fermi arcs in underdoped cuprates", *Phys. Rev. B* **99** (2019), article no. 224516.

[29] Y. Wang, A. Chubukov, "Charge-density-wave order with momentum (2Q,0) and (0,2Q) within the spin-fermion model: continuous and discrete symmetry breaking, preemptive composite order, and relation to pseudogap in hole-doped cuprates", *Phys. Rev. B* **90** (2014), article no. 035149.

[30] T. C. Hsu, J. B. Marston, I. Affleck, "Two observable features of the staggered-flux phase at nonzero doping", *Phys. Rev. B* **43** (1991), p. 2866-2877.

[31] S. Chakravarty, R. B. Laughlin, D. K. Morr, C. Nayak, "Hidden order in the cuprates", *Phys. Rev. B* **63** (2001), article no. 094503.

[32] A. Kaminski, S. Rosenkranz, H. M. Fretwell, J. Campuzano, Z. Li, H. Raffy, W. G. Cullen, H. You, C. G. Olson, C. M. Varma, H. Höchst, "Spontaneous breaking of time-reversal symmetry in the pseudogap state of a high-T_c superconductor", *Nature* **416** (2002), p. 610-613.

[33] V. Balédent, B. Fauqué, Y. Sidis, N. B. Christensen, S. Pailhès, K. Conder, E. Pomjakushina, J. Mesot, P. Bourges, "Two-dimensional orbital-like magnetic order in the high-temperature $La_{2-x}Sr_xCuO_4$ superconductor", *Phys. Rev. Lett.* **105** (2010), article no. 027004.

[34] S. De Almeida-Didry, Y. Sidis, V. Balédent, F. Giovannelli, I. Monot-Laffez, P. Bourges, "Evidence for intra-unit-cell magnetic order in $Bi_2Sr_2CaCu_2O_{8+\delta}$", *Phys. Rev. B* **86** (2012), article no. 020504.

[35] L. Mangin-Thro, Y. Sidis, P. Bourges, S. De Almeida-Didry, F. Giovannelli, I. Laffez-Monot, "Characterization of the intra-unit-cell magnetic order in $Bi_2Sr_2CaCu_2O_{8+\delta}$", *Phys. Rev. B* **89** (2014), article no. 094523.

[36] J. Jeong, Y. Sidis, A. Louat, V. Brouet, P. Bourges, "Time-reversal symmetry breaking hidden order in $Sr_2(Ir,Rh)O_4$", *Nat. Commun.* **8** (2017), article no. 15119.

[37] D. Bounoua, L. Mangin-Thro, J. Jeong, R. Saint-Martin, L. Pinsard-Gaudart, Y. Sidis, P. Bourges, "Loop currents in two-leg ladder cuprates", *Commun. Phys.* **3** (2020), no. 1, article no. 123.

[38] M. S. Scheurer, S. Sachdev, "Orbital currents in insulating and doped antiferromagnets", *Phys. Rev. B* **98** (2018), article no. 235126.

[39] D. F. Agterberg, D. S. Melchert, M. K. Kashyap, "Emergent loop current order from pair density wave superconductivity", *Phys. Rev. B* **91** (2015), article no. 054502.

[40] Z. Dai, Y.-H. Zhang, T. Senthil, P. A. Lee, "Pair-density waves, charge-density waves, and vortices in high-T_c cuprates", *Phys. Rev. B* **97** (2018), article no. 174511.

[41] S. Sarkar, D. Chakraborty, C. Pépin, "Incipient loop-current order in the underdoped cuprate superconductors", *Phys. Rev. B* **100** (2019), article no. 214519.

[42] Y. Sidis, B. Fauqué, V. Aji, P. Bourges, "Search for the existence of circulating currents in high-T_c superconductors using the polarized neutron scattering technique", *Phys. B: Condens. Matt.* **397** (2007), no. 1, p. 1-6.

[43] P. Bourges, Y. Sidis, "Novel magnetic order in the pseudogap state of high-T_c copper oxides superconductors", *C. R. Phys.* **12** (2011), no. 5, p. 461-479, Superconductivity of strongly correlated systems.

[44] Y. Sidis, P. Bourges, "Evidence for intra-unit-cell magnetic order in the pseudo-gap state of high-T_c cuprates", *J. Phys.: Conf. Ser.* **449** (2013), article no. 012012.

[45] P. Bourges, D. Bounoua, J. Jeong, L. Mangin-Thro, Y. Sidis, "Evidence for intra-unit cell magnetism in superconducting cuprates: a technical assessment", *J. Phys.: Conf. Ser.* **1316** (2019), article no. 012003.

[46] T. P. Croft, E. Blackburn, J. Kulda, R. Liang, D. A. Bonn, W. N. Hardy, S. M. Hayden, "No evidence for orbital loop currents in charge-ordered $YBa_2Cu_3O_{6+x}$ from polarized neutron diffraction", *Phys. Rev. B* **96** (2017), article no. 214504.

[47] P. Bourges, Y. Sidis, L. Mangin-Thro, "Comment on "No evidence for orbital loop currents in charge-ordered $YBa_2Cu_3O_{6+x}$ from polarized neutron diffraction"", *Phys. Rev. B* **98** (2018), article no. 016501.

[48] S. W. Lovesey, D. D. Khalyavin, U. Staub, "Ferro-type order of magneto-electric quadrupoles as an order-parameter for the pseudo-gap phase of a cuprate superconductor", *J. Phys.: Condens. Matt.* **27** (2015), no. 29, article no. 292201.

[49] S. W. Lovesey, D. D. Khalyavin, "Ordered state of magnetic charge in the pseudo-gap phase of a cuprate superconductor ($HgBa_2CuO_{4+\delta}$)", *J. Phys.: Condens. Matt.* **27** (2015), no. 49, article no. 495601.

[50] M. Fechner, M. J. A. Fierz, F. Thöle, U. Staub, N. A. Spaldin, "Quasistatic magnetoelectric multipoles as order parameter for pseudogap phase in cuprate superconductors", *Phys. Rev. B* **93** (2016), article no. 174419.

[51] B. Hennion, "La diffusion inélastique des neutrons sur monocristal. Le spectromètre 3-axes", *JDN* **10** (2010), p. 357-378.

[52] Y. Ishikawa, K. Tajima, D. Bloch, M. Roth, "Helical spin structure in manganese silicide MnSi", *Solid State Commun.* **19** (1976), no. 6, p. 525-528.

[53] M.-H. Julien, "Magnetic order and superconductivity in $La_{2-x}Sr_xCuO_4$: a review", *Phys. B: Condens. Matt.* **329–333** (2003), p. 693-696, Proceedings of the 23rd International Conference on Low Temperature Physics.

[54] P. Chudzinski, M. Gabay, T. Giamarchi, "Orbital current patterns in doped two-leg Cu–O Hubbard ladders", *Phys. Rev. B* **78** (2008), article no. 075124.

[55] J. Xia, E. Schemm, G. Deutscher, S. A. Kivelson, D. A. Bonn, W. N. Hardy, R. Liang, W. Siemons, G. Koster, M. M. Fejer, A. Kapitulnik, "Polar Kerr-effect measurements of the high-temperature $YBa_2Cu_3O_{6+x}$ superconductor: evidence for broken symmetry near the pseudogap temperature", *Phys. Rev. Lett.* **100** (2008), article no. 127002.

[56] R. Daou, J. Chang, D. LeBoeuf, O. Cyr-Choinière, F. Laliberté, N. Doiron-Leyraud, B. J. Ramshaw, R. Liang, D. A. Bonn, W. N. Hardy, L. Taillefer, "Broken rotational symmetry in the pseudogap phase of a high-T_c superconductor", *Nature* **463** (2010), p. 519-522.

[57] Y. Lubashevsky, L. Pan, T. Kirzhner, G. Koren, N. P. Armitage, "Optical birefringence and dichroism of cuprate superconductors in the THz regime", *Phys. Rev. Lett.* **112** (2014), article no. 147001.

[58] L. Zhao, C. A. Belvin, R. Liang, D. A. Bonn, W. N. Hardy, N. P. Armitage, D. Hsieh, "A global inversion-symmetry-broken phase inside the pseudogap region of $YBa_2Cu_3O_y$", *Nat. Phys.* **13** (2017), p. 250-254.

[59] H. Murayama, K. Ishida, R. Kurihara, T. Ono, Y. Sato, Y. Kasahara, H. Watanabe, Y. Yanase, G. Cao, Y. Mizukami, T. Shibauchi, Y. Matsuda, S. Kasahara, "Bond directional anapole order in a spin-orbit coupled Mott insulator $Sr_2(Ir_{1-x}Rh_x)O_4$", *Phys. Rev. X* **11** (2021), article no. 011021.

[60] S. Lim, C. M. Varma, H. Eisaki, A. Kapitulnik, "Observation of broken inversion and chiral symmetries in the pseudogap phase in single and double layer bismuth-based cuprates", https://arxiv.org/abs/2011.06755, 2020.

[61] A. Shekhter, C. M. Varma, "Considerations on the symmetry of loop order in cuprates", *Phys. Rev. B* **80** (2009), article no. 214501.

[62] S. Di Matteo, M. R. Norman, "Orbital currents, anapoles, and magnetic quadrupoles in CuO", *Phys. Rev. B* **85** (2012), article no. 235143.

[63] N. A. Spaldin, M. Fiebig, M. Mostovoy, "The toroidal moment in condensed-matter physics and its relation to the magnetoelectric effect", *J. Phys.: Condens. Matt.* **20** (2008), no. 43, article no. 434203.

[64] V. Aji, A. Shekhter, C. M. Varma, "Theory of the coupling of quantum-critical fluctuations to fermions and d-wave superconductivity in cuprates", *Phys. Rev. B* **81** (2010), article no. 064515.

[65] Y. He, C. M. Varma, "Theory of polarized neutron scattering in the loop-ordered phase of cuprates", *Phys. Rev. B* **86** (2012), article no. 035124.

[66] J. Orenstein, "Optical nonreciprocity in magnetic structures related to high-T_c superconductors", *Phys. Rev. Lett.* **107** (2011), article no. 067002.

[67] V. M. Yakovenko, "Tilted loop currents in cuprate superconductors", *Phys. B: Condens. Matt.* **460** (2015), p. 159-164, Special Issue on Electronic Crystals (ECRYS-2014).

[68] S. Lederer, S. A. Kivelson, "Observable NMR signal from circulating current order in YBCO", *Phys. Rev. B* **85** (2012), article no. 155130.

[69] S. Chatterjee, S. Sachdev, "Insulators and metals with topological order and discrete symmetry breaking", *Phys. Rev. B* **95** (2017), article no. 205133.

[70] M. J. Lawler, K. Fujita, J. Lee, A. R. Schmidt, Y. Kohsaka, C. K. Kim, H. Eisaki, S. Uchida, J. C. Davis, J. P. Sethna, E.-A. Kim, "Intra-unit-cell electronic nematicity of the high-T_c copper-oxide pseudogap states", *Nature* **466** (2010), p. 347-351.

[71] S. Mukhopadhyay, R. Sharma, C. K. Kim, S. D. Edkins, M. H. Hamidian, H. Eisaki, S.-i. Uchida, E.-A. Kim, M. J. Lawler, A. P. Mackenzie, J. C. S. Davis, K. Fujita, "Evidence for a vestigial nematic state in the cuprate pseudogap phase", *Proc. Natl Acad. Sci. USA* **116** (2019), no. 27, p. 13249-13254.

[72] N. Auvray, B. Loret, S. Benhabib, M. Cazayous, R. D. Zhong, J. Schneeloch, G. D. Gu, A. Forget, D. Colson, I. Paul, A. Sacuto, Y. Gallais, "Nematic fluctuations in the cuprate superconductor $Bi_2Sr_2CaCu_2O_{8+\delta}$", *Nat. Commun.* **10** (2019), article no. 5209.

[73] M. H. Fischer, E.-A. Kim, "Mean-field analysis of intra-unit-cell order in the Emery model of the CuO_2 plane", *Phys. Rev. B* **84** (2011), article no. 144502.

[74] A. Sacuto, S. Benhabib, Y. Gallais, S. Blanc, M. Cazayous, M.-A. Méasson, J. S. Wen, Z. J. Xu, G. D. Gu, "Pseudogap in cuprates by electronic Raman scattering", *J. Phys.: Conf. Ser.* **449** (2013), article no. 012011.

[75] I. M. Vishik, M. Hashimoto, R.-H. He, W.-S. Lee, F. Schmitt, D. Lu, R. G. Moore, C. Zhang, W. Meevasana, T. Sasagawa, S. Uchida, K. Fujita, S. Ishida, M. Ishikado, Y. Yoshida, H. Eisaki, Z. Hussain, T. P. Devereaux, Z.-X. Shen, "Phase competition in trisected superconducting dome", *Proc. Natl Acad. Sci. USA* **109** (2012), no. 45, p. 18332-18337.

[76] R. Dipasupil, M. Oda, N. Momono, M. Ido, "Energy gap evolution in the tunneling spectra of $Bi_2Sr_2CaCu_2O_{8+\delta}$", *J. Phys. Soc. Japan* **71** (2002), no. 6, p. 1535-1540.

[77] L. Ozyuzer, J. F. Zasadzinski, K. E. Gray, C. Kendziora, N. Miyakawa, "Absence of pseudogap in heavily overdoped $Bi_2Sr_2CaCu_2O_{8+\delta}$ from tunneling spectroscopy of break junctions", *Europhys. Lett.* **58** (2002), no. 4, p. 89-595.

[78] T. Watanabe, T. Fujii, A. Matsuda, "Anisotropic resistivities of precisely oxygen controlled single-crystal $Bi_2Sr_2CaCu_2O_{8+\delta}$: systematic study on "Spin Gap" effect", *Phys. Rev. Lett.* **79** (1997), p. 2113-2116.

[79] Y. Toda, F. Kawanokami, T. Kurosawa, M. Oda, I. Madan, T. Mertelj, V. V. Kabanov, D. Mihailovic, "Rotational symmetry breaking in $Bi_2Sr_2CaCu_2O_{8+\delta}$ probed by polarized femtosecond spectroscopy", *Phys. Rev. B* **90** (2014), article no. 094513.

[80] B. Loret, N. Auvray, G. D. Gu, A. Forget, D. Colson, M. Cazayous, Y. Gallais, I. Paul, M. Civelli, A. Sacuto, "Universal relationship between the energy scales of the pseudogap phase, the superconducting state, and the charge-density-wave order in copper oxide superconductors", *Phys. Rev. B* **101** (2020), article no. 214520.

[81] B. Leridon, P. Monod, D. Colson, A. Forget, "Thermodynamic signature of a phase transition in the pseudogap phase of $YBa_2Cu_3O_x$ high-T_C superconductor", *Europhys. Lett.* **87** (2009), no. 1, article no. 17011.

[82] C. Varma, L. Zhu, "Specific heat and sound velocity at the relevant competing phase of high-temperature superconductors", *Proc. Natl Acad. Sci. USA* **112** (2015), p. 6331-6335.

[83] M. S. Grønsleth, T. B. Nilssen, E. K. Dahl, E. B. Stiansen, C. M. Varma, A. Sudbø, "Thermodynamic properties near the onset of loop-current order in high-T_c superconducting cuprates", *Phys. Rev. B* **79** (2009), article no. 094506.

[84] D. LeBoeuf, S. Kramer, W. N. Hardy, R. Liang, D. A. Bonn, C. Proust, "Thermodynamic phase diagram of static charge order in underdoped $YBa_2Cu_3O_y$", *Nat. Phys.* **9** (2013), p. 79-83.

[85] H.-H. Kim, S. M. Souliou, M. E. Barber, E. Lefrançois, M. Minola, M. Tortora, R. Heid, N. Nandi, R. A. Borzi, G. Garbarino, A. Bosak, J. Porras, T. Loew, M. König, P. J. W. Moll, A. P. Mackenzie, B. Keimer, C. W. Hicks, M. Le Tacon, "Uniaxial pressure control of competing orders in a high-temperature superconductor", *Science* **362** (2018), no. 6418, p. 1040-1044.

[86] S. Blanco-Canosa, A. Frano, T. Loew, Y. Lu, J. Porras, G. Ghiringhelli, M. Minola, C. Mazzoli, L. Braicovich, E. Schierle, E. Weschke, M. Le Tacon, B. Keimer, "Momentum-dependent charge correlations in $YBa_2Cu_3O_{6+\delta}$ superconductors probed by resonant X-ray scattering: evidence for three competing phases", *Phys. Rev. Lett.* **110** (2013), article no. 187001.

[87] H. Alloul, P. Mendels, H. Casalta, J. F. Marucco, J. Arabski, "Correlations between magnetic and superconducting properties of Zn-substituted $YBa_2Cu_3O_{6+x}$", *Phys. Rev. Lett.* **67** (1991), p. 3140-3143.

[88] H. Alloul, J. Bobroff, M. Gabay, P. J. Hirschfeld, "Defects in correlated metals and superconductors", *Rev. Mod. Phys.* **81** (2009), p. 45-108.

[89] C. M. Varma, "Pseudogap in cuprates in the loop-current ordered state", *J. Phys.: Condens. Matt.* **26** (2014), no. 50, article no. 505701.

[90] V. S. de Carvalho, C. Pépin, H. Freire, "Coexistence of Θ_{II}-loop-current order with checkerboard d-wave CDW/PDW order in a hot-spot model for cuprate superconductors", *Phys. Rev. B* **93** (2016), article no. 115144.

[91] R.-G. Cai, L. Li, Y.-Q. Wang, J. Zaanen, "Intertwined order and holography: the case of parity breaking pair density waves", *Phys. Rev. Lett.* **119** (2017), article no. 181601.

[92] E. Fradkin, S. A. Kivelson, J. M. Tranquada, "Colloquium: theory of intertwined orders in high temperature superconductors", *Rev. Mod. Phys.* **87** (2015), p. 457-482.

[93] A. M. Mounce, S. Oh, J. A. Lee, W. P. Halperin, A. P. Reyes, P. L. Kuhns, M. K. Chan, C. Dorow, L. Ji, D. Xia, X. Zhao, M. Greven, "Absence of static loop-current magnetism at the apical oxygen site in $HgBa_2CuO_{4+\delta}$ from NMR", *Phys. Rev. Lett.* **111** (2013), article no. 187003.

[94] T. Wu, H. Mayaffre, S. KrÀÂd'mer, M. Horvatic, C. Berthier, W. Hardy, R. Liang, D. Bonn, M.-H. Julien, "Incipient charge order observed by NMR in the normal state of $YBa_2Cu_3O_y$", *Nat. Commun.* **6** (2015), article no. 6438.

[95] A. Pal, K. Akintola, M. Potma, M. Ishikado, H. Eisaki, W. N. Hardy, D. A. Bonn, R. Liang, J. E. Sonier, "Investigation of potential fluctuating intra-unit cell magnetic order in cuprates by μSR", *Phys. Rev. B* **94** (2016), article no. 134514.

[96] A. Pal, S. R. Dunsiger, K. Akintola, A. C. Y. Fang, A. Elhosary, M. Ishikado, H. Eisaki, J. E. Sonier, "Quasistatic internal magnetic field detected in the pseudogap phase of $Bi_{2+x}Sr_{2-x}CaCu_2O_{8+\delta}$ by muon spin relaxation", *Phys. Rev. B* **97** (2018), article no. 060502.

[97] S. Gheidi, K. Akintola, A. C. Y. Fang, S. Sundar, A. M. Côté, S. R. Dunsiger, G. D. Gu, J. E. Sonier, "Absence of μSR evidence for magnetic order in the pseudogap phase of $Bi_{2+x}r_{2-x}CaCu_2O_{8+\delta}$", *Phys. Rev. B* **101** (2020), article no. 184511.

[98] Z. H. Zhu, J. Zhang, Z. F. Ding, C. Tan, C. S. Chen, Q. Wu, Y. X. Yang, O. O. Bernal, P.-C. Ho, G. D. Morris, A. Koda, A. D. Hillier, S. P. Cottrell, P. J. Baker, P. K. Biswas, J. Qian, X. Yao, D. E. MacLaughlin, L. Shu, "Muon spin relaxation and fluctuating magnetism in the pseudogap phase of $YBa_2Cu_3O_y$", *Phys. Rev. B* **103** (2021), article no. 134426.

[99] C. Tan, Z. F. Ding, J. Zhang, Z. H. Zhu, O. O. Bernal, P. C. Ho, A. D. Hillier, A. Koda, H. Luetkens, G. D. Morris, D. E. MacLaughlin, L. Shu, "Slow magnetic fluctuations and critical slowing down in $Sr_2Ir_{1-x}Rh_xO_4$", *Phys. Rev. B* **101** (2020), article no. 195108.

[100] X. Lu, D. Sénéchal, "Loop currents in ladder cuprates: a dynamical mean field theory study", *Phys. Rev. B* **102** (2020), article no. 085135.

[101] R. Tazai, Y. Yamakawa, H. Kontani, "Emergence of charge loop current in the geometrically frustrated Hubbard model: a functional renormalization group study", *Phys. Rev. B* **103** (2021), article no. L161112.

[102] M. Mitrano, A. A. Husain, S. Vig, A. Kogar, M. S. Rak, S. I. Rubeck, J. Schmalian, B. Uchoa, J. Schneeloch, R. Zhong, G. D. Gu, P. Abbamonte, "Anomalous density fluctuations in a strange metal", *Proc. Natl Acad. Sci. USA* **115** (2018), no. 21, p. 5392-5396.

[103] D. V. Else, T. Senthil, "Strange metals as ersatz Fermi liquids", https://arxiv.org/abs/2010.10523, 2020.

[104] C. Morice, D. Chakraborty, X. Montiel, C. Pépin, "Pseudo-spin skyrmions in the phase diagram of cuprate superconductors", *J. Phys.: Condens. Matt.* **30** (2018), no. 29, article no. 295601.

[105] M. Fiebig, "Revival of the magnetoelectric effect", *J. Phys. D: Appl. Phys.* **38** (2005), no. 8, p. R123-R152.

[106] M. Klug, J. Kang, R. M. Fernandes, J. Schmalian, "Orbital loop currents in iron-based superconductors", *Phys. Rev. B* **97** (2018), article no. 155130.

[107] V. Scagnoli, U. Staub, Y. Bodenthin, R. A. de Souza, M. García-Fernández, M. Garganourakis, A. T. Boothroyd, D. Prabhakaran, S. W. Lovesey, "Observation of orbital currents in CuO", *Science* **332** (2011), no. 6030, p. 696-698.

[108] Y. Joly, S. P. Collins, S. Grenier, H. C. N. Tolentino, M. De Santis, "Birefringence and polarization rotation in resonant X-ray diffraction", *Phys. Rev. B* **86** (2012), article no. 220101.

[109] A. de la Torre, K. L. Seyler, L. Zhao, S. Di Matteo, M. S. Scheurer, B. Yu, L. Y, M. Greven, S. Sachdev, M. R. Norman, D. Hsieh, "Mirror symmetry breaking in a model insulating cuprate", *Nat. Phys.* **17** (2021), p. 777-781.

[110] M. Hücker, M. v. Zimmermann, G. D. Gu, Z. J. Xu, J. S. Wen, G. Xu, H. J. Kang, A. Zheludev, J. M. Tranquada, "Stripe order in superconducting $La_{2-x}Ba_xCuO_4$ ($0.095 \leq x \leq 0.155$)", *Phys. Rev. B* **83** (2011), article no. 104506.

Comptes Rendus
Physique
2021, 22, nº S5, p. 33-50
https://doi.org/10.5802/crphys.96

Prizes of the French Academy of Sciences 2020 / *Prix 2020 de l'Académie des sciences*

Relation between mechanical response of reinforced elastomers and dynamics of confined polymer chains

Relation entre la réponse mécanique des élastomères renforcés et la dynamique des chaînes polymères confinées

Helene Montes [a] **and Francois Lequeux** [*, a]

[a] Sciences et Ingénierie de la Matière Molle, UMR 7615, ESPCI Paris, Université PSL, CNRS, Sorbonne Université, 75005 Paris, France

E-mails: helene.montes@espci.fr (H. Montes), francois.lequeux@espci.fr (F. Lequeux)

Dedicated to the memory of Aurélie Papon, our brightest student, who unfortunately left us too soon.

Abstract. Elastomers used in everyday life are always reinforced with rigid nanoparticles (carbon black or silica). The addition of rigid nanoparticles to an elastomer gives it very specific viscoelastic properties. In this article, we discuss the current understanding of mechanical properties of a polymer matrix around its glass transition, focusing on the situation of polymers confined between two rigid surfaces with a nanometric gap. Then, we will explain how the properties of the matrix can help to understand the properties of filled or reinforced elastomers. We will then explain that in reinforced rubbers, the mechanical properties are dominated by stress propagation between neighboring aggregates through a nanometric polymer gap, thus by confined polymer bridges. We will discuss how knowledge of the dynamics of confined polymers allows us to understand the temperature dependence, the pressure dependence and the non-linearities observed for strain below 0.1 of reinforced elastomers.

Résumé. Les élastomères utilisés dans la vie courante sont toujours renforcés avec des nanoparticules rigides (noir de carbone, ou silice). L'ajout de nanoparticules rigides dans un élastomère leur confère des propriétés mécaniques très spécifiques. Dans cet article, nous rappelons d'abord ce que l'on connait aujourd'hui des propriétés mécaniques d'un élastomère autour de sa transition vitreuse, et en particulier lorsqu'il est confiné entre deux surfaces solides proche de quelques nanomètres. Puis nous expliquerons comment ces propriétés peuvent aider à la compréhension de celles des élastomères renforcés. En effet nous montrons que dans les élastomères renforcés, les propriétés mécaniques sont dominées par la propagation de la contrainte entre nanoparticules par des ponts de polymère confinés. Nous discuterons comment la connaissance de

* Corresponding author.

la dynamique des polymères confinés permet de comprendre les effets de température, de pression est les non-linéarités précoces de la mécanique des élastomères renforcés.

Keywords. Glass transition, Polymer physics, Mechanical properties, Reinforced elastomers, Confinement, Nanoparticles, Pressure.

Mots-clés. Transition vitreuse, Physique des polymères, Propriétés mécaniques, Élastomères renforcés, Confinement, Nanoparticules, Pression.

Note. Francois Lequeux is the 2020 recipient of the « Grand prix de la fondation Michelin – Académie des sciences ».

Available online 2nd May 2022

1. Introduction

Glassy polymers (glassy polystyrene, polymethylmetacrylate (PMMA), and epoxies) and semicrystalline polymers (most of the polyolefins) are generally used without reinforcing with solid fillers. However, most of elastomers—crosslinked polymer above their glass transitions, such as those used in shoe soles, car tires, gaskets, and plastic nipples, are mixed and reinforced with solid fillers. The fillers used are generally carbon black or silica nanoparticles. A representation of a typical reinforced elastomer is shown in Figure 1. It consists of solid particles (typically 100 nm in size) of various shapes that are embedded in a matrix of crosslinked polymer chains. From an industrial point of view, fillers are added to achieve the two following objectives. The first is simply that fillers are less expensive than elastomers; hence, adding fillers reduces the price of the products. The second is at the heart of this work, is that the presence of inorganic nanoparticles considerably modifies and reinforces the mechanical properties of elastomers. Their addition increases the elastic modulus and the wear resistance as well as toughness. However, at small strain amplitudes (above 0.1%), the addition of fillers causes elastic nonlinearities (strain softening) that result in a dissipation mechanism crucial for applications, such as car tires and mechanical dampers.

Understanding the microscopic origin of the mechanical properties of reinforced rubbers has been challenging for scientists. The question of why rigid nanoparticles increase the elastic modulus of the filled sample and generate a complex mechanical response remains unsolved. The first possible answer, which appeared in the material science community fifty years ago [1], is that polymer dynamics is modified by the presence of rigid nanoparticles. However, the nature and physical origin of such a modification of polymer dynamics by the fillers has remained unclear since 2000. Similarly the question of how dynamics of polymer chains precisely affect the mechanical properties of reinforced elastomers remains a challenging question that we have addressed over the past twenty years [2–4].

Payne in 1962 [5] identified that the mechanics of reinforced rubber is controlled by hard and soft zones corresponding to various dynamical states of the polymers, which have different mechanical properties. In a seminal paper on the mechanics of filled elastomers, Payne has wrote "*We may assume that the proportion of hard and soft zones is determined by the type and concentration of (carbon) black (nanoparticles), the details of processing, here exemplified by the effect of heat treatment, the temperature and, of course the immediate preceding strain history.*" However, the nature of these hard and soft zones has not beenmade clear up to now. We propose in the present study that hard and soft zones, which correspond to the zones at which polymers connect to the rigid fillers, are in glassy and rubber states, respectively. This finding was inspired by experiments that revealed the possible modification of glass transition in the vicinity of solid surfaces. The idea that the dynamical response of polymers near their glass transition is modified in the vicinity of surfaces emerged in the physics community in 1995. The study conducted

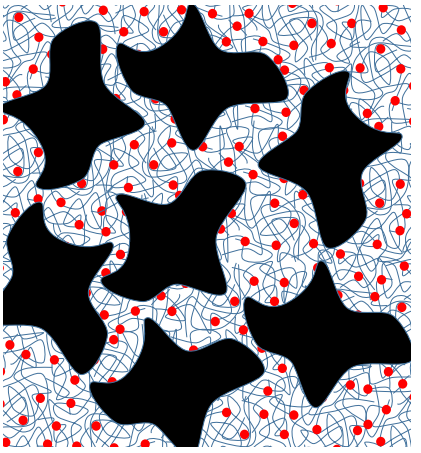

Figure 1. A schematic of a filled elastomer. Solid nanoparticles (in black) are embedded in cross-linked polymer chains (red dots). Possibly, the polymers can also be covalently connected to the particle surfaces.

by Keddie *et al.* [6] was one of the first to identify that the measured glass transition temperature of a thin layer of polymer was different from that of the bulk polymer. The effect of surface proximity on the polymer dynamics has been confirmed by several researchers and has been reported in numerous publications in the past decades [7, 8]. Thus, it has been suggested that the glass transition temperature near rigid boundaries is shifted compared to that in bulk polymers. Furthermore, Wang [9] was the first to propose that modification of the mechanical response of polymer chains near nanoparticle surfaces, which is similar to the shift of the glass transition temperature observed in thin films, can explain the mechanics of filled elastomers. However, other mechanisms have been proposed to explain some features of the mechanical behavior of filled elastomers: the possible adsorption–desorption of polymer chains under mechanical solicitations [10] and changes in polymer structure near a solid surface [11]. Both these mechanisms have a temperature dependence which is different from that of polymers near their glass transition. Lastly, other mechanisms have been proposed, such as the modification of reptation and the Rouse dynamics of polymer chains near the surface [12, 13]. We will see that the temperature dependence of the mechanical properties of filled elastomers, which follows the time–temperature law of pure polymers [14], unambiguously reveals that modification of the dynamics occurring locally in the vicinity of nanoparticle surface is the main origin of the linear and weak-nonlinear viscoelastic behavior.

In this paper, we therefore focus on the dynamical features of polymer chains near solid surfaces and their influence on the mechanical properties of filled elastomers. The objective of this paper is to summarize the effect of the modification of local polymer mechanical properties, which is induced by the presence of solid particles, on the macroscopic mechanical properties of filled elastomers.

This paper is organized as follows.

First, we briefly recall the mechanical properties of a pure elastomer matrix (without fillers) near the glass transition temperature in bulk polymers. We show that the concept of dynamical heterogeneities, which were discovered nearly 20 years ago, helps us to understand the origin of the width of the glass transition domain as well as the onset of yielding.

Second, we discuss the polymer dynamics in a confined geometry. The concept of dynamical

heterogeneities provides a physical interpretation of the mechanical properties of a polymer chain confined between two surfaces.

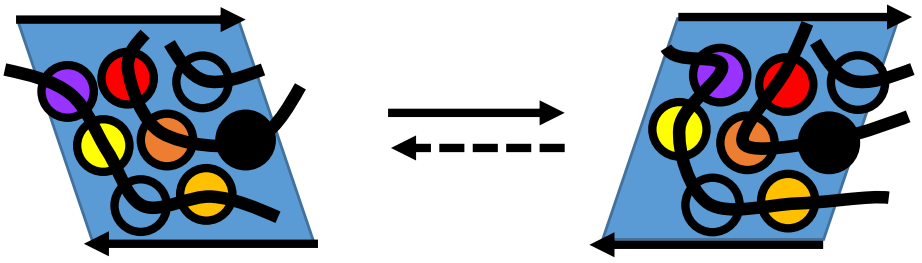

Figure 2. Schematic cage motions. Monomer (in orange) is trapped by its neighbors. The neighbors constitute the cage. Under sufficient stress (or thermal activation), the monomer escapes from the cage and the system reaches a new configuration: a new cage is formed. At a mesoscopic scale, this corresponds to a change in strain.

Third, we discuss the effect of polymer confinement on three macroscopic mechanical properties of filled elastomers, i.e., the linear viscoelasticity, variation of elasticity as a function of pressure, and nonlinear viscoelastic response observed at small amplitude known as "Payne's" effect.

2. Bulk polymer mechanics near the glass transition

First, we briefly present the physical origin of polymer mechanical response near the glass transition. We schematically distinguish two regimes: the glassy and rubber states.

(a) The glassy state corresponds to low temperatures, where the chain dynamic is very slow compared to the duration of experiments. In the glassy state, the thermal motions of the monomers are slow and, in practice, restricted to distances smaller than 0.1 nm, i.e., smaller than the monomer. A consequence of the restricted motions is that any macroscopic deformation in the linear regime results in a tiny variation in the distance between neighboring monomers. Hence, the shear modulus originates from the intramolecular forces—mostly Van der Waals interactions [15]—between monomers and is of the order of the bulk modulus, which is typically 1 GPa.

Sufficiently large stress (50 MPa) or strain (0.05) may induce however irreversible motions (typically nanometric) of monomers known in the literature as "cage motions," "plastic events," or "hops" [16, 17]. These motions correspond to a modification of the structure with a change of the nearest neighbors of a given monomer (see for instance in Figure 2, the monomer in orange which has as first neighbors, before the application of the stress, monomers in blue, red and black and after the application of shear stress, monomers in violet, red and black).

Macroscopically, the phenomenon just mentioned corresponds to yielding. The yield strain originates from the monomer packing geometry. All glassy polymers yield above a given stress of typically a few tens of MegaPascals or when the deformation exceeds about 3–5%.

(b) In the rubbery state, the monomer motions are fast, corresponding to high temperatures, i.e., $T \gg T_g$, where the monomer dynamics are very fast compared to the duration of experiments. The monomers then experience fluctuations at the scale of the chains or more precisely at the scale of the distance between crosslinks and entanglements, typically over tens of nanometers. At this length scale, each chain may exhibit many configurations. In the rubber state, under macroscopic deformation, the entropy contribution to free energy dominates. The entropy modification of chains under elongation leads to a stress opposite to deformation, as depicted in Figure 3. The shear modulus resulting from this mechanism is of the order of 1 MPa in practice. The precise origin of the elastic response of crosslinked elastomers is well known, as it originates from

Figure 3. Chains connected to the network by crosslinks may be stretched by a few hundred of % while keeping their integrity. The elongation decreases the entropy and generates a force on the crosslinks.

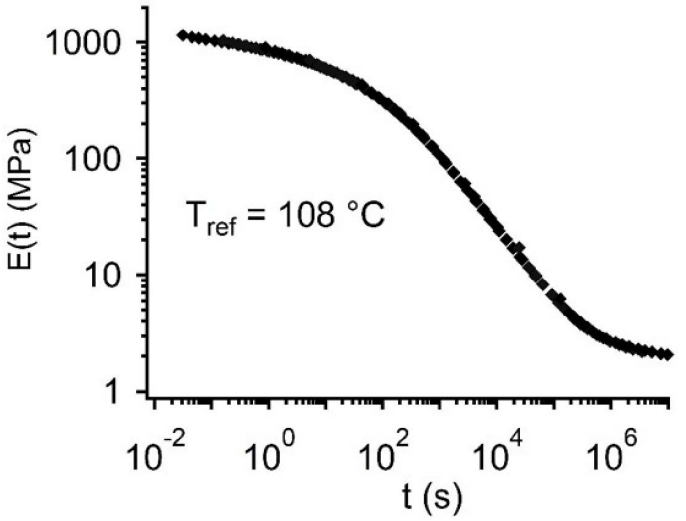

Figure 4. Relaxation modulus—or stress relaxation after a strain step divided by the step amplitude—of a crosslinked PolyMethylMethAcrylate (PMMA) matrix across the glass transition. The modulus is approximately 1 GPa before the cage hops (Van der Waals regime) and decreases progressively to approximately 1 MPa (entropic regime). Measurements were performed at a temperature of 108 °C. The WLF law was used to build the entire master curve, giving the modulus relaxation over 9 decades [16].

entropy modifications of a network under topological constraints caused by crosslinks and entanglements [18]. At a macroscopic scale, the deformation can produce reversible changes of a few tens of %.

At the crossover between the two regimes just mentioned, the monomer dynamics is of the order of the measurement time. It is governed by cage hops, which are similar to those induced by strain (Figure 2) but occurring spontaneously under the simple effect of thermal activation. The average lifetime of cages varies strikingly but continuously with temperature. By varying the temperature between the glassy and molten states, a sharp but continuous variation is observed in the elastic modulus from 1 GPa to 1 MPa at a given time scale (Figure 4). This phenomenon is called the glass transition [19]. In polymer science, the glass transition temperature T_g is usually defined as the temperature at which the average lifetime of the cages is 1 s.

Nearly all polymers exhibit a similar variation in their dynamics with temperature. This variation is in general described by the following empirical law for the mean monomer relaxation time, which is known as WLF law [14]

$$\mathrm{In}\left(\frac{\tau}{\tau_0}\right) = \frac{-C_1(T-T_g)}{C_2+T-T_g}, \tag{1}$$

where the mean monomer relaxation time τ_0 at T_g is chosen equal to 1 s. The WLF coefficients C_1 and C_2 weakly depend on the chemical nature of the polymer, with typical values of $C_1 \approx 17$ and $C_2 \approx 50$ K. The above empirical formula exhibits a divergence in the relaxation time for $T = T_g - C_2$. This divergence has been discussed in detail (see [20] for instance) and it appears not to have any physical meaning, because it cannot be reached experimentally. Indeed, measuring the relaxation time at temperatures below T_g by 10 K is very difficult because the relaxation times are very large, typically months or years.

The properties of a polymer material around its glass transition are described as viscoelastic. The viscoelastic modulus is the ratio of the stress over the strain, under a sinusoidal strain solicitation, using a complex number. For an elastic material, the stress and strain are in phase and the viscoelastic modulus is real, but it is complex for a polymer around the glass transition because of the relaxation. The viscoelastic modulus depends on both frequency and temperature. Equation (1) can be used to superimpose the frequency viscoelastic modulus at various temperature. At least in a time window of about 3 decades, over more than 50 K, the viscoelastic modulus appears to follow the time/temperature superposition law given by (1) [14]. Thus, WLF's law allows a measurement of the viscoelastic spectrum at a given frequency for various temperatures and to deduce the viscoelastic spectrum at other frequencies and temperatures, which considerably broadens the frequency window for polymer experimentation. For instance in Figure 4, the relaxation modulus is shown. The relaxation modulus is the stress relaxation of the material, as a function of the time, after a step of strain, divided by the strain test amplitude. It can be shown that it is also the Fourier transform of the frequency dependent viscoelastic modulus. Using the time rescaling of (1), the relaxation modulus spans over 10 decades of time. But it results from the superimposition of relaxation modulus measured over three decades of time over a temperature window of 50 Kelvin by applying (1).

WLF's relation gives a very good description of the temperature dependence of the characteristic relaxation time of polymers, but it does not describe the width of the glass transition at all. In the previous figure, it is implicitly assumed that all the cages have similar lifetimes, but recent measurements have shown that this is not at all the case. Near the glass transition, polymer materials exhibit "dynamical heterogeneities [10]." The term "dynamical heterogeneities" means that the lifetimes of the cages are distributed over more than 4 decades, and the correlation length of these rearrangements, i.e., the size of the cages is approximately 5 nm. These dynamical heterogeneities have been the subject of several vast studies of the glass transition, beyond polymers [21]. The mechanical consequences of these dynamical heterogeneities are considered and a step strain solicitation is applied to the crosslinked matrix in its glassy state. Each domain of the polymer matrix accumulates some stress. As time progresses, each domain will undergo a cage rearrangement that will cause a decrease in stress, as depicted in Figure 2. The stress of a given domain will relax over a time equal to the cage lifetime. Thus, the lifetime that is widely distributed leads to a non exponential slow decay of the stress relaxation. A full description of this is the following: from a mechanical point of view, a polymer can be considered as an ensemble of 5-nm domains, each with its own stress relaxation time, which is distributed over many decades over the entire material.

We have shown that these dynamical heterogeneities can be mimicked with the model shown in Figure 5. Following this model, the bulk is divided into 5-nm-wide domains, each exhibiting the following mechanical behavior: a glassy branch that corresponds to the intermolecular attraction contribution with a shear modulus of approximately 1 GPa and a specific relaxation time τ_i that mimics cage lifetime, in parallel with a 1-MPa branch that corresponds to the entropic contribution.

The distribution of lifetimes of the domains presents as a log-normal law, which reflects a Gaussian distribution of the energy barrier involved in cages hops, but it can be based on more

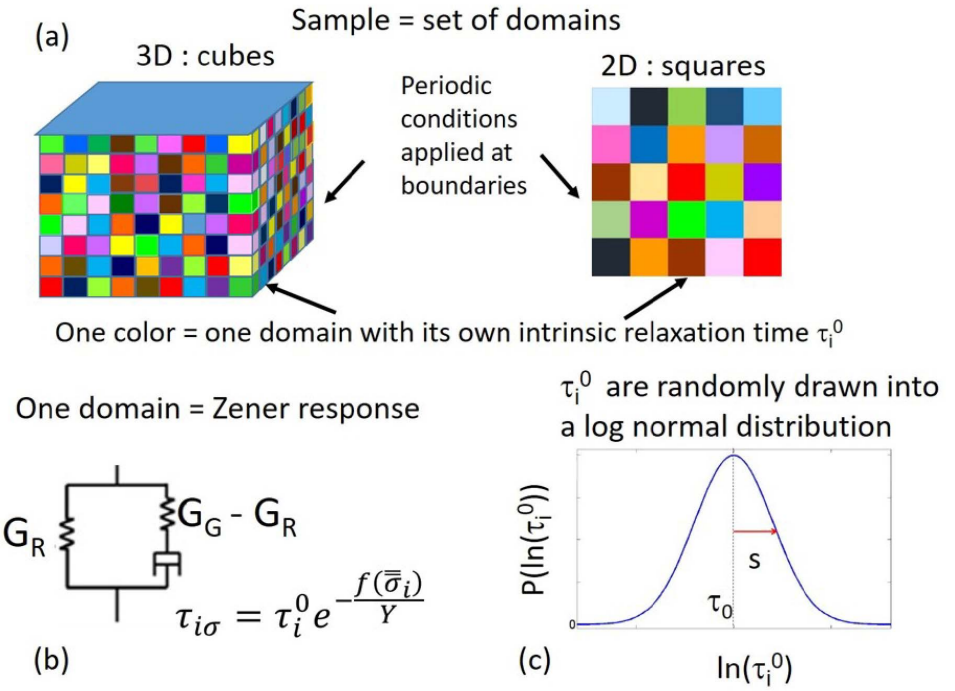

Figure 5. Mechanical simulations of polymer mechanics. Each domain possesses a rubber branch and a glassy branch in parallel. The latter is in series with a damper to have its own relaxation time. The relaxation time is drawn randomly from a log-normal distribution and may be affected by the local stress.

microscopic arguments (see Long and collaborator's work, for instance in [22, 23]). To a good approximation, we can write the lifetime distribution as follows:

$$P(\ln(\tau_i^0)) = \frac{1}{\sqrt{2\pi}s} \exp\left(-\ln\left(\frac{\tau_i^0}{\tau_0}\right) \Big/ 2s^2\right). \tag{2}$$

Where s is the width of the time distribution, and τ_0 a characteristic time. The width s depends on the polymer, but is typically around 4.5 for an homopolymer [24]. We then numerically solved the model [25], which appears to describe very precisely the viscoelastic modulus of polymer glasses in their linear regime [24], as shown in Figure 6 for two systems.

Therefore, including nonlinear mechanical properties in this model is easy. As explained in Section 2, the application of stress can induce cage rearrangements similar to that induced by thermal activation. The relaxation of domains under macroscopic stress has been measured in previous studies [26], and the results have been discussed recently by Long [27], and have been confirmed experimentally by us very recently [28]. The cage lifetime, and the time for the modulus decay from 1 GPa to 1 MPa, depends on the local stress applied. For the sake of simplicity, we write it in a scalar form in $\tau = \tau_0 e^{\sigma^2/Y^2}$, where σ is the local stress, Y is typically 10 MPa, and τ_0 is the cage lifetime in the absence of stress. This law describes how thermal hopping is modified by stress. Therefore, the mechanical properties of a polymer matrix near its glass transition can be satisfactorily described by including the local relaxation times from the previous model as follows:

$$\tau_i = \tau_i^0 e^{\sigma^2/Y^2}, \tag{3}$$

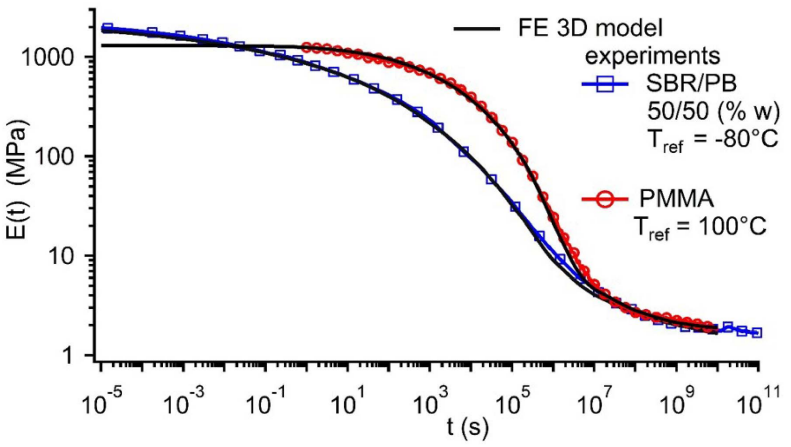

Figure 6. Relaxation modulus for crosslinked PMMA and crosslinked blends of poly butadiene. Continuous lines are results of the model presented in Figure 5. Details can be found in previous studies [13].

where the cage lifetime of domain iτ_i^0 is randomly drawn over a log-normal distribution of many decades width (2), and σ is the local stress. This type of model has been proven to very efficiently describe the polymer mechanics both in the linear (as explained in the previous sentences) and nonlinear regimes in the glass–rubber crossover regime.

Once the physical origin of the polymer viscoelastic responses near the glass transition is established, including recent findings on the so-called dynamical heterogeneities, we will now explore how mechanical behavior is modified in confined geometries.

3. Confinement effects on polymer dynamics

We will now show that the model representing a polymer bulk as a collection of dynamical heterogeneous domains can explain confinement effects and thus the shift of glass transition temperature observed in thin polymer films. For a few decades, it has been observed that the polymer dynamics should be modified at the surface of solid particles in filled elastomers. These modifications have been correlated with some mechanical properties of filled rubbers [9]. More recently, motivated by the developments of nanotechnologies, the mechanical properties of thin-polymer film coatings on solid substrates have been studied, revealing that the dynamics of polymer films may be different from the those of bulk materials [8].

The recent literature unanimously agrees that the dynamics of polymers near their glass transition is modified by the presence of hard or soft boundaries [8]. We will now consider a situation of interest for reinforced elastomers: a polymer is confined between two solid walls with a strong anchoring between the walls and polymer (see Figure 7). This situation mimics the behavior of a polymer confined between two neighboring solid particles in a filled rubber and reveals size dependent mechanical properties discussed below [29].

First, let us assume that the thickness of the layer is approximately 5 nm and that hundreds of domains constitute the polymer bridge between particles. These have random relaxation times that span many decades, as explained above. We apply a step strain to this bridge and separately consider the slowest domain compared to other domains. When all other domains have relaxed their stress, the two solid walls remain mechanically connected only by the slowest domain, which has a modulus of 1 GPa, whereas other domains exhibit a modulus of 1 MPa. Thus, the

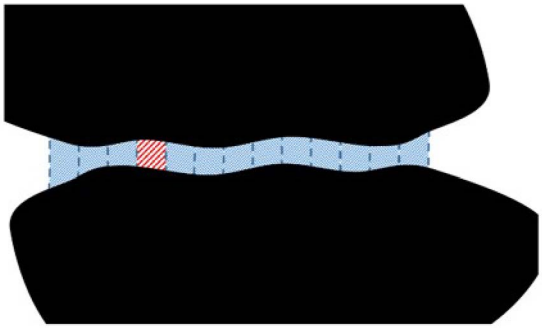

Figure 7. Polymer bridges between two particle surfaces, constituted by several domains. The slowest domains, which are 10^3 fold more rigid than the others at the end of the relaxation, controls the stress transmission.

stress is carried by the slowest domain, which provides an apparent modulus of about 10 MPa to the bridge. Therefore, the slowest domain dominates the mechanical response of the polymer connection between the walls. Thus, the rigidity of the polymer bridge is dominated by the one percent of slowest domains.

This situation is very different from the case of a bulk polymer. In that case, the slowest domains must at least form a percolation network to dominate the macroscopic mechanical response. Thus, in bulk polymers, the slowest domains that dominate the stress have to be more than in a film (typically more than 10% in bulk as compared to less than 1% in nanometric films).

Because polymer samples near T_g exhibit a large width in local relaxation times, their mechanical response will strongly depend on the geometry of the mechanical solicitation. A length over which the mechanical properties propagate may thus be introduced. This length has to be related to the dynamical heterogeneities. In a naive view, the change in mechanical transmission can be described as a shift of the glass transition temperature of polymer chains in the vicinity of a solid surface. In this frame, we show that a good approximation of the dependence of the glass transition temperature as a function of the distance z from the surface can be written as follows:

$$T_g(z) = T_g^{\infty} \cdot \left(1 + \frac{\delta}{z}\right), \tag{4}$$

where z is the distance to the surface, δ an atomic length, and T_g^{∞} the glass transition of the matrix at an infinite distance from any surfaces, or in bulk. A more complete analysis of the mechanical behavior of a polymer thin film between two solid surfaces has been performed using the aforementioned model. Figure 8 shows that the mechanical response is shifted toward lower frequencies (or higher temperatures) under confinement. Furthermore, the glass transition domain is broadened. The simulation has been satisfactorily compared to the experimental results of filled elastomers. Introducing a clear mechanical criterion for the glass transition—e.g., the temperature at which the macroscopic modulus of a confined polymer film has a given value—Equation (4) can appears to be a satisfactory approximation. Hence we see that dynamical heterogeneities—that are considered as mechanical heterogeneities—induce an apparent shift of the glass transition of polymer chains confined between solids walls.

The slowing down of polymer dynamics has been the object of various interpretations. Note that effects other than the effect just mentioned may also contribute to a slowing down of the polymer mechanical response near surfaces. First, at a monomeric scale, the modification of the structure and of the dynamics induced by the change in structure may also contribute to

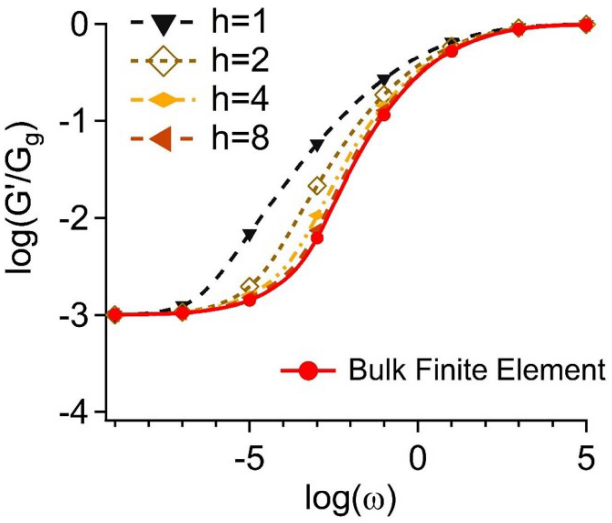

Figure 8. Real part of the apparent visco-elastic modulus of confined polymer in thin films versus frequency predicted by the aforementioned model for a film thickness h equal to 1, 2, 4 and 8 domains, as well as for the bulk finite element. The relaxation in thin films extends to lower frequencies as compared to the one in bulk polymers and broadens with increasing confinement [30].

slow the dynamics down. However, in that case, a shift in the dynamics is not expected to follow the frequency–temperature WLF's law, in contrast to what is observed subsequently [2, 3]. The shift in dynamic caused by structural modification appears more like a rigid shell around the particles [31]. Second, the mechanism of adsorption/desorption under mechanical solicitation is involved when describing modifications of the dynamics near nanoparticle surfaces [10]. There is however no reason why these mechanisms would follow the frequency–temperature WLF law, while experimental results do. Finally, the polymer chain dynamics (Rouse motions and reptation) are modified near the surfaces, but these last contributions typically induce a shift in time relaxations of a factor of two, whereas the confinement effect leads to a shift of two decades.

The effect of confinement on the mechanical response of polymers is crucial because of dynamical heterogeneities. The mechanical behavior of elastomers will indeed reveal this effect, as explained in the next section.

4. Filled elastomer mechanics

In industrial filled elastomers, the amount of nanoparticles is optimized such that the average distance between nanoparticle surfaces is of the order of a few nanometers. The adjustment of nanoparticle concentration is in fact a compromise. A small distance between nanoparticles surfaces leads to the system becoming very rigid and brittle, whereas a large distance will cause the fillers to have a negligible effect on the mechanics. In the optimal situation, from an engineering point of view, the stress in filled rubbers originates mostly in the forces transmitted between nanoparticles through a thin layer of polymer. This peculiar mode of stress transmission is described in the literature as "particles network" [32] (see Figure 9). These effects of confinement are crucial in the stress transmission within the filled elastomers because they ensure the

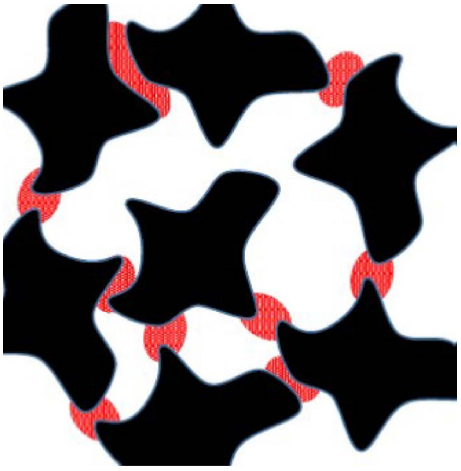

Figure 9. A schematic view of a particles network connected by polymer bridges (in red).

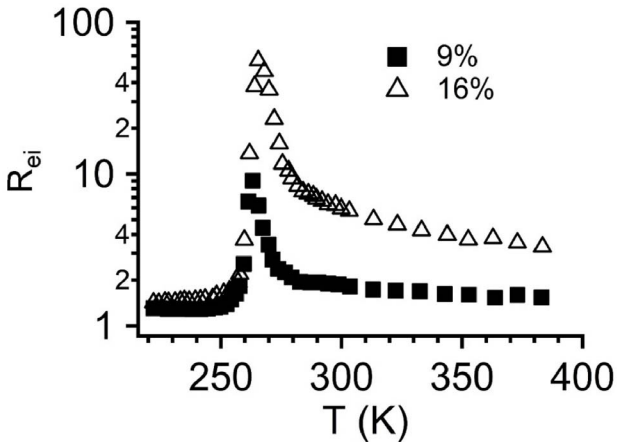

Figure 10. Ratio between the elastic modulus of filled elastomers versus the pure matrix for two spherical nanoparticle volume fractions (9% and 16%). Samples described in [2]. This ratio exhibits a maximum in the glass transition domain, and the modulus of the pure matrix simply decreases with temperature in this temperature range, as shown in Figure 4. This reveals that the filled rubbers have slower temperature decay than that of the matrix. Thus, the width of the glass transition domain of the bridges is on average larger than that of the matrix. The slow decay of R_e indicates that the glass transition domain of the bridges spans more than 100 K.

stress transmission between nanoparticles. We refer to the confined polymer between particles as "polymer bridges".

The effect of stress transmission through the particle network can be quantified by the reinforcement coefficient R_{ei}, which is equal to the ratio between the elastic modulus in the presence of nanofillers divided by the elastic modulus of the pure matrix. R_{ei} depends obviously on the nanoparticle volume fraction. Moreover, R_{ei} decreases with increasing temperature, even at a few tens of Kelvins greater than the glass transition temperature of the matrix. Precisely, R_{ei} exhibits a bell-shaped dependence on temperature, as shown in Figure 10.

This phenomenon can be understood as follows. At low temperatures, both the matrix and bridges are glassy, and the reinforcement is weak. Similarly, at high temperatures, both the matrix and bridges are in the rubber state and the reinforcement is weak. Thus, the bell-shaped curve reveals that the mechanical difference between the elastic modulus of the bridges and that of the matrix is at maximum a few tens of Kelvins above the glass transition temperature. This reveals that there is a shift between the temperature dependence of the elastic modulus of the polymer bridges and that of the matrix, which agrees with the shift in the glass transition temperature measured directly for the confined polymers (or polymer bridges), as discussed in the previous sections.

Polymer bridges can thus be glassy or not, depending on the temperature and the gap thickness. For mechanical behaviour, the distribution of distances between neighboring particle surfaces is crucial. In practice, because filled elastomers are prepared by mechanical mixing, the distance between neighboring particles, or the thickness of the glassy bridges, is distributed. It is indeed possible to vary the distribution of distance with the same amount of filler in a model, filled elastomer prepared according to a nonindustrial process [33]. We observed that a change in the bridge thickness distribution strongly modifies the shape of the temperature dependence of the modulus. Thus, bridge thickness distribution is a key parameter for the mechanical response of filled elastomers.

Simple laws can be deduced from this remark. Let us consider that each bridge has its own gap d, and its distribution we will call $p(d)$. The glass transition of the bridge, which originates from the shift in T_g induced by the two surfaces, at a distance $d/2$ of the surface that can be estimated using the following relation [15]:

$$T_g(d) = T_g^{\infty} \cdot \left(1 + 4\frac{\delta}{d}\right). \tag{5}$$

Thus, at temperature T, the bridges with a glass transition temperature $T_g(d)$ larger than T will be glassy, and the others will be rubber-like. For the most part, the bridges that really participate in the stress transmission across the sample are the glassy ones. Their fraction X is given as follows:

$$X = \int_0^{d_c} p(x)\,\mathrm{d}x, \tag{6}$$

where the upper boundary of the integral is related to the room temperature and the glass transition temperature of the matrix:

$$d_c = 4\delta \frac{T_g^{\infty}}{T - T_g^{\infty}}. \tag{7}$$

Thus, it is expected that R_{ei} depends exclusively on the fraction X. This naïve view appears to efficiently predict frequency–temperature superposition behavior. As explained above, the definition of glass transition temperature depends on the choice of a characteristic time, meaning that T_g^{∞} depends on the frequency of the measurements, which can be written as $T_g^{\infty}(\omega)$. Therefore, changing the frequency and temperature such that d_c remains constant must not modify the value of R_{ei}. This is indeed observed in our experiments [2], confirming that the shift in glass transition temperature is the most crucial factor that controls the mechanics of filled elastomers.

If the distribution p is smooth, increasing the temperature will lead to a decrease in X and may be somehow equivalent to a decrease in the filler volume fraction. As a result, in samples with "good" dispersion, a volume fraction/temperature superposition behavior is observed [3].

This qualitatively explains why different distributions (as measured with neutron scattering) lead to different temperature dependences in similar systems [33]. Furthermore, it can predict the pressure–temperature superposition law specific to filled elastomers, as explained in the next section.

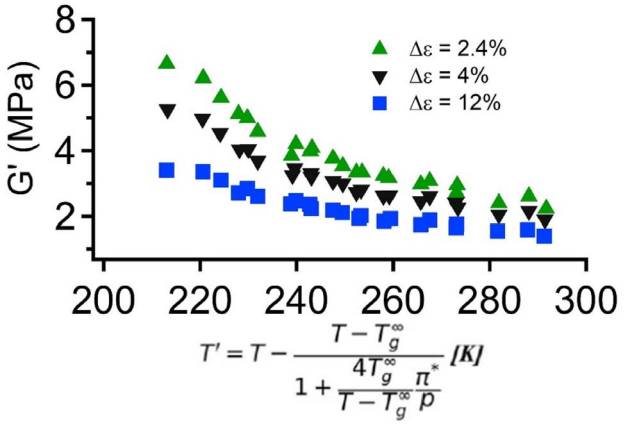

Figure 11. Temperature–pressure modulus master curves obtained for poly(dimethylsiloxane-co-diphenylsiloxane) elastomers filled with silica particles at 27% volume and applying sinusoidal strain of various amplitudes ($\Delta\varepsilon = 2.4\%$, $\Delta\varepsilon = 4\%$, and $\Delta\varepsilon = 12\%$). Master curves were obtained by taking $T_g^\infty = 158$ K and $\pi^* = 2.2$ MPa [23]. Pressure varies from 0 to 3.1 MPa.

5. Pressure effect

One of the consequences of the presence of glassy bridge connection particles is the effect of pressure on the mechanical properties of filled elastomers.

For bulk polymers, applying pressure is known to result in an increase in the glass transition temperature [14]. A basic picture is given by the free volume model. In this model, the dynamics of the chains are related to the amount of unoccupied volume, the free volume, in the system. As explained above, monomers are trapped in cages by their neighbors. There are periodic changes in density over time and space owing to thermal activation fluctuations in density. Once the density is weak enough at a given location, the cage can rearrange. According to the free volume theory, density is the key parameter that controls the polymer chain dynamics. Under pressure, density increases and thus free volume decreases, causing a slowing down of the dynamics and causing increase of the glass transition temperature. This basic image obviously has some limitations, but it is relatively correct. Experimentally, for pure elastomers, one observes typical increase in T_g of 0.5 K for a change in amplitude of the pressure is around 1 MPa.

In the case of reinforced elastomers, pressure causes an increase in the elastic modulus, which can similarly be expressed in terms of an increase in the glass transition temperature. However, the increase in amplitude of the T_g is approximately 50 K/MPa, two orders of magnitude larger than the one measured for a pure elastomer [34]. Under pressure, the density increases. This decreases the length of the glassy bridges, leading to a stronger confinement of the polymer chains in the glassy bridges. The dominant mechanism is not the variation in the free volume of the elastomer itself, but a decrease in the glassy bridge thickness. Because their rigidity considerably depends on the gap between bridges and the glassy bridges sustain most of the stress, the macroscopic modulus considerably increases under pressure.

We can easily quantify this effect. For the sake of simplicity, we assume that under pressure the sample undergoes uniform contraction. If R is the radius of the particles, the variation in distance δd between neighboring particle surfaces under pressure can be written as follows:

$$\frac{\delta d}{d + 2R} = -\frac{P}{K}, \tag{8}$$

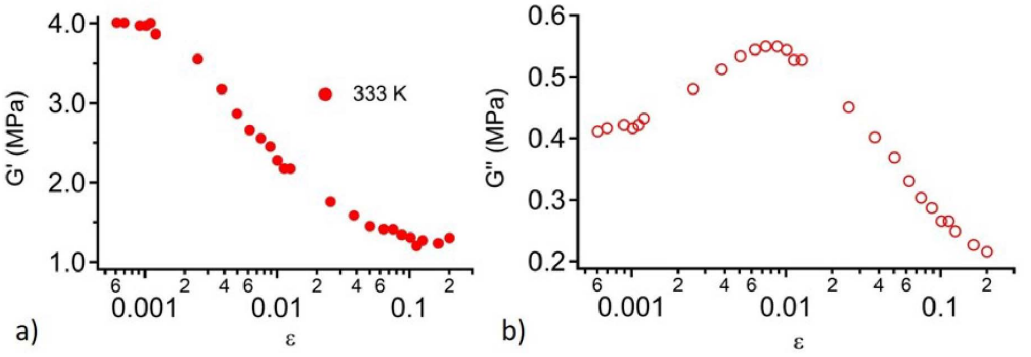

Figure 12. Typical apparent elastic and loss modulus as a function of strain amplitude ε of a poly(dimethylsiloxane-co-diphenylsiloxane) elastomer filled with silica particles at 27% volume at 333 K and 1 Hz.

where P is the applied pressure, K the compression modulus (typically 1 GPa), and V the volume of the sample. Thus, the fraction of bridges that are glassy is given by (6), but with the upper bound d_c shown as follows:

$$d_c = 4\delta \frac{T_g^\infty}{T - T_g^\infty} + \frac{P}{K} 2R, \tag{9}$$

with $R \gg d$. Under two pressure–temperature (P, T) and $(0, T_0)$ conditions, such that they lead to the same value of d_c, the same bridges will transmit the stress across the sample, and thus we expect to have the same mechanical behavior. This gives the pressure/temperature superposition law as follows:

$$T_0 = T - \frac{T - T_g^\infty}{1 + \frac{4T_g^\infty}{T - T_g^\infty} \frac{\pi^*}{P}}, \tag{10}$$

where $\pi^* = (K\delta)/(2R)$.

This is exactly what we observed experimentally in industrial samples as shown in Figure 11 [34]. Experimentally, π^* is of the order of a few MPa, which is in good agreement with the aforementioned estimation. Thus, in the mechanical modeling of filled elastomers, pressure effects should be taken into consideration as soon as the stress exceeds 1 MPa. To conclude, pressure effects reveal the strength of the glassy bridge approach.

6. Payne's effect

Compared to pure elastomers, reinforced elastomers exhibit a precocious nonlinear response [35, 36]. When submitted to oscillatory strain, the apparent elastic modulus typically begins to decrease at strain amplitudes larger than 1%, whereas the apparent loss modulus exhibits a maximum. Typical behavior of the apparent elastic and loss moduli as a function of strain amplitude is shown in Figure 12.

This is known as Payne's effect, and it is very important in industrial applications.

Payne's effect corresponds to a strong but nonlinear mechanical dissipation in filled elastomers. At the same temperature and strain amplitude, the matrix is purely elastic. In industry, because dissipation has to be controlled, particularly in car tires and filled rubber dampers, Payne's effect has been the object of numerous discussions. As a result, it is mainly described

as the progressive destruction of the particle network under increasing strain and at large amplitudes, the effect of a particle network disappears. We can quantitatively discuss the effect of strain on bridges.

Under strain, two effects may be considered: the modification of bridge thickness and strain softening of glassy bridges.

(a) As explained in the previous section devoted to pressure effect, the distance between fillers is modified by strain. For a given bridge, depending on the respective positions of the fillers, compared to strain orientation, the distance between fillers may increase or decrease. However, on average, the distance increases with strain (at the second order), resulting in a decrease in the average glass transition temperature of the bridges. We estimate the effect of strain on the shift in the glass transition temperature of the bridges. Under a strain of amplitude ε, the mean distance averaged over all directions increases by a factor of $\varepsilon^2/3$. The average bridge thickness changes under a strain of approximately $2R\varepsilon^2$. According to (4), a T_g shift of approximately $(\Delta T_g)/(T_g^\infty) \approx -(8\delta R\varepsilon^2)/(3d^2)$ is expected.

(b) The stress in the bridges decreases the relaxation times, as written in (3). Because the stress is transmitted by the glassy bridges, the stress concentrates in these glassy bridges: the local stress to consider has to be taken to be larger than the macroscopic stress by a factor equal to the particle section πR^2 divided by the bridge section, which can be estimated as πRd. Therefore, the local stress in the bridge is of the order of $((E_r R_{ei} R)/d)\epsilon$. This corresponds to a shift in cage lifetime, as given by (3), which corresponds to (1) to a shift in glass transition temperature of $(\Delta T_g)/(T_g^\infty) \approx -(C_2)/(T_g^\infty C_1)((E_r R_{ei} R)/(Yd))^2$ using (1).

After quantifying all these relations, the second effect (b) typically dominates the first effect (a) by a factor of 100. Thus, Payne's effect is expected to be controlled by the strain softening of glassy bridges. Indeed, quantifying strain softening gives a good estimate of the strain at which the decrease of the elastic modulus and the increase of dissipation begins to be significant—more than 10% for a strain of about 1% typically. Moreover, the frequency–temperature equivalence can be observed for the viscoelastic non linear response associated to Payne's effect, similar to the one observed for the linear elastic modulus. A detailed analysis of Payne's effect has been made possible by all the tools developed in the recent past on the physics of glassy polymers. However, new tools must be developed to provide a stochastic and tensorial description of the bridges to the community.

7. Conclusion

Recent advances in the physical origin of the mechanics of amorphous polymers thus provided a renewed understanding of the mechanics of filled rubbers, a subject that is of great importance in the transportation sector, which is increasingly demanding in terms of high-level technology. To understand the mechanics of filled rubbers, one needs to combine the effect of dynamical heterogeneities on the dynamics of confined polymers and the yielding on polymer matrix mechanical response with the image of the particles network. Indeed, polymer bridges that mechanically connect the rigid particles dominate the mechanics of filled rubbers. More precisely, three effects on the viscoelastic modulus can be discussed precisely using the concepts of glassy bridge and confined polymer properties; the effect of pressure—that decreases the thickness of glassy bridges, the effect of temperature—that controls the rigidity of the glassy bridges, and the effect of strain amplitude—that controls their strain-softening.

Conflicts of interest

Authors have no conflict of interest to declare.

Acknowledgements

All the results presented in the article were obtained during the theses of five students who have worked since 1999 on the mechanical properties of filled elastomers: Julien Berriot, Thomas Chaussée, Aurélie Papon, Davide Colombo and Jonathan Champagne. The authors gratefully acknowledge their contribution as well as financial support from the companies Rhodia (now Solvay) and Hutchinson. Francois Lequeux acknowledges the 2020 award from the Académie des Sciences and the Michelin foundation.

References

[1] S. Kaufman, W. P. Slichter, D. D. Davis, "Nuclear magnetic resonance study of rubber–carbon black interactions", *J. Polym. Sci. B Polym. Phys.* **9** (1971), p. 829-839.
[2] J. Berriot, H. Montes, F. Lequeux, D. Long, P. Sotta, "Evidence for the shift of the glass transition near the particles in silica-filled elastomers", *Macromolecules* **35** (2002), p. 9756-9762.
[3] J. Berriot, H. Montes, F. Lequeux, D. Long, P. Sotta, "Gradient of glass transition temperature in filled elastomers", *Europhys. Lett.* **64** (2003), p. 50-56.
[4] A. Papon, H. Montes, M. Hanafi, F. Lequeux, L. Guy, K. Saalwächter, "Glass-transition temperature gradient in nanocomposites: evidence from nuclear magnetic resonance and differential scanning calorimetry", *Phys. Rev. Lett.* **108** (2012), article no. 065702.
[5] A. R. Payne, "The dynamic properties of carbon black-loaded natural rubber vulcanizates. Part I", *J. Appl. Polym. Sci.* **6** (1962), p. 57-63.
[6] J. L. Keddie, R. A. L. Jones, "Glass transition behavior in ultra-thin polystyrene films", *Isr. J. Chem.* **35** (1995), p. 21-26.
[7] D. S. Fryer, P. F. Nealey, J. J. de Pablo, "Thermal probe measurements of the glass transition temperature for ultrathin polymer films as a function of thickness", *Macromolecules* **33** (2000), p. 6439-6447.
[8] B. D. Vogt, "Mechanical and viscoelastic properties of confined amorphous polymers", *J. Polym. Sci. B Polym. Phys.* **56** (2018), p. 9-30.
[9] M.-J. Wang, "Effect of polymer-filler and filler-filler interactions on dynamic properties of filled vulcanizates", *Rubber Chem. Technol.* **71** (1998), p. 520-589.
[10] S. S. Sternstein, A.-J. Zhu, "Reinforcement mechanism of nanofilled polymer melts as elucidated by nonlinear viscoelastic behavior", *Macromolecules* **35** (2002), p. 7262-7273.
[11] J.-L. Barrat, J. Baschnagel, A. Lyulin, "Molecular dynamics simulations of glassy polymers", *Soft Matter.* **6** (2010), p. 3430-3446.
[12] N. A. García, J.-L. Barrat, "Entanglement reduction induced by geometrical confinement in polymer thin films", *Macromolecules* **51** (2018), p. 9850-9860.
[13] M. Vladkov, J.-L. Barrat, "Local dynamics and primitive path analysis for a model polymer melt near a surface", *Macromolecules* **40** (2007), p. 3797-3804.
[14] J. D. Ferry, *Viscoelastic Properties of Polymers*, Wiley, New York, USA, 1980.
[15] D. Long, F. Lequeux, "Heterogeneous dynamics at the glass transition in van der Waals liquids, in the bulk and in thin films", *Eur. Phys. J. E* **4** (2001), p. 371-387.
[16] J. Perez, *Physics and Mechanics of Amorphous Polymers*, Routledge, London, UK, 1998.
[17] J. S. Langer, "Shear-transformation-zone theory of plastic deformation near the glass transition", *Phys. Rev. E* **77** (2008), article no. 021502.
[18] M. Rubinstein, S. Panyukov, "Elasticity of polymer networks", *Macromolecules* **35** (2002), p. 6670-6686.
[19] G. R. Strobl, *The Physics of Polymers: Concepts for Understanding Their Structures and Behavior*, Springer-Verlag, Berlin, Heidelberg, 2007, e-books.
[20] G. B. McKenna, S. L. Simon, "50th anniversary perspective: challenges in the dynamics and kinetics of glass-forming polymers", *Macromolecules* **50** (2017), p. 6333-6361.
[21] L. Berthier, G. Biroli, "Theoretical perspective on the glass transition and amorphous materials", *Rev. Mod. Phys.* **83** (2011), p. 587-645.
[22] S. Merabia, D. Long, "Heterogeneous dynamics at the glass transition in van der Waals liquids: Determination of the characteristic scale", *Eur. Phys. J. E* **9** (2002), p. 195-206.

[23] A. Dequidt *et al.*, "Heterogeneous dynamics and polymer plasticity", *Macromolecules* **49** (2016), p. 9148-9162.
[24] H. Montes, A. Belguise, S. Cantournet, F. Lequeux, "Modeling the mechanics of amorphous polymer in the glass transition", in *Mechanics and Physics of Solids at Micro- and Nano-Scales* (I. R. Ionescu, S. Queyreau, C. R. Picu, O. U. Salman, eds.), Wiley, London, UK, 2019, Ch. 9, p. 231-262.
[25] R. J. Masurel *et al.*, "Role of dynamical heterogeneities on the viscoelastic spectrum of polymers: a stochastic continuum mechanics model", *Macromolecules* **48** (2015), p. 6690-6702.
[26] H.-N. Lee, R. A. Riggleman, J. J. de Pablo, M. D. Ediger, "Deformation-induced mobility in polymer glasses during multistep creep experiments and simulations", *Macromolecules* **42** (2009), p. 4328-4336.
[27] D. R. Long, L. Conca, P. Sotta, "Dynamics in glassy polymers: The Eyring model revisited", *Phys. Rev. Mater.* **2** (2018), article no. 105601.
[28] A. Belguise, S. Cantournet, F. Lequeux, H. Montes, "Weak nonlinearities in viscoelastic mechanical properties of polymers near their glass transition: Local versus macroscopic laws for stress-induced acceleration of the mechanical response", *Phys. Rev. Mater.* **5** (2021), article no. 033601.
[29] A. Dequidt, D. R. Long, P. Sotta, O. Sanséau, "Mechanical properties of thin confined polymer films close to the glass transition in the linear regime of deformation: theory and simulations", *Eur. Phys. J. E* **35** (2012), article no. 61.
[30] R. J. Masurel *et al.*, "Role of dynamical heterogeneities on the mechanical response of confined polymer", *Phys. Rev. Lett.* **118** (2017), article no. 047801.
[31] A. P. Holt *et al.*, "Dynamics at the polymer/nanoparticle interface in poly(2-vinylpyridine)/silica nanocomposites", *Macromolecules* **47** (2014), p. 1837-1843.
[32] J. G. Meier, M. Klüppel, "Carbon black networking in elastomers monitored by dynamic mechanical and dielectric spectroscopy", *Macromol. Mater. Eng.* **293** (2008), p. 12-38.
[33] H. Montes, T. Chaussée, A. Papon, F. Lequeux, L. Guy, "Particles in model filled rubber: Dispersion and mechanical properties", *Eur. Phys. J. E* **31** (2010), p. 263-268.
[34] J. Champagne *et al.*, "Role of glassy bridges on the mechanics of filled rubbers under pressure", *Macromolecules* **53** (2020), p. 3728-3737.
[35] A. D. Drozdov, A. Dorfmann, "The payne effect for particle-reinforced elastomers", *Polym. Eng. Sci.* **42** (2002), p. 591-604.
[36] H. Montes, F. Lequeux, J. Berriot, "Influence of the glass transition temperature gradient on the nonlinear viscoelastic behavior in reinforced elastomers", *Macromolecules* **36** (2003), p. 8107-8118.

Comptes Rendus
Physique
2021, 22, nº S5, p. 51-71
https://doi.org/10.5802/crphys.95

Prizes of the French Academy of Sciences 2020 / *Prix 2020 de l'Académie des sciences*

Chipless labels detection by backscattering for identification and sensing applications

Détection d'étiquettes sans puce par rétrodiffusion pour des applications d'identification et de détection

Etienne Perret [a, b]

[a] Univ. Grenoble Alpes, Grenoble INP, LCIS, France

[b] Institut Universitaire de France, 75005 Paris, France
URL: https://www.scattererid.eu/scattererid-project-team/#principal

E-mail: etienne.perret@lcis.grenoble-inp.fr

Prix Espoir IMT – Académie des sciences 2020

Abstract. There is currently a growing interest in the development of communication systems that consume as little energy as possible, with the idea of eliminating the presence of batteries, which are a very polluting component. This is why the principles of communication based on backscatter modulation, or even more simply on backscattering by a device that takes the form of a label, like a barcode, are being studied more and more. In the latter case, the idea is to use the radar signature of this totally passive label, the geometry of the elements printed on it having been specially designed to perform the desired functions. These new systems cannot claim to do the same things as those working with a power supply or a chip, but they may be of interest for certain applications where the reading distances do not exceed one metre. Compared to barcodes, the main advantages are related to the use of RF waves to communicate, which makes it possible to read through certain objects that are opaque to light, or to significantly reduce the acquisition time of identifiers by being able to scan larger reading areas more easily.

Résumé. Il existe actuellement un intérêt croissant pour le développement de systèmes de communication consommant le moins d'énergie possible, avec l'idée d'éliminer la présence de batteries, qui sont des composants très polluants. C'est pourquoi on étudie de plus en plus les principes de communication RF basés sur la retro-modulation, ou même plus simplement sur la rétrodiffusion d'une onde par un dispositif qui prend la forme d'une étiquette, comme un code-barres. Dans ce dernier cas, il s'agit d'utiliser la signature radar de cette étiquette totalement passive; la géométrie des éléments imprimés sur celle-ci ayant été spécialement conçue pour remplir les fonctions souhaitées. Ces nouveaux systèmes ne peuvent prétendre faire les mêmes choses que ceux fonctionnant avec une alimentation ou une puce, mais ils peuvent être intéressants pour certaines applications où les distances de lecture ne dépassent pas un mètre. Par rapport aux code-barres, les principaux avantages sont liés à l'utilisation des ondes RF pour communiquer, ce qui permet de lire à travers certains objets opaques à la lumière ou encore de réduire significativement le temps d'acquisition des identifiants en pouvant balayer plus facilement de plus grandes zones de lecture.

Keywords. Chipless radio frequency (RF) identification (RFID), Backscattering communication, Sensor tags, Aspect-independent parameters extraction, Radar cross section (RCS), RF scatterer.

Mots-clés. Identification par radiofréquence (RFID) sans puce, Communication par rétrodiffusion, Étiquettes-capteurs, Extraction de paramètres indépendante de l'orientation, Surface équivalente radar (SER), Diffuseur RF.

Available online 16th March 2022

1. Introduction

Despite our advanced communication systems, humans lack an easy way of interacting with everyday objects. Over centuries human beings interacted mechanically with physical, non-electronic, objects. The development of electronic devices has introduced non-natural interactions, with cumbersome, wire connected devices requiring a significant expertise and time investment. With the advent of wireless technologies, one would expect more natural handlings of objects to replace these non-ergonomic interactions. Although considerable progress has been made in recent years, particularly in smartphones, the fact that these devices need a battery to operate still makes their use restrictive. Today, the objective of more and more researchers is to develop electronic systems that communicate without wires and without batteries. From an application point of view, such systems already exist but remain confined to the field of identification as it is the case for Radio Frequency IDentification (RFID).

In RFID, the tag consists of an antenna and a chip that is self-powered by the EM wave emitted by the reader. A considerable number of studies have been carried out in recent years to extend the number of functionalities of these tags, in particular to allow them to have a sensor function. However, even if these systems consume much less energy than systems with a battery, they are still based on the use of a silicon chip, which has also a strong impact on the environment, especially when we are talking about tens of billions of tags sold per year. It therefore seems interesting to wonder what can be done in terms of applications with a system of tags without chips. Could wireless electronic systems be turned into chipless devices that can be printed with common printers, even simpler than a common passive RFID tag? Could this new technology be compatible with easier interactions with physical objects, and be able to connect them wirelessly to the internet? Indeed, can't we introduce a chipless RF reading technology closer to the barcode application that is currently very popular? Barcodes are very present around us for the identification and tracking of objects. They work on an optical principle where the information is coded by the geometry of the printed patterns (for example the width of the black strips printed next to each other for EAN13 codes, or the position of the black squares in the case of datamatrix) [1]. Unfortunately, barcodes have significant limitations in that they often have to be read by a human operator. This significantly reduces the reading time when a large number of labels are present on a pallet for example.

Achieving this goal will allow everyone to produce smart electronic labels that could be used for different applications (like identification, sensing or remote control of common electronic devices), with their own printer. To this end, models for "artificial" radar target need to be rethought from a theoretical and practical point of view. Specifically, we propose the new paradigm of "smart chipless electronic labels", that can replace current applications based on classical chipped devices.

Scientifically, while the problem we address is in the field of Radio Frequency communications, this calls for a new convergence with radar approaches, reflectometry principle, and wave interaction with objects. In terms of impact, the resulting "smart paper based electronic label" for human-machine interface will not only serve the needs of scientists or engineers but also of anyone interested in changing the way they interact with objects.

2. Context and state-of-the-art of chipless RFID radar approaches

2.1. *A failure of standard RF identification technologies?*

RFID is one of the major technologies in the field of identification and has grown considerably, since its principle was introduced more than 60 years ago [2]. This is a technique for automatic capture of information contained in a label, by radio waves with a remote reading facility. The label consists of a chip that contains the data and an antenna that allows a communication with a dedicated reader. Many prospective studies show that in coming years the world's demand for traceability is expected to increase considerably, as a result of economic development. However, despite the benefits of RFID deployment, this technology is affected by several economic, technological or societal factors. These obstacles include the tags' cost which is too high for some application sectors, but also the lack of reliability and security in the information contained in the RFID chip. Furthermore, RFID remains a relatively complex technology when compared to the barcodes. Indeed, the barcodes are very simple to implement or to use. They are perfectly standardized and universal in their operating principle. They are also extremely low cost for both the tags and the reader part. However, the main drawback of this technology relies in the way of capturing the information, which most often requires human intervention. In contrast, the main advantage of RFID is the use of radio waves to transfer data, for the purposes of automatically identifying and tracking tags attached to objects. In addition to the flexibility of reading, multiple tags can be read at once. Similarly, it is possible to obtain a substantial read range. However, the RFID solution is complex; it requires the use of a chip and a communication protocol which induces costly tags. Moreover, this solution is not universal, since it requires different frequency bands from one country to another. All these reasons explain why more and more research projects seek to develop new identification systems. Among them, a solution without any chip is very promising.

2.2. *Chipless RFID and state-of-the-art of chipless radar approaches*

The development of chipless radar tags in RF has grown significantly in recent years [3–5]. The principle of information encoding, that is to say the ID label, is based on the generation of a specific electromagnetic signature, a bit like the radar principle: a wave is sent to the tag, a portion of the tag backscattered signal—what we call his EM signature—is retrieved by the reader. The main difference here is that the shape of the conductive pattern forming the tag is imposed (RCS Synthesis) in order to have a specific and perfectly recognizable signature (see Figure 1). Thus, the information is no longer stored within an electronic chip in a classical memory, as can be done in traditional RFID tags, but directly "written" in the label like a barcode.

Figure 1a shows the chipless technology from an application point of view. It shows a pallet with 16 cardboards (marked objects in the figure) on which tags have been placed (on the outside of the carton, like the barcode, each tag has a different geometry/identifier) to identify each cardboard. In the figure, the tag has been shown on the outside of the cardboard for ease of understanding, however unlike barcodes, a chipless tag based on an RF approach can be read through the cardboard. Also, for practical purposes, the tags could still be read if the cardboards were wrapped in a protective plastic film. Similarly, for product integrity reasons, it would also be possible to put the tags inside the cardboards to make them invisible. Another undeniable advantage of RFID chipless technology over barcodes is the ability to significantly increase the speed of reading of the tags on the pallet. Whereas with a barcode, the reader has to be positioned in direct view of each label, chipless tags can be read at greater distances (e.g. 40 cm) and therefore by scanning the area with a handheld reader for example. Figure 1a shows

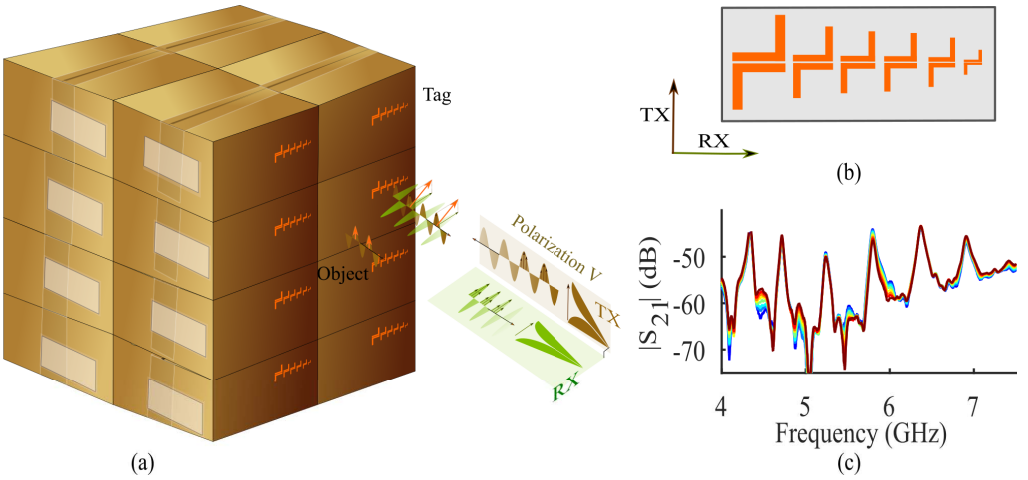

Figure 1. Chipless RFID application principle: (a) Example of the use of chipless technology. Each cardboard is identified by a chipless tag (orange pattern). The identification is done by means of RF waves. The wave backscattered by the object and the tag contains the information that will allow to obtain the identification. Like the barcode, each tag has a different geometry/identifier. (b) Example of a REP chipless tag with 6 independent resonators. (c) Spectrum of the backscattered signal measured for the chipless tag (b) and showing 6 resonance frequencies.

the interaction between the waves sent by the chipless reader (not shown in the figure) and the tag, as well as the backscattered wave which contains the information on the ID of the chipless tag. The tag is shown in Figure 1b. There are many different types of chipless tags, most often consisting of a rectangular plastic (or paper) support with conductive patterns (shown in orange in the figure) printed on it. Some tags have a third metal layer which acts as a ground plane for the structure and which usually isolates the tag from the object and improves the quality factor of the resonators. The shapes of the resonators are obtained from a specific RF design work based mostly on the use of RF simulators [3, 6]. There are many constraints to be taken into account in the design of the tag, such as the amplitude of the backscattered signal (or the radar cross section (RCS) of the tag, a quantity that describes the ability of the tag to reradiate in one direction in space), or the quality factor, which must be as large as possible. The coding capacity of a chipless tag as well as the reading distance are directly linked to this design work. Therefore, a key point is the relationship between the geometry of the conductor pattern and the RF signature expected. To encode information in chipless solutions consists in:

- Detecting the presence or absence of a distinctive portion of signal observed in the time or in the frequency domain (for example a peak or dip associated with a resonance of the conductive pattern of the label—see Figure 1c).
- Measuring precisely the duration or the frequency interval (respectively from the signal represented in the time or the spectral domain) between the presence of distinctive parts of the signal. This physical quantity must be independent of the measurement, for example the distance between the reader and the tag or the presence of objects next to the tag. In this case, the use of resonant devices (resonators), and therefore the detection of their resonance frequency (which is an independent parameter), is of particular interest. This is why the vast majority of chipless tags currently in use are based on the printing of resonant patterns on the label (see Figure 1b). From this, it is possible to establish a bijective link between their resonant frequencies and the corresponding tag ID. This link

can be made in both directions, allowing both the generation of a tag corresponding to a given ID, or the association of an ID with the EM signature of a tag.
- Making these physical quantities extracted from the tag signature totally independent. Indeed, in the case where the tag comprises several resonant patterns, these structures must be decoupled from each other, i.e. the modification of one of the resonance frequencies (and therefore the modification of a specific geometric quantity) must not have any effect on the resonances of the other patterns. These conditions are indispensable for coding information according to this label principle. Note that to increase the coding capacity of the tag, more advanced design methods based on RCS synthesis have also been proposed [6].

One of the first frequency tags was designed on the principle of antennas loaded by resonant structures. In order to decouple transmission from reception as much as possible, these tags were usually made up of two antennas oriented at 90° to each other and connected by a transmission line on which resonators were placed [3, 4]. These cumbersome structures made it possible to demonstrate the principle of information coding but proved to be too inefficient for applications in a real environment.

A decisive turning point for the practical implementation of this technology is linked to the introduction of tags based on the use of resonant patterns. In this case, we no longer try to recover or retransmit the signal with antennas and modify the signal by placing a specific circuit between the antennas. Instead, the emitted signal is directly interacted with the presence of a resonator that stores energy and then backscatters it over a period of time that is related to its quality factor. These "artificial" objects with remarkable properties thus operate on the principle of RF Encoding Particles (REP) and can intrinsically have a characteristic radar signature and thus be directly associated with an identifier [3, 7]. The functions of receiving, signal processing and transmitting are not separated from each other, both in terms of the concept and the geometry of the tag (see Figure 1b). In this case, REP tags act as transmitting, receiving and filtering devices at the same time [8, 9]. Also, these tags do not have antennas, or transmission lines, which are too cumbersome and restrictive for the development of chipless RFID tags. Thus, like RF barcodes, tags designed on this principle are extremely simple and most often the resonant frequency is directly linked to a characteristic pattern length that can be modified to change the tag ID. Similarly, to increase the coding capacity, it is possible to place several resonators on the same tag and thus reach several tens of bits (see Figure 1b).

Based on the REP approach a substantial amount of research work was focused on demonstrating the potential of chipless radar approaches for scientific (remote characterization of RF devices [10–12]) and engineering applications (identification—chipless RFID [5]). An important number of these articles have addressed technical challenges, such as the tag encoding capacity [9,13], the robustness of detection [14–17], the sensitivity of detection based on the relative orientation between the reader and the tag [18–21], the cost of both the tag and the reader [22–24], and finally, compliance with RF emission regulations [25]. A tag demonstrated a capacity of 49 bits [18], proving for the first time that chipless technology can have a comparable encoding capacity to the well-known international article number EAN 13 [(EAN), formerly the European article number] bar code technology. The widespread application of chipless RFID is intimately linked to the manufacturing cost of the tags. The feasibility of large scale chipless tag production has been shown with a unit cost of about €0.004 [24]. These figures are following some institutes' forecast. Indeed, it has been demonstrated that a REP chipless tag based on a paper substrate can be manufactured using the flexography technique, which is an industrial high-speed printing process. Everyone can also use a common low-cost component off the shelf (COTS) inkjet printer to produce such tags. Here, the only difference with the barcodes is the use of a conductive ink which is at the origin of the specific EM signature of the tag.

In practical terms, it is now expected to show that it is possible to associate the chipless label ID with other features like the ability to: (1) write and rewrite the information (ID) [26], (2) associate an ID with a sensor function [27, 28], (3) associate an ID with gesture recognition [29, 30]. As compared to the barcodes, the chipless technology must bring other features that are impossible to implement with the optical approach, while remaining a very low-cost approach, that is to say, a printable one. This is why the writing/rewriting, sensor capabilities and gesture recognition are crucial features for the large-scale development of such a technology. For instance, the development of very low-cost sensor tags is now eagerly awaited for.

Could wireless electronic systems be turned into chipless devices that can be printed, and even simpler to use than a common passive RFID tag? Could it be possible to rewrite data using only a paper label and a common inkjet printer? Could these chipless labels replace classical remote control for specific applications? These are the questions we are asking ourselves and to which we are seeking to provide concrete answers, particularly within the framework of the ScattererID project [31].

3. Challenge: retrieve the label data from its backscattered wave in an unknown environment

To achieve this goal, developing these smart chipless labels based only on the extension of existing approaches is far from sufficient. Existing models need to be totally re-thought, in order to give the possibility to add these awaited new functionalities. In other words, rewritable capability needs to borrow a concept from memory and revisit tag models from a user-centered perspective. It is the same thing for the sensing and gesture recognition part. Therefore, we will explore the new paradigm of "smart chipless electronic label", namely, a paper-based green electronic compatible solution with advanced functionalities and designed to allow an intuitive interaction with users.

We will then discuss some essential aspects relating to the challenge of retrieving the label data from its backscattered wave in an unknown environment. We will be interested in: (a) the isolation between the signals reflected by the tag and the much more significant ones reflected by the environment around the tag, (b) aspect-independent parameters extraction, which is essential to recover the ID of the tag, (c) the level of sensitivity on the measurement, which can be achieved and which allows to determine possible sensor applications.

3.1. *Spatial isolation of signals*

The vast majority of objects are characterised by RCS values that increase with their geometric dimensions and with the frequency of the EM wave. Thus, we have around us objects with very different RCS values, some of which (such as metallic objects) can be very large when compared to the RCS values of chipless tags (at best the RCS of a chipless tag is less than -10 dBm at UWB frequencies between 3 and 10 GHz). Therefore, an important task when designing chipless tags is to find shapes that allow the highest RCS values to be obtained with the highest possible quality factors. However, the limitations imposed by the application (geometry of the tags with a credit card format—frequencies in the UWB band…) mean that it is not possible to obtain tags with RCS values that are much higher than the ones of surrounding objects. In fact, we usually end up with tag RCS that can be a thousand or even a million times weaker than the surrounding object ones. This is why, in order to be able to read a chipless tag in a real environment, without a complex calibration system (which would mean imposing that we know the environment), we need to implement specific strategies such as the isolation of signals between the tag and

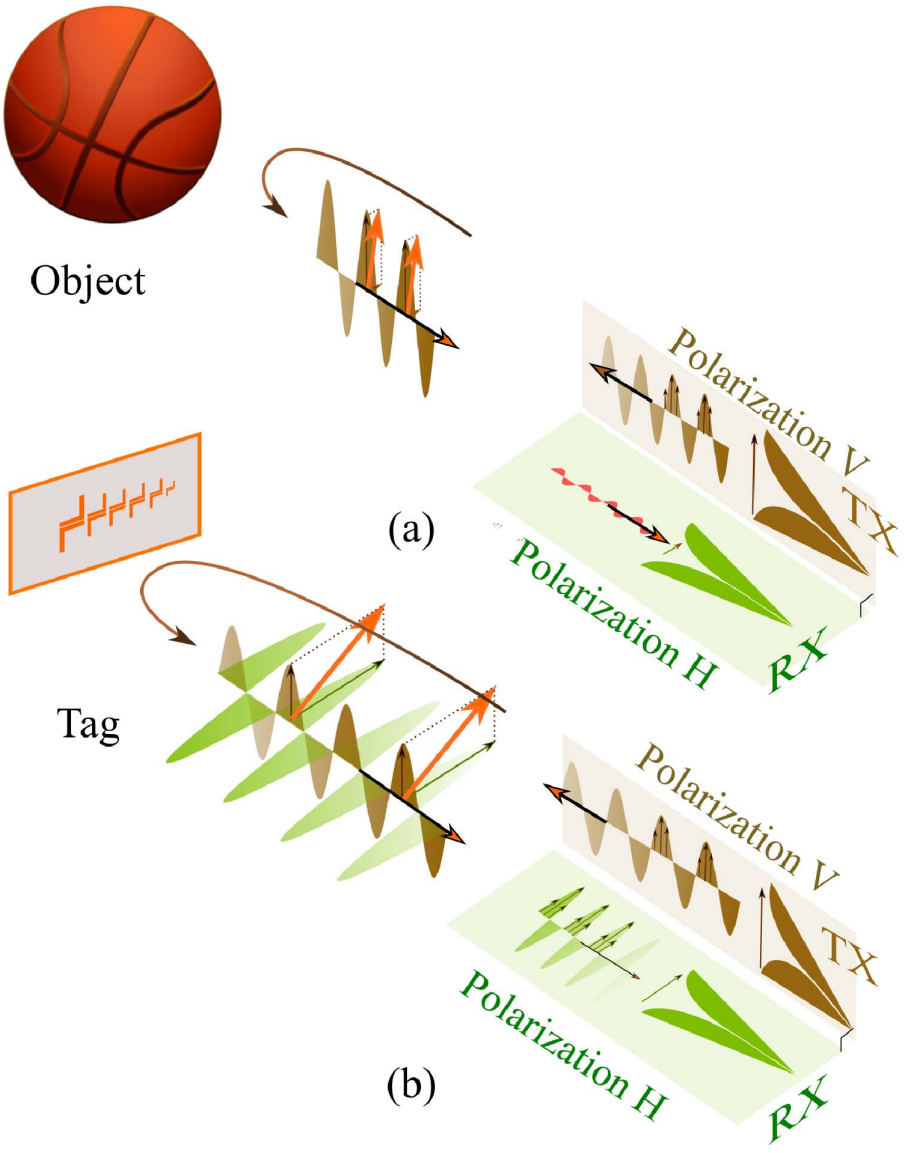

Figure 2. Principle of cross polarisation measurement applied to chipless RFID. (a) The field backscattered by a large number of objects has the same polarisation as the incident wave. (b) The chipless tag is designed to backscatter a field perpendicular to the incident field. In practice, the tag is surrounded by objects, and the situation (a) and (b) are superimposed, which makes it possible to isolate the tag signal from the total backscattered signal.

those linked to the environment, from a spatial and temporal point of view. A good spatial isolation is achieved by working in cross-polarisation [3, 32]. The principle is illustrated in Figure 2. Indeed, a vertically polarised signal is transmitted and only the horizontally polarised backscattered component is recovered at the reader. The advantage here is to seek to put oneself in an environment that contains objects that tend not to change the polarisation of the incident

wave as it is the case with the balloon in Figure 2a. This constraint is relatively simple to respect in practice as objects are often oriented vertically or horizontally (especially metallic structures which have high RCS), which allows to respect the case described by the Figure 2a. In this case, the tag must be able to change the polarisation of the incident wave. The first generation of chipless tags with two antennas were directly compatible with this approach as it was sufficient to impose a 90° angle between the two antennas. For REP tags, specific design work has shown that by simply modifying the geometry of the scatterers [32], it is possible to obtain the same effect (see Figure 2b). It has even been recently shown that with the REP approach (as opposed to the two-antenna approach) it is possible to design resonators that depolarise the incident wave regardless of the orientation of the tag with respect to the incident wave [33]. It is thus shown that it is possible to have either tags of this type that are totally invariant (backscattered wave of constant amplitude regardless of the orientation of the emission), or tags that guarantee a certain level of signal (non-zero) in cross-polarisation regardless of their orientation with respect to the emission. With this approach based on a cross-polarisation measurement, we show that we can reduce the importance of the surrounding objects by 20 to 30 dB, which is a way to isolate the signal backscattered by the tag from the total backscattered field.

3.2. *Temporal isolation of signals—aspect-independent parameters extraction*

In order to be able to carry out a measurement without any calibration (i.e. a measurement in which the tag has been removed from the scene and which will be subtracted from the following measurements in which the tag will be present), the spatial isolation described above must be completed by a temporal isolation whose basis is the resonant character of the scatterers used to make the tag. Indeed, the resonant character of the tag has a double importance. As described above, it is the basis of the coding used for this type of tag, where the resonant frequencies will enable the information to be coded. It will also play a discriminating role in the tag's reading robustness. Indeed, as shown in Figure 3, it is possible to use the resonant character of the scatterers to temporally isolate the tag from its environment and thus be able to measure the resonance frequencies precisely. The principle is also based on the idea that this resonant character is not present in everyday objects. In this respect, it should be noted that a great deal of design work, particularly in the choice of materials and geometries, is necessary to have good resonators on chipless RFID tags. The signal backscattered by these everyday objects (which, as previously mentioned, can have very high RCS) will have a duration similar to that of the incident pulse. This is known as a quasi-optical reflection; an illustration is given in Figure 3b. This behaviour is very different from that of a good resonator (quality factors between 100 and 150 can be obtained in the UWB band with printed techniques). These will act as a very selective filter and the backscattered field will have a much longer duration than the incident pulse. For example, a UWB pulse emitted by a chipless reader will have a duration of a few nanoseconds (less than 5 ns) whereas the duration of the field backscattered by the chipless tag from this same pulse will have a duration of around 20 ns. Also, on this principle, as illustrated in Figure 3b, it is possible to separate the signal backscattered by the tag from other signals which may have higher amplitudes. It is possible to perform cross-polarisation readings and time windowing in order to cumulate both effects (see Figure 3b). However, as shown in Figure 3c, it is also possible to recover the useful signal from the backscattered signal in co-polarisation. However, the amplitude variations between the tag signal and the other signals are much greater, which can cause problems, particularly in the reader's receiver amplification chain. It has been shown that this temporal windowing is nothing other than a method allowing aspect-independent parameters extraction, i.e. we can recover the characteristics specific to the tag's resonators, i.e. their resonance frequency and their quality factor [34]. These characteristics are

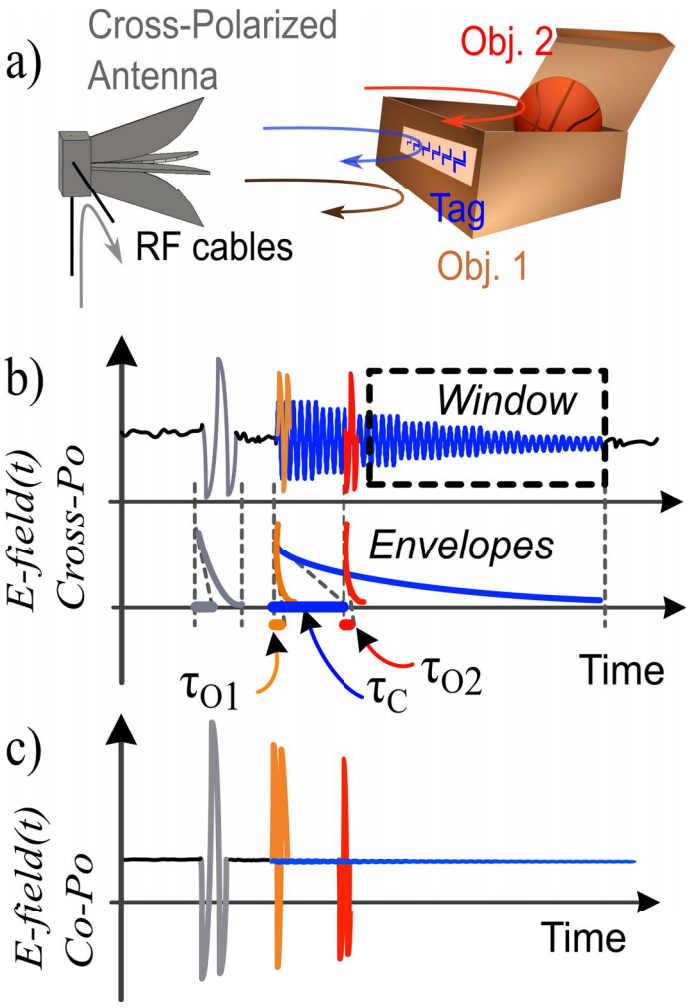

Figure 3. Illustration of the time separation used in chipless RFID technology. (a) The tag is read with an antenna that will be characterised by an isolation between the horizontal and vertical polarisation. This imperfection causes a replica of the transmission pulse in grey on the figure. The presence of objects will also send back signals with a duration similar to that of the incident pulse, which is very different for the tag, which is composed of resonant scatterers. (b) Temporal presentation of the signals reflected by the objects and the tag for a cross-polarisation reading. It is possible to define a time window where the signal corresponds almost exclusively to that linked to the tag. (c) Same as (b) but for a co-polarisation reading. The signals reflected by the objects have a much greater amplitude than the one linked to the tag.

essential for coding the information as they do not depend on the measurement itself, i.e. the distance, the orientation of the tag, the surrounding objects or even the type of antenna used. It is therefore important to be able to retrieve them as accurately as possible. However, at the level of information recovery, it is possible at first sight to associate the resonance frequency with the search for a maximum in the spectrum of the backscattered signal. However, if we look more precisely, without any particular signal processing, this maximum does not only describe

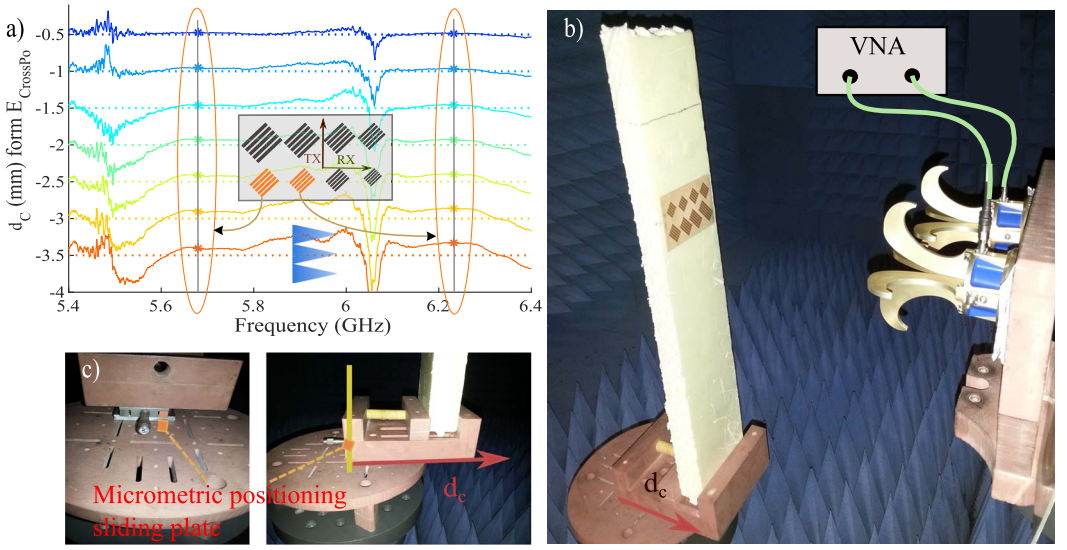

Figure 4. Illustration of the level of accuracy achievable with a chipless tag. Application to displacement measurement. The tag used has 8 scatterers with resonance frequencies between 3.34 to 6.8 GHz. (a) Extraction of the displacement d_c from the measurement of S-parameters (S21) in an anechoic chamber. (b) Bench used, description of the measurement using a VNA. (c) Details on how displacements of 100 to 500 µm were achieved in practice.

the resonance mode of the tag but also the quasi-optical mode of the tag itself, not to mention the effect of surrounding objects when they are present. So, the frequency associated with this maximum can move as a function of the reading itself, which shows that this approach does not detect the resonant frequency of the tag [34]. The temporal windowing approach coupled with a spectrogram representation has been used to recover tag information in real environments and even without any calibration, which is very complicated to do in practice [34]. This approach is essential to efficiently read a tag in a real environment and is all the more relevant when the quality factor of the tag is important.

3.3. *Level of accuracy of the backscattered signals from a chipless RFID tag*

Particular attention has been paid to the possibility of identification with this radar approach, where the identifier is linked to the geometry of the resonators present on the tag. However, like the radar applications known to allow the remote recovery of potentially very precise information such as the speed of a vehicle, to name but one, the signals retrieved by a chipless reader can contain much more than an identifier [3]. This is particularly interesting in chipless RFID as the radar target in this case is specifically designed to have special properties. Thus, we were able to show that this approach is compatible with the remote measurement of a large number of physical quantities ranging from temperature, humidity, or electrical/thermal quantities of materials such as permittivity/thermal expansion coefficient. This idea of using a radar approach on resonant targets to make precise measurements of physical quantities follows a first characterisation which aimed to measure the smallest possible displacement (noted d_c in Figure 4) of a tag. Indeed, if we are interested, in this case, in the variation of the phase of the backscattered signal, it is possible to derive analytically the displacement of the tag (see Figure 4a). By exploiting resonance frequencies, cross-polarisation and time windowing, we have been able to show that it is

possible to measure these displacements even through objects (such as a cardboard box or plastic tab) or even to identify individually the displacement of different tags positioned at the same time in front of the reader [35,36]. Figure 4 shows some results obtained in an anechoic chamber where one can see the procedure used to make the measurements. It can be seen in Figure 4a that around the resonance frequencies (vertical lines), the extracted displacement value is the smoothest and flattest part of the curve, this being due to the fact that it is at these frequencies that the best SNR is obtained. The results obtained in terms of accuracy are remarkable. Indeed, a displacement of 100 μm can be measured with this approach [36]. The error of the displacement measurement can be reduced by using several resonators, each of them allowing to recover a displacement value. Finally, it was found that for displacements greater than or equal to 400 μm, the error on the measurement is less than 15 μm.

Thus, this example illustrates the potentially high sensitivity of the chipless approach, and several application areas are possible. Indeed, by perfectly controlling the environment, for example by positioning the tag in an anechoic environment, by choosing a highly resonant tag (with a quality factor of the order of 150), as well as a very precise measuring device such as a network analyser (VNA), it is possible to measure variations in resonance frequency of less than 1 MHz when the measurement is reproduced identically by removing the tag each time. If we compare these values with those related to the effect on the length of a 3 cm metal loop for a temperature variation of a few degrees, we realise that we are on the same order of magnitude. Indeed, the thermal expansion modifies the geometric dimension of the loop and thus its resonance frequency. Thus, based on this principle, it is possible to carry out very precise measurements, remotely, such as the characterisation of the dilation coefficients of metals [12]. If, on the other hand, the temperature dependence of the materials that make up the tag is considered to be known, it is possible to use it as a temperature sensor [27,37]. Results on tags with no specific material (i.e. known to be particularly temperature sensitive) have shown that it is already possible to trace the temperature, simply by modelling the effect of thermal expansion and the temperature dependence of the dielectric. As these input data are usually present in the material datasheets, this shows that it is very simple to create a sensor with the chipless approach. Recent studies also show that a conventional chipless tag can be used to measure temperature and humidity at the same time. Taking advantage of the simple geometry, it is possible in this case to have an analytical approach to model both the temperature and humidity dependence of the resonant frequency and to extract these two physical quantities [37].

4. New features in RFID chipless

4.1. *Rewritable chipless RFID label*

As said previously, advances in the field of chipless RFID applications are primarily based on significant technological breakthroughs. For instance, the possibility of designing rewritable and low-cost printable tags involves the development of original approaches at the forefront of progress, like the use of structures from conductive-bridging random-access memories (CBRAM) microelectronics technology, allowing to achieve reconfigurable elements based on Nano-switches [38,39].

Like the barcodes, the chipless tags' information cannot be changed: once the tag has been printed, the information is recorded in hard copy. To obtain the "writing/rewriting" function, a specific element presenting two clearly distinct states must be implemented in the label. This element must be perfectly controllable and must allow modifying the EM signature of the tag, that is to say its ID. This behaviour can be obtained with a RF switch; the major differences here are that (1) this device must be printed simultaneously with the label conductive pattern and

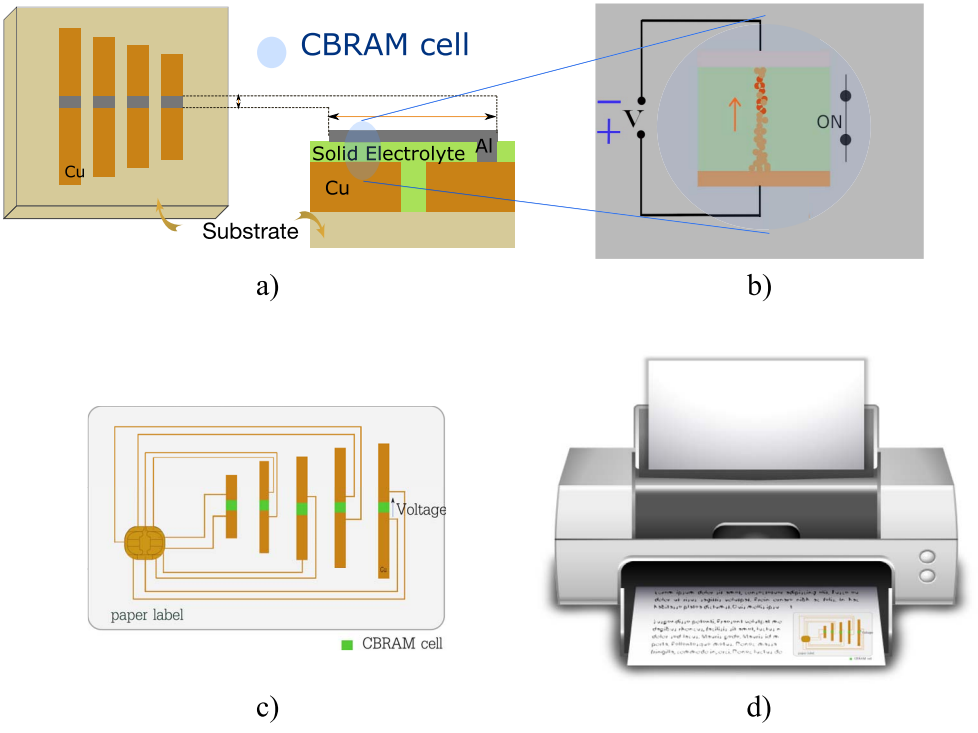

Figure 5. Use of CBRAM technology to produce rewritable RFID chipless labels. (a) Example of the implementation of a CBRAM cell at the level of a resonator. (b) Operating principle of the CBRAM cell, the formation of a filament ensures electrical conductivity between the two electrodes (ON state). (c) Example of an RFID chipless label printed in credit card format with the supply lines. (d) Illustration of the problem of manufacturing these labels where the objective is to be able to print them with conventional printing means.

(2) the switch must keep its state even in the absence of any applied power. A simple and flexible technology in terms of manufacturing is needed. Such a function can be obtained with a physical principle currently being studied to realize the future non-volatile fast access memories (known under different names including Memristors or CBRAM) [40]. It was particularly interesting to work on the principle of CBRAM in order to perform RF switches that could be used to rewrite our chipless tags (see Figure 5). The CBRAM technology has shown the potential to operate at lower energies and voltage (couple of volts), making it particularly interesting for embedded applications [40].

4.1.1. *Operating principles of CBRAM*

The RF switches that have been developed are based on MIM structures (Metal Insulator Metal—Figure 5b), that is to say a stack of three layers, with no moving parts. Moreover, they are fully compatible with many low cost fabrication approaches and simple to implement [41,42] (see Figure 5c, d). By carefully choosing materials and their thicknesses, it is possible to show that such a structure acts as a programmable resistor that keeps its value in the absence of any power control (see Figure 5b). Under the action of an electric field between the two electrodes, the insulator (which is a solid electrolyte) allows the migration of ions, which come from the active electrode, towards the inert electrode. The ions are then deposited on the inert electrode and are reduced with electrons to obtain the Cu or Ag metal.... This way, a conductive filament grows

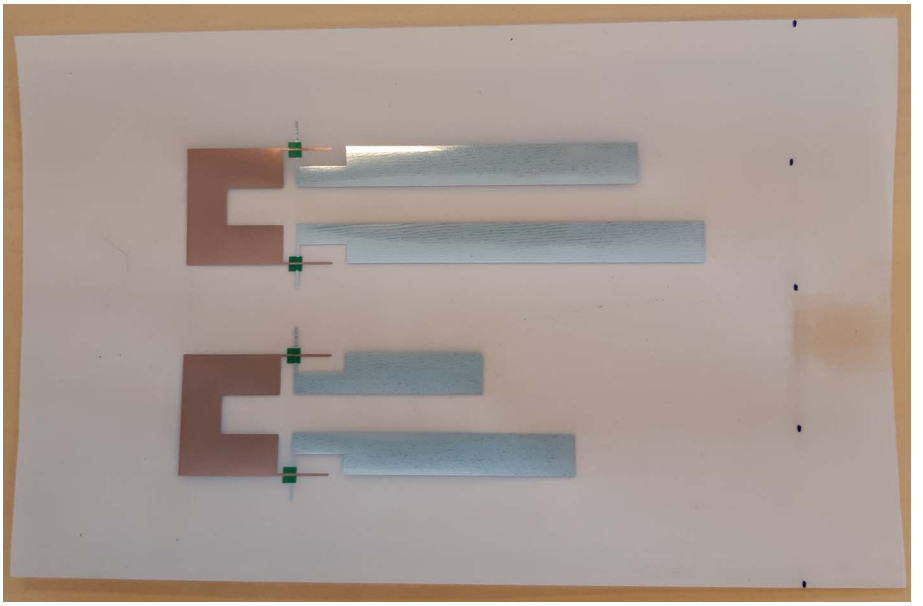

Figure 6. Photo of the first rewritable chipless tags made entirely through printing. The metals used are copper and aluminium.

until it touches the active electrode (see Figure 5b). The device then switches to a conducting state (ON). To break the filament and return to the OFF state, we simply have to reverse the voltage.

We will note here the significant divergences that exist in terms of specifications and desired performance between memories and RF switches, which are very different applications from an applicative point of view. In the case of memories, consumption and time of switching/memory access are determining factors, while in RF, it is above all frequency behaviour and particularly the insertion loss in the ON state that is decisive. The main differences between memories and the RF switch version can be found in the dimensions of structures. In RF, the lowest COFF capacity possible must be reached. We must also seek configurations in which the dielectric is as thick as possible; that is, it must absolutely be significantly thicker than 100 nm, generally used for memories. Studies have shown that it is possible to execute switching with thicknesses of several hundred nanometers [43]. A work closer in nature to the function desired for chipless tags has shown the possibility of producing an RF switch operating between 1 and 6 GHz [44]. A comparison with switches based on classic approaches is presented in [44], and the results are spectacular. To provide proof-of-concept for the integration of RF switches using CBRAM in a chipless tag, the use of common, printable materials is expected. A photograph of a tag made entirely by printing is shown in Figure 6. The tag is made on flexible PET laminates with copper and aluminium as metals. A complete study of the performance of this tag is given in [26].

4.1.2. *Example of a reconfigurable chipless tag*

The CBRAM structure is extremely simple. Figure 5a shows an example of the implementation of this technology in a chipless tag in order to make it rewritable. The RF switch is used to modify the geometric length of the tag and thus its resonance frequency. As an example, in Figure 5a, the arrangement of switches at the centre of the dipoles makes it possible to obtain basic OOK coding in frequency. We can see in this figure how the reconfigurable element, the CBRAM cell, could be integrated. With the Cu/Nafion/Al layers, filaments inside the solid electrolyte dielectric can be

created to produce a short circuit. In terms of realization, if we start from a classical chipless tag (that is, a substrate with a conductive pattern), we must begin by depositing the dielectric layer, being careful to leave a copper access area on the arm that does not contain the MIM structure. After this, we must deposit aluminium in such a way as to cover part of the arm of the antenna, thus creating the MIM stacking and ensuring electrical contact with the other arm. This results in a horizontal stacking of layers (out-of-plane RF switch). It is also possible to create a vertical MIM structure (in-line RF switch), but the thinness of the dielectric (typically of the order of a few hundred nanometers) makes this second configuration more difficult to achieve in practice. Next, to create the dielectric layer, various solutions are possible (such as, for example, the deposit of resins (PMMA/Nafion) via spin coating to preserve simple production techniques [41]), and need to be tested to improve the RF switch performances for chipless applications.

The principal result obtained is that it is possible to obtain very low ON-state resistances of the order of a few ohms, which makes this technology compatible with RF applications. With several volts (from 1 to 20 V depending on the dielectrics and thicknesses used), an ON state can be obtained, and an OFF state achieved by reversing the voltage.

4.2. *Remote sensor based on chipless label*

Still on the idea of low cost printed labels, it would be quite relevant to perform a new generation of sensors that are identifiable, easy to use, and able to fulfill the pressing need to make objects able to communicate with one another. It would be of particular interest to be able to read an identification code providing information about the content of an object—data on its hygrometry, for example (see Figure 7). We would have access to an object-tracking system that would be remote and extremely complete, all using low-cost technology. For this, the production of chipless tag-sensors is a very attractive solution. Compared to the classic RFID solution, besides increased precision, the ability to avoid chip-related constraints reduces cost, increases life span, and results in tags that are more mechanically robust overall, with much higher resistance to vibration and temperature. Based on the chipless technology, the idea here is to add a sensor function. Various materials can be used to do this, for example nanomaterials. Silicon nanowires have geometries and dimensions with a very high surface-to-volume ratio, thus encouraging surface interactions. Given the very small dimensions of these structures (the diameter of a nanowire can be of the order of a few dozen nanometers), exchanges or harnessing of molecules can take place on the surface, permitting a modification of electrical properties depending on the environment in which they are placed (see Figure 7).

These nanomaterials have been studied for several years already, and the possibility of using them as sensors, particularly wireless sensors, has been demonstrated [28].

Figure 8 describes the operating principle used to produce a chipless tag comprising an ID and a sensor function. The principle of associating an ID with an RF signature (backscattered field or RCS) is shown in Figure 8a. We can see in Figure 8b that for the sensor function, the idea is to use, in contact with a resonator, a material sensitive to the quantity to be measured. The electrical variations (permittivity and losses) of this material as a function of the quantity to be measured will directly impact the resonance frequency (as well as the amplitude/phase of the corresponding peak—resonance frequency—obtained on the field backscattered by the resonator). Thus, it is possible to trace the value of the physical quantity through the measurement of this backscattered field, most often through the value of the resonance frequency. The correspondence between the resonance frequency and the value of the physical quantity is usually done using a lookup table or, when the problem is simple enough, by a direct analytical model [27,37].

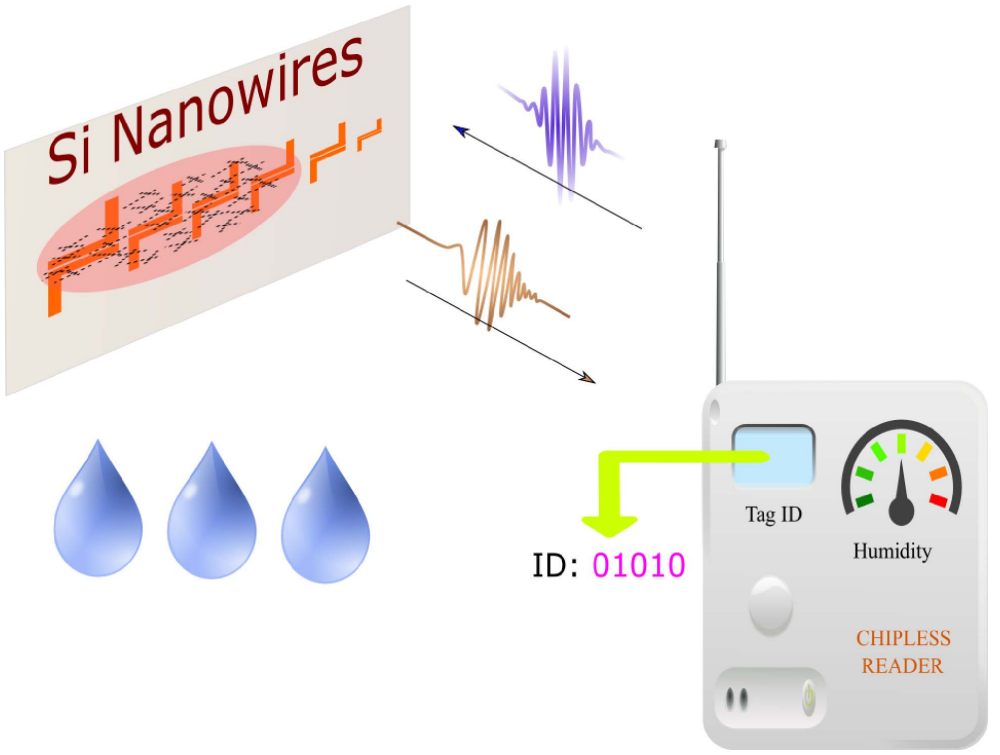

Figure 7. Illustration of the reading of a chipless tag with an identifier and a humidity sensor. Resonators are either used to encode the information or to read the relative humidity in the air. In this example, a humidity-sensitive material (silicon nanowires—SiNw) has been deposited on these resonators. Therefore, the resonance frequency associated with these specific resonators (with SiNw) will change according to the relative humidity level. The measurement of the 6 resonance frequencies allows the recovery of the tag's ID and the humidity value in one go.

Figure 8c, d show measurements made on resonators where drops of silicon nanowire have been deposited [28]. Indeed, a dozen drops of solutions containing silicon nanowires were deposited on a specific resonator of the tag. A climate chamber or a sealed container into which water was placed (to simulate a more realistic environment) made it possible to cause the relative humidity (HR) to vary in time inside the box, between around 70% and 100%. Significant variations have been observed around the resonant frequency of the chipless tag (35 MHz of frequency shift). For example, by comparing the measurement results with the EM simulations, it has been possible to understand the electrical behavior of the silicon nanowires: we can deduce that the presence of humidity will simultaneously modify permittivity and losses. A measurement of the same structure but without the presence of nanowires (see Figure 8d), under the same conditions, does not display any significant variations in RCS, which shows that it is the nanowires that are exacerbating this phenomenon. A last important point is that it has been observed that the variations are reproducible from one day to the next [45]. In fact, the same tag was measured under the same conditions several weeks later, and the results obtained are comparable.

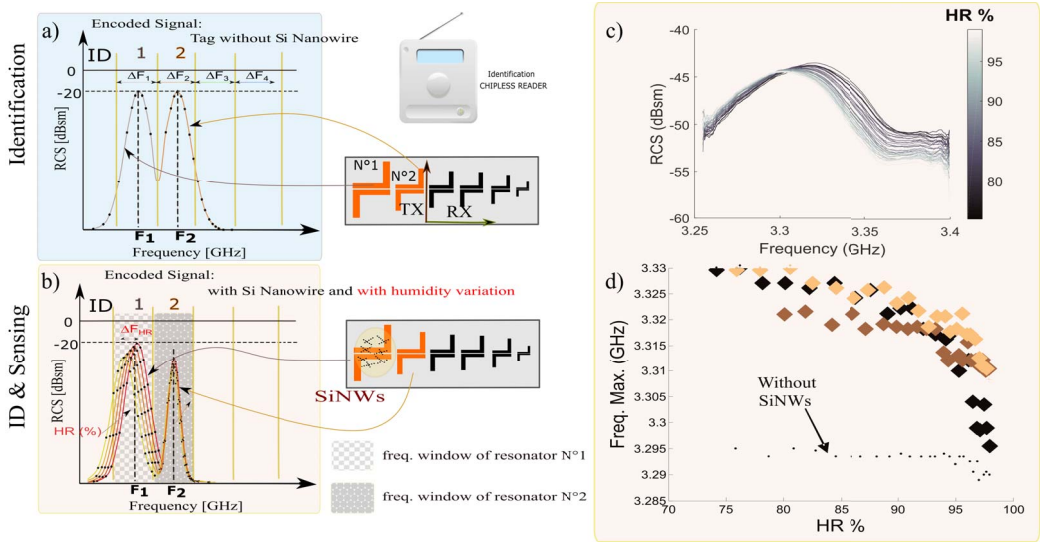

Figure 8. Operating principle of a chipless tag comprising an ID and a sensor function. (a) Tag used for identification—in this case the ID is determined by looking in which ΔFi sub-windows the peaks relating to the resonance frequencies of the tags are present. (b) Sensor function: a material sensitive to the physical quantity to be measured is added to resonators. The information on the physical quantity will be obtained by measuring precisely the value of the resonance frequency and by using either an analytical model or a lookup table to find the required value. (c) Example of the variation of the RCS as a function of humidity (measurements—resonator with SiNw). (d) Variations of the resonance frequency as a function of the relative humidity for 3 identical sensors and a resonator without SiNw.

4.3. *Gesture recognition*

As previously shown, chipless tags are sensitive to their surrounding environment. It means that, if desired, they can be affected by the position of the user's hands or fingers on the top of the label. Moreover, a radar approach is used to read these tags, which means that it is fully adapted for localization purposes. If we combine these two statements, we will see that chipless tags can be used to introduce a new kind of application, i.e. for gesture recognition as illustrated in Figure 9. So the question is: can a simple chipless label be used to control electronic equipment?

Contactless human-computer interactions (HCI) using EM waves have already been investigated in the literature. Project Soli is developed by Google ATAP since 2015 [46]. As compared to Project Soli, our solution would operate in UWB band and would use chipless paper tag to identify the label, and thus the user itself. The WISP (Wireless Identification and Sensing Platform) is another project which can produce contactless HCI [47]. This platform is based on the use of a low power microcontroller coupled with sensors. The whole system can be powered by standard RFID readers and can communicate using backscatter modulation. Unlike WISP, our solution proposes a simple chipless tag to sense the environment, that is to say without any electronic component. Initial studies show that it is possible to developed the concept of HCI based on the use of radar chipless labels [29, 30, 48]. Our system has to detect specific user gesture like the displacement of the label (see Figure 9a) or the position of the finger on a tag's surface (see Figure 9b) [30]. The chipless tag, made on paper is playing the role of a remote control but without any electronic component.

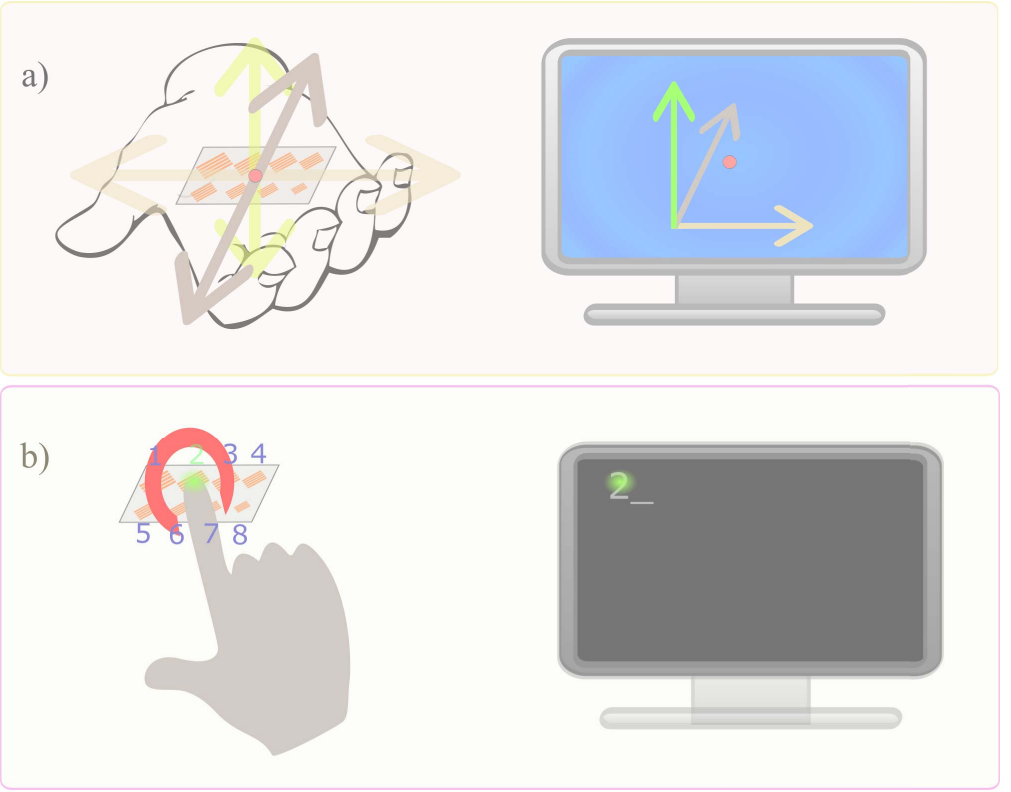

Figure 9. Gesture recognition applications: chipless label acting as a remote control. (a) Joystick mode, (b) keyboard mode.

This is based on the observation that it is possible to extract the displacement of chipless labels with submillimeter precision [35]. So, as it is possible to measure in real time the position of the tag, gesture recognition can be considered. Moreover, the identification function of the chipless tag is still available in the signature and can be used to separate various users.

Figure 10 explains the principle of operation of a label that can be used in keyboard mode. One can imagine a two-phase operation. (1) The user approaches the tag to the reader to read the identifier so that the reader recognises the user in front of it. (2) By pressing the finger on different areas of the tag, one area after the other—like using a keyboard—the user can communicate information to the reader. The principle is based on the fact that the finger has a high effective permittivity, which causes the resonance frequency to vary by several GHz, making it disappear from the frequency band and thus allowing the reader to detect this disappearance. Since the geometrical position of the resonator is perfectly known, it is possible to print a keyboard like numbers on the label in a perfectly visible way (see Figure 9b) [30].

5. Conclusion

The development of the new paradigm of RF communication system based on chipless labels is now highly expected. This means a totally passive tag without any chip, bringing an ID, able to communicate with radio wave and having extremely low costs. With comparable costs to a barcode, this new technology should stand out by providing more functionalities than the optical approach.

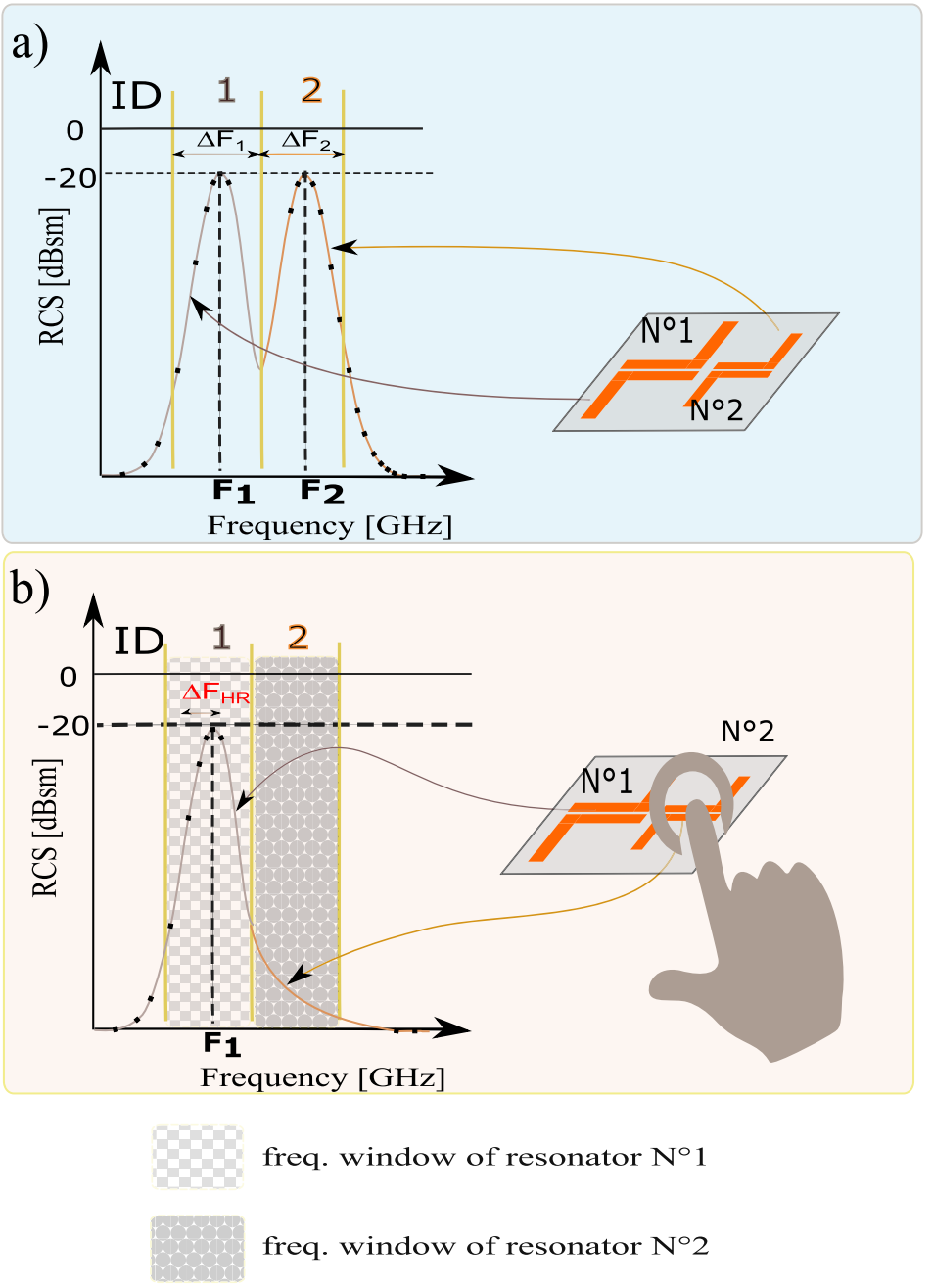

Figure 10. Operating principle of a chipless tag usable in keyboard mode. (a) RCS of the tag presented to the reader for identification. (b) Once the identification has been carried out, the user can interact with the reader by pressing on a specific zone of the tag (where a keyboard can be printed). The action of the finger on the tag will cause the peak related to the resonance frequency of the touched resonator to disappear.

The use of CBRAM technology nowadays provides a non-volatile RF behaviour in such a simple manner. Similarly, it seems to be the only approach that would allow (i) to control the RF switches activation remotely (by radio wave); which is due to the low power needed to change the state, (ii) to manufacture switches entirely through printing techniques. It is obvious that scientific challenges have to be addressed and solved such as: a better understanding of the filament creation, the role that the dielectric plays in it, how to reduce the inherent MIM capacity in order to increase the frequency range of use, how to minimize the equivalent resistance of the conductive state, how to increase the manufacturing reliability.... In all cases, the use of this technology to achieve printable, reconfigurable chipless tags, is original and promising for future applications in the field of identification and sensing of totally passive and printable labels. Chipless RFID technology is also very interesting to achieve sensor functions. This is based on the use of the radar approach coupled with the use of particular targets, that is to say resonant targets that allow to significantly increase the signal to noise ratio around the resonance frequencies as well as to perform time windowing. Numerous conceptual possibilities for such a use are currently being studied. Concerning gesture recognition, the goal is to develop a system that can detect the specific user gesture, like the position of the finger on a tag's surface. The chipless tag, made on paper with an inkjet printer would play the role of a remote control but without any electronic component. Indeed, since the architecture is based on a chipless tag, the system is entirely passive and does not need any battery. With the radar approach used in chipless, lots of accurate and useful data can be deduced form that type of reading. For example, as it is possible to measure in real time the position of the tag (the distance between the tag and the reader but also lots of other relevant data), gesture recognition can be considered. Moreover, the identification function of the chipless tag is still available in the signature and can be used to separate various users. Chipless paper tags could have a huge impact in the development of the concept of "smart packaging" or "smart paper". New progresses in conductive inks give the possibility for printer companies to think about new applications for their printers now able to print on paper with conductor ink.

Conflicts of interest

The author has no conflict of interest to declare.

Acknowledgments

This work was supported in part by the Institut Universitaire de France and by the European Research Council (ERC) under the European Union's Horizon 2020 Research and Innovation Program (grant agreement No 772539 - ScattererID). The authors are also thankful towards Nathalie Franck for his help in proofreading the paper.

References

[1] S. Cavel, C. Millet, "Les étiquettes RFID", 2004, http://cerig.efpg.inpg.fr/memoire/2004/rfid.htm#code_barres.
[2] P. Nikitin, "Leon Theremin (Lev Termen)", *IEEE Antennas Propag. Mag.*, 2012, **54**, no. 5, 252-257.
[3] E. Perret, *Radio Frequency Identification and Sensors: From RFID to Chipless RFID*, Wiley, Hoboken, NJ, USA, 2014, London, UK: ISTE.
[4] S. Preradovic, N. C. Karmakar, "Chipless RFID: Bar code of the future", *IEEE Microw. Mag.*, 2010, **11**, no. 7, 87-97.
[5] S. Tedjini, N. Karmakar, E. Perret, A. Vena, R. Koswatta, R. E. Azim, "Hold the chips: Chipless technology, an alternative technique for RFID", *IEEE Microw. Mag.*, 2013, **14**, no. 5, 56-65.
[6] O. Rance, E. Perret, R. Siragusa, P. Lemaitre-Auger, *RCS Synthesis for Chipless RFID: Theory and Design*, ISTE Press, London, UK, 2017, Oxford, UK: Elsevier.

[7] A. Vena, E. Perret, S. Tedjini, *Chipless RFID Based on RF Encoding Particle — Realization, Coding and Reading System*, ISTE, London, UK, 2016, Oxford, UK: Elsevier.
[8] A. Vena, E. Perret, S. Tedjini, "Design of compact and auto compensated single layer chipless RFID tag", *IEEE Trans. Microw. Theory Tech.*, 2012, **60**, no. 9, 2913-2924.
[9] A. Vena, E. Perret, S. Tedjini, "Chipless RFID tag using hybrid coding technique", *IEEE Trans. Microw. Theory Tech.*, 2011, **59**, no. 12, 3356-3364.
[10] O. Rance, R. Siragusa, P. Lemaître-Auger, E. Perret, "Contactless characterization of coplanar stripline discontinuities by RCS measurement", *IEEE Trans. Antennas Propag.*, 2017, **65**, no. 1, 251-257.
[11] E. Perret, "Permittivity characterization based on Radar Cross measurements", in *International Symposium Electromagnetic Theory (EMTS 2016), URSI, Finland*, Union Radio-Scientifique Internationale (URSI), 2016 (Invated paper).
[12] F. Requena, N. Barbot, D. Kaddour, E. Perret, "Contactless characterization of metals' thermal expansion coefficient by a free-space RF measurement", *IEEE Trans. Antennas Propag.*, 2021, **69**, no. 2, 1230-1234.
[13] O. Rance, R. Siragusa, P. Lemaître-Auger, E. Perret, "RCS magnitude coding for chipless RFID based on depolarizing tag", in *IEEE MTT-S International Microwave Symposium Digest, Phoenix, USA*, IEEE, 2015.
[14] A. Vena, E. Perret, S. Tedjini, "A depolarizing chipless RFID tag for robust detection and its FCC compliant UWB reading system", *IEEE Trans. Microw. Theory Tech.*, 2013, **61**, no. 8, 2982-2994.
[15] A. Vena, E. Perret, S. Tedjini, "A fully printable chipless RFID tag with detuning correction technique", *IEEE Microw. Wirel. Compon. Lett.*, 2012, **22**, no. 4, 209-211.
[16] A. Vena, E. Perret, S. Tedjini, "Design of compact and auto compensated single layer chipless RFID tag", *IEEE Trans. Microw. Theory Tech.*, 2012, **60**, no. 9, 2913-2924.
[17] A. Ramos, E. Perret, O. Rance, S. Tedjini, A. Lazaro, D. Girbau, "Temporal separation detection for chipless depolarizing frequency-coded RFID", *IEEE Trans. Microw. Theory Tech.*, 2016, **64**, no. 7, 2326-2337.
[18] A. Vena, E. Perret, S. Tedjini, "High capacity chipless RFID tag insensitive to the polarization", *IEEE Trans. Antennas Propag.*, 2012, **60**, no. 10, 4509-4515.
[19] N. Barbot, O. Rance, E. Perret, "Chipless RFID reading method insensitive to tag orientation", *IEEE Trans. Antennas Propag.*, 2021, **69**, no. 5, 2896-2902.
[20] N. Barbot, O. Rance, E. Perret, "Angle sensor based on chipless RFID tag", *IEEE Antennas Wirel. Propag. Lett.*, 2020, **19**, no. 2, 233-237.
[21] N. Barbot, O. Rance, E. Perret, "Cross-polarization chipless tag for orientation sensing", in *2020 50th European Microwave Conference (EuMC), Utrecht, Netherlands*, IEEE, 2021, 1119-1122.
[22] E. Perret, S. Tedjini, R. Nair, "Design of antennas for UHF RFID tags", *Proc. IEEE*, 2012, **100**, no. 7, 2330-2340.
[23] A. Vena, E. Perret, S. Tedjini, G. E. P. Tourtollet, A. Delattre, F. Garet, Y. Boutant, "Design of chipless RFID tags printed on paper by flexography", *Antennas Propag., IEEE Trans.*, 2013, **61**, no. 12, 5868-5877.
[24] A. Vena, E. Perret, S. Tedjini, G. E. P. Tourtollet, A. Delattre, F. Garet, Y. Boutant, "Design of chipless RFID tags printed on paper by flexography", *IEEE Trans. Antennas Propag.*, 2013, **61**, no. 12, 5868-5877.
[25] A. Vena, T. Singh, S. Tedjini, E. Perret, "Metallic letter identification based on radar approach", in *General Assembly and Scientific Symposium, 2011 XXXth URSI, Istanbul, Turkey*, IEEE, 2011, 1-4.
[26] J. M. Purushothama, S. Lopez-Soriano, A. Vena, B. Sorli, I. Susanti, E. Perret, "Electronically rewritable chipless RFID tags fabricated through thermal transfer printing on flexible PET substrates", *IEEE Trans. Antennas Propag.*, 2021, **69**, no. 4, 1908-1921.
[27] F. Requena, M. Gilch, N. Barbot, D. Kaddour, R. Siragusa, F. Costa, S. Genovesi, E. Perret, "Thermal modeling of resonant scatterers and reflectometry approach for remote temperature sensing", *IEEE Trans. Microw. Theory Tech.*, 2021, **69**, no. 11, 4720-4734.
[28] A. Vena, E. Perret, D. Kaddour, T. Baron, "Toward a reliable chipless RFID humidity sensor tag based on silicon nanowires", *IEEE Trans. Microw. Theory Tech.*, 2016, **64**, no. 9, 2977-2985.
[29] N. Barbot, E. Perret, "Gesture recognition with the chipless RIFD technology", in *URSI General Assembly and Scientific Symposium (GASS), Montreal, QC, Canada, 19–26 August 2017*, IEEE, 2017.
[30] R. Unnikrishnan, O. Rance, N. Barbot, E. Perret, "Chipless RFID label with identification and touch-sensing capabilities", *Sensors*, 2021, **21**, no. 14, article no. 4862.
[31] The Scatterer ID project, 2022, ERC Agreement 772539. Accessed: Fev. 07, 2022. [Online], https://www.scattererid.eu/.
[32] A. Vena, E. Perret, S. Tedjini, "A depolarizing chipless RFID tag for robust detection and its FCC compliant UWB reading system", *IEEE Trans. Microw. Theory Tech.*, 2013, **61**, no. 8, 2982-2994.
[33] O. Rance, N. Barbot, E. Perret, "Design of planar resonant scatterer with roll-invariant cross polarization", *IEEE Trans. Microw. Theory Tech.*, 2020, **68**, no. 10, 4305-4313.
[34] Z. Ali, E. Perret, N. Barbot, R. Siragusa, "Extraction of aspect-independent parameters using spectrogram method for chipless frequency-coded RFID", *IEEE Sensors J.*, 2021, **21**, no. 5, 6530-6542.
[35] E. Perret, "Displacement sensor based on radar cross-polarization measurements", *IEEE Trans. Microw. Theory Tech.*, 2017, **65**, no. 3, 955-966.

[36] E. Perret, "Micrometric displacement sensor based on chipless RFID", in *IEEE MTT-S International Microwave Symposium (IMS2017), Honolulu, Hawaii, United States*, IEEE, 2017.
[37] F. Requena, N. Barbot, D. Kaddour, E. Perret, "Chipless RFID temperature and humidity sensing", in *2021 IEEE MTT-S International Microwave Symposium (IMS)*, IEEE, 2021, 545-548.
[38] J. Nessel, R. Lee, "Chalcogenide Nanoionic-Based Radio Frequency Switch", April 12, 2013, US Patent 7 923 715 B2.
[39] M. P. Jayakrishnan, A. Vena, B. Sorli, E. Perret, "Nafion based fully passive solid state conductive bridging RF switch", *IEEE Microw. Wirel. Compon. Lett.*, 2017, **27**, no. 12, 1104-1106.
[40] I. Valov, R. Waser, J. R. Jameson, M. N. Kozicki, "Electrochemical metallization memories—fundamentals, applications, prospects", *Nanotechnology*, 2011, **22**, no. 25, article no. 254003.
[41] E. Perret, T. Vidal, A. Vena, P. Gonon, "Realization of a conductive bridging RF switch integrated on to printed circuit board", *Prog. Electromagn. Res.*, 2015, **151**, 9-16.
[42] A. Vena, E. Perret, S. Tedjini, C. Vallée, P. Gonon, C. Mannequin, "A fully passive RF switch based on nanometric conductive bridge", in *IEEE MTT-S International Microwave Symposium (IMS), Montreal, Canada*, IEEE, 2012.
[43] A. Vena, E. Perret, S. Tedjini, C. Vallée, P. Gonon, C. Mannequin, "A fully passive RF switch based on nanometric conductive bridge", in *IEEE MTT-S International Microwave Symposium (IMS), Montreal, Canada*, IEEE, 2012.
[44] J. Nessel, R. Lee, "Chalcogenide nanoionic-based radio frequency switch, USA", 2010, US 7 923 715 B2.
[45] A. Vena, E. Perret, D. Kaddour, T. Baron, "Toward a reliable chipless RFID humidity sensor tag based on silicon nanowires", *IEEE Trans. Microw. Theory Tech.*, 2016, **64**, no. 9, 2977-2985.
[46] J. Lien, N. Gillian, M. E. Karagozler, P. Amihood, C. Schwesig, E. Olson, H. Raja, I. Poupyrev, "T Soli: ubiquitous gesture sensing with millimeter wave radar", *J. ACM Trans. Graph.*, 2016, **35**, no. 4, 1-19.
[47] A. P. Sample, D. J. Yeager, P. S. Powledge, A. V. Mamishev, J. R. Smith, "Design of an RFID-based battery-free programmable sensing platform", *IEEE Trans. Instrum. Meas.*, 2008, **57**, no. 11, 2608-2615.
[48] N. Barbot, E. Perret, "A chipless RFID method of 2D localization based on phase acquisition", *J. Sensors*, 2018, **2018**, article no. 7484265.

Comptes Rendus

Physique

Objet de la revue

Les *Comptes Rendus Physique* sont une revue électronique évaluée par les pairs de niveau international, qui couvre l'ensemble des domaines de la physique et de l'astrophysique. Ils publient principalement des numéros thématiques, mais également des articles originaux de recherche, des annonces préliminaires, des articles de revue, des mises en perspective historiques, des textes à visée pédagogique ou encore des actes de colloque, sans limite de longueur, en anglais ou en français. Ils proposent également des numéros spéciaux consacrés à certains aspects récents et/ou significatifs de la discipline, dont les auteurs sont choisis parmi les chercheurs les plus actifs sur le sujet et dont la coordination est assurée par des rédacteurs en chef invités.

Les *Comptes Rendus Physique* sont diffusés selon une politique vertueuse de libre accès diamant, gratuit pour les auteurs (pas de frais de publications) comme pour les lecteurs (libre accès immédiat et pérenne).

À propos de la revue

Toutes les informations concernant la revue, y compris le texte des articles publiés qui est en accès libre intégral, figurent sur le site https://comptes-rendus.academie-sciences.fr/physique/.

Informations à l'attention des auteurs

Pour toute question relative à la soumission des articles, les auteurs peuvent consulter le site https://comptes-rendus.academie-sciences.fr/physique/.

Contact

Académie des sciences
23, quai de Conti, 75006 Paris, France
Tél. : (+33) (0)1 44 41 43 72
CR-Physique@academie-sciences.fr

Comptes Rendus
de l'Académie des sciences

Physique

Volume 22, nº S5, 2021

Special issue / *Numéro thématique*
Prizes of the French Academy of Sciences 2020 / *Prix 2020 de l'Académie des sciences*

1878-1535 (electronic)

Académie des sciences — Paris

COMPTES RENDUS
DE L'ACADÉMIE DES SCIENCES

Physique

Volume 22, nº S5, 2021